

INVESTIGATION OF TRIBOCHEMICAL REACTIONS USING THE MODEL SYSTEM OF  
METHYLTHIOLATE ON COPPER FOIL IN ULTRAHIGH VACUUM AND AB-INITIO  
CALCULATIONS

by

Heather Adams

A Dissertation Submitted in

Partial Fulfillment of the

Requirements for the Degree of

Doctor of Philosophy

in Chemistry

at

The University of Wisconsin-Milwaukee

December 2017

## ABSTRACT

### INVESTIGATION OF TRIBOCHEMICAL REACTIONS USING THE MODEL SYSTEM OF METHYLTHIOLATE ON COPPER FOIL IN ULTRAHIGH VACUUM AND AB-INITIO CALCULATIONS

by

Heather Adams

The University of Wisconsin-Milwaukee, 2017  
Under the Supervision of Professor Tysoe

Advancement in the understanding of tribochemical systems suffers from several obstacles that hinder the progress in advancing an understanding of the fundamental processes involved in the evolution of friction and wear. Characterizing ephemeral chemical states within a buried interface is an experimental challenge and work in this dissertation uses a model system, methyl thiolate on copper foil, that undergoes tribo-activated decomposition to investigate the rate of change of the chemical components in the interface. The elementary steps in the tribochemical reaction were identified and consist of a shear-induced decomposition of methyl thiolate species to produce gas-phase hydrocarbons and form surface sulfur, which is mechanochemically transported into the sub-surface copper region resulting in changes in the friction coefficient. A method has been developed to analyze the changes in sliding-induced gas-phase product formation and friction coefficient as a function of the number of passes over the surface with a tribopin. Finally, the Vienna Ab-Initio Simulation Package (VASP) is used to calculate the methyl thiolate decomposition energies on Cu(100) as a function of load and the results are compared to the extended-Bell model.

To  
My mom  
My sisters and brothers  
All the women out there fighting for their place in the world  
And most especially my daughter, Moira

# TABLE OF CONTENTS

ABSTRACT.....	ii
DEDICATION.....	iii
TABLE OF CONTENTS.....	iv
LIST OF FIGURES .....	x
ACKNOWLEDGMENTS .....	xxi
Chapter 1.....	1
Chapter 2.....	10
2.1 Introduction.....	10
2.2 Vacuum equipment.....	10
Pressure measurement.....	11
Diaphragm gauges .....	11
Ionization gauges .....	13
Attaining low pressure .....	15
Mechanical pumps .....	16
Turbo-molecular pumps.....	17
Diffusion Pumps .....	18
Ion Pump.....	20

2.3 UHV Chambers.....	22
Chamber body.....	22
Flanges .....	23
Working in UHV.....	23
Metal Sample .....	24
Introducing Gaseous Reactants.....	24
Leak valves .....	26
Linear motion.....	26
Rotary motion .....	27
Electricity.....	27
2.4 Instruments.....	28
Auger Electron Spectroscopy .....	28
Mass Spectrometer.....	30
Ultrahigh Vacuum Tribometer.....	31
2.5 Experimental Protocols.....	32
Liquid-Sample Purification.....	32
Sample Cleaning .....	33
Aligning the Sample in the Tribometer .....	34
2.6 Tribometer Chamber.....	35
Monolayer dosing experiments.....	36

Continuous-dosing experiments.....	37
2.7 Conclusion .....	37
Chapter 3.....	39
3.1 Introduction.....	39
3.2 Single electron model .....	40
3.3 Density Functional Theory .....	43
3.4 Potentials.....	44
3.5 Projector-Augmented plane-wave approximations.....	45
3.6 Ionic Minimization.....	47
3.7 Minimum Energy Pathway for a reaction.....	49
3.8 Conclusion .....	52
3.9 References.....	53
Chapter 4.....	55
4.1 Introduction.....	55
4.2 Experimental.....	57
4.3 Theoretical Methods .....	59
4.4 Results.....	60
4.5 Discussion.....	69
Chapter 5.....	89
5.1 Introduction.....	89

5.2 Experimental .....	92
5.3 Results .....	93
Analysis of Methyl Thiolate Kinetics .....	106
Analysis of Ethyl Thiolate Kinetics .....	107
5.5 Conclusions .....	109
Acknowledgements .....	<b>Error! Bookmark not defined.</b>
Chapter 6 .....	115
6.1 Introduction .....	115
6.2 Experimental Methods .....	117
Vacuum System .....	117
XPS Measurements .....	118
Material .....	118
6.3 Results .....	119
Measurement of Total Subsurface Sulfur .....	121
Angle-Resolved Electron Spectroscopy Analyses of Subsurface Sulfur .....	122
6.4 Discussion .....	124
Kinetic Analysis of Mechanochemical Reaction using first-order processes .....	124
Subsurface Sulfur Concentration and Distribution .....	128
Nature of the Subsurface Sulfur .....	130
6.5 Conclusion .....	131

6.6 References.....	132
Chapter 7.....	139
8.1 Introduction.....	139
8.2 Theoretical Methods .....	140
8.3 Results and discussion .....	143
Change in Activation Energy with Applied Load.....	143
Response to shear force by translation of the molecule.....	148
Tilting methylate – response to load and shear.....	152
7.4 Conclusion .....	153
Chapter 8.....	158
8.1 Introduction.....	158
8.2 Experimental.....	159
8.3 Results.....	161
8.5 Discussion.....	166
8.6 Proof of concept experiments .....	169
8.7 Conclusion .....	172
8.8 References.....	174
Chapter 9.....	177
Education .....	179
Doctorate   09/2009-2017.....	179

Bachelors of Science.....	179
Publications.....	179
Awards .....	180
Presentations .....	180
Teaching Experience.....	180

# LIST OF FIGURES

Figure 2-1 Schematic of a diaphragm gauge of a system at low (left) and high (right) pressure.	12
Figure 2-2 Ion gauge schematic showing the filament, grid and collector .....	13
Figure 2-3 Graph with curves representing typical pumping speeds versus pressure for the pumps discussed in this work. Black - rotary pump, red - turbo pump, green - diffusion pump and blue - ion pump .....	15
Figure 2-4 A) Mechanical pump schematic and B) Welch Vacuum graph of pumping speed versus Pressure for a the Welch Duo seal pump users from the manual reprinted with permission from Welch Vacuum Corp.....	16
Figure 2-5 Turbo pump diagram from Varian V-70 turbo pump manual. (B) Pumping speed versus inlet pressure for Varian turbo pump from Varian v-70 turbo pump manual. Reprinted with permission from Varian .....	17
Figure 2-6 Schematic of a diffusion pump. Cooling lines are not shown. Diffusion pumping speed graph versus pressure is shown from an Agilent Diffusion pump description. Reprinted with permission.....	19
Figure 2-7 (A) Ion pump diagram. (B) Pumping speed versus pressure for diode, noble diode and triode ion pumps .....	21
Figure 2-8 Top (left) and side (right) view of a conflat flange.....	23
Figure 2-9 Top(left) and side (right) view of the sample holder with a copper foil sample mounted on tantalum rods with heating wires and thermocouple attached. ....	24
Figure 2-10 Diagram of the gas-handling line.....	25
Figure 2-11 Drawing of A) outer and B) inner workings of a typical leak valve.....	26
Figure 2-12 Linear motion feed through in the retracted (A) and extended (B) positions .....	26

Figure 2-13 Rotary motion feedthrough with universal joint ..... 27

Figure 2-14 Copper feedthrough with ceramic insulation on a conflat flange ..... 27

Figure 2-15 Diagram of the ejection of a KLL Auger electron. The primary electron is shown in black, shell electrons go from yellow to red, secondary electrons are light blue and Auger electron is dark blue ..... 29

Figure 2-16 Auger spectroscopy system composed of cylindrical mirror analyzer, electron gun, and detector ..... 30

Figure 2-17 Quadrupole mass spectrometer diagram ..... 31

Figure 2-18 Tribometer Arm with strain sensors ..... 32

Figure 2-19 Diagram of an ion gun ..... 33

Figure 2-20A) representation of the sample alignment with respect to the direction of travel of the tip. B) graphs of load versus time for a reciprocal slide of the tribometer pin as the sample is corrected from far out of alignment, black line, to better aligned, red line, to green line, where the sample is parallel to the path of the pin ..... 34

Figure 2-21 Cutaway, side-view of the tribometer chamber ..... 35

Figure 2-22 Cut-away top view of tribometer chamber ..... 36

Figure 3-1 Searching for the global minimum of energy for an ion (in gray) on a potential energy surface. A) and B) give false minimums due to the proximity of a local minimum and a small slope, respectively. C) shows an ion that could move along lines of force to the global minimum ..... 47

Figure 3-2 The ion movement determined by conjugate gradient method. A) shows the path of the ion at an angle to that of steepest descent. B) shows several steps along the path near the minimum. .... 48

Figure 3-3 Movement determined by the quasi-Newtonian force method. A) shows the ion moving along the path of steepest descent of a potential energy surface. B) shows the path of an ion accelerated using a time-step that moves the ion too far through the minimum. .... 49

Figure 3-4 A) NEB method for finding the MEP. The ionic positions are constrained by a spring force between them, represented by gray arrows, along the direction of the reaction path that keeps the steps equally spaced. The path goes through the saddle point, but it is not necessarily likely to find an image located directly at the transition state. B) cut-away image of cNEB method. The same potential energy surface is used as in figure 4, but the forces are inverted along the potential energy path..... 51

Figure 4.1 (A) Plot of the 16 amu (methane) signal measured during reciprocating sliding on a thiolate-saturated copper foil as a function of the number of scans at a sliding speed of  $4 \times 10^{-3}$  m/s with a normal load of 0.44 N. The methane signals measured while the pin is moving towards the sample are labeled T and those measured with the pin moving away from the sample are labeled A. (B) Expanded profile of a methane desorption pulse measured at a sliding speed of  $2 \times 10^{-3}$  m/s with a normal load of 0.44 N. .... 62

Figure 4.2 The profile of energy versus the lateral displacement of the methyl group in methyl thiolate, for the decomposition of methyl thiolate species on a Cu(100) surface obtained using density functional theory calculations. The calculated activation energy ( $\sim 1.1$  eV,  $\sim 106$  kJ/mol) is in good agreement with the experimental value measured by temperature-programmed desorption.<sup>21</sup> Shown also in the figure is the evolution in the structure of the thiolate species as it forms adsorbed methyl species. .... 64

Figure 4.3 (A) The 16 amu (methane) signal measured by sliding a tungsten carbide pin containing a copper transfer film on a pre-rubbed (50 scans) clean copper foil as a function of the number of

scans at a sliding speed of  $1 \times 10^{-3}$  m/s with a normal load of 0.44 N showing the decay in methane desorption yield as a function of the number of scans. Shown as an inset is the desorption yield measured from the area under each methane pulse as a function of the number of scans. After collecting data for the first DMDS dose while sliding at  $4 \times 10^{-3}$  m/s, until no more methane was detected (■), the sample was re-saturated with DMDS and the 16 amu signal again monitored (●). This experiment was repeated for the third (▲), fourth (▼) and fifth (◆) DMDS doses, where the evolution of methane yield as a function of the number of scans is identical within experimental error. (B) Plot of the desorption yield measured from the integrated area under each desorption pulse for the  $n^{\text{th}}$  pass  $Y_n$  for the desorption of methane during sliding, taken from the data in Figure 2A, plotted versus  $(n-1)$ . ..... 66

Figure 4.4 Plot of the calculated energy barrier as a function of the shear force obtained from the calculated energy profile for the decomposition of thiolate species (Fig. 2) by superimposing a potential due to the external force,  $V(x)=-Fx$ . This is compared with the prediction of the conventional Bell model, drawn as a red line. Indicated also as thick lines is the discrete force (of  $\sim 0.5$  eV/Å) that would be required to lower the activation barrier to the experimentally measured values of between 64 and 58 kJ/mol). An inset shows a plot of the height of the activation barrier as a function of  $[(F^*-F)]^{.32}$ , where  $F^*$  is the value of the force at which the energy barrier decreases to zero. .... 71

Figure 4.5 Contact force distributions along the loading (left figure) and sliding (right figure) directions taken at a sliding speed of 40 m/s with a contact pressure of 450 MPa..... 74

Figure 4.6 The calculated force distribution from MD simulations of  $\sim 0.45$  monolayers of methyl thiolate species on Cu(100) (where a monolayer is defined as the number of thiolate molecules per copper atom on the (100) surface) at a sliding speed of 4 mm/s with a contact pressure of 450 MPa;

snapshots of the simulations are shown in the insets and a movie is shown in the Supporting Information section. The calculated average force  $F_0$  is  $\sim 0.08$  nN (dashed line in figure). However, the distribution of forces is Gaussian with a significant proportion of molecules experiencing much larger forces than the average value. The calculations show that  $D$ , defined as  $\sigma/F_0$ , where  $\sigma$  is the standard deviation of the force distribution (dotted line in figure) is  $\sim 6.9$  ..... 75

Figure 4.7 Plot of the influence on the effective activation energy  $E_a(F)$  for a Gaussian force distribution with an average force of  $F_0 \sim 0.018$  nN/molecule with a width at half maximum of  $\sigma$ , where the energy is plotted versus  $D$ , defined as  $D = \sigma/F_0$ . In this case, the value of  $F_0$  was estimated by assuming that the surface deforms elastically. The horizontal line shows the measured value of the shear-induced methyl thiolate decomposition activation energy again assuming elastic deformation of the contact. .... 77

Table 4.1 The average contact pressure and track length calculated for various contact models (see Supporting Information, Section 3). Shown also is the average force per molecule, and the calculated shear-induced methyl thiolate decomposition rate constant,  $k(F)$  and well as the corresponding reaction activation energy calculated assuming a standard pre-exponential factor of  $1 \times 10^{13} \text{ s}^{-1}$  ..... 78

Figure 4.8 Plot of the influence on the effective activation energy  $E_a(F)$  for a Gaussian force distribution with an average force of  $F_0 \sim 0.07$  nN/molecule with a width at half maximum of  $\sigma$ , where the energy is plotted versus  $D$ , defined as  $D = \sigma/F_0$ . In this case, the value of  $F_0$  was estimated by assuming that the surface deforms plastically. The horizontal line shows the measured value of the shear-induced methyl thiolate decomposition activation energy again assuming plastic deformation of the contact. .... 79

Table 4.2 Values of D obtained from the molecular dynamics simulation at different normal pressures at a sliding speed of 40 m/s.....	80
Figure 4.9 Atomic force microscope image of a 70 $\mu\text{m}$ $\times$ 70 $\mu\text{m}$ region of the wear track region after completion of the run-in period.....	81
Figure 5.1 Plot of the 26 amu signal as a function of the number of scans at a load of 0.44 N at a sliding speed of 4 mm/s, after exposing the copper foil to 0.7 L of DEDES. Note that the unequal intervals between scans arises from the different times between scans.....	95
Figure 5.2 Plot of relative coverage of the sulfur in the wear track measured by small-spot-size Auger spectroscopy as a function of the number of scans for a methyl thiolate overlayer on the surface, where the sulfur peak-to-peak intensity is normalized to that of the copper substrate. The normal load was 0.44 N, the sliding speed was 4 mm/s and the surface was pre-covered with thiolate species after a wear track had been created by rubbing the clean copper surface 50 times. The line through the data is a fit to the kinetic model .....	97
Figure 5.3 Plot of the friction coefficient as a function of the number of scans while rubbing a methyl thiolate covered copper surface at a normal load of 0.44 N and a sliding speed of 4 mm/s. The line shows a fit to the data (see Discussion section).....	98
Figure 5.4 Plot of integrated areas of the first desorption pulse collected at 26 amu as a function of DEDES exposure in Langmuir (1 Langmuir (L) = $1 \times 10^{-6}$ Torr s) from a dosing tube directed at the sample (●). A line is drawn through the data as a guide to the eye. ....	99
Figure 5.5 Plot of the variation in integrated intensities of the 15 (■), 26 (●), 29 (▲) and 30 (▼) amu signals as a function of the number of scans, after saturating a copper surface, that had previously been rubbed 50 times, with an exposure of 0.8 L of DEDES; a sliding speed of 4 mm/s and a normal load of 0.44 N, were used. Shown as an inset is a plot of the integrated area per pulse	

for ethane (■) and ethylene (●) formation. The ethane signal is calculated by subtracting the contribution due to ethane fragmentation using the fragmentation pattern for ethane measured using the same mass spectrometer as used to collect the shear-induced desorption data..... 101

Figure 5.6 Plot of the friction coefficient as a function of the number of scans while rubbing an ethyl thiolate covered copper surface at a normal load of 0.44 N at a sliding speed of 4 mm/s. The line shows a fit to the data (see Discussion section)..... 102

Figure 5.7 Plot of the calculated coverages of adsorbed methyl thiolate species (■), adsorbed sulfur (●) and the clean copper (▲) surface as a function of the number of scans over a methyl-thiolate covered surface with a normal load of 0.44 N and a sliding speed of 4 mm/s. .... 107

Figure 5.8 Plot of the calculated coverages of adsorbed ethyl thiolate species (■), adsorbed sulfur (●) and the clean copper (▲) surface as a function of the number of scans over an ethyl-thiolate covered surface with a normal load of 0.44 N and a sliding speed of 4 mm/s. .... 109

Figure 6-1 Plot of friction coefficient as a function of the number of passes for the sliding of a copper-covered tungsten carbide ball sliding against copper after the completion of a run-in period (for ~70 scans) and then exposing the surface to a background pressure of  $5 \times 10^{-8}$  Torr of dimethyl disulfide using a normal load of 0.44 N with a sliding speed of 4 mm/s..... 119

Figure 6-2 A series of small-spot-size S 2p angle-resolved XPS spectra inside the wear track after rubbing a clean copper sample after the completion of a run-in period in the presence of a background pressure of  $5 \times 10^{-8}$  Torr of dimethyl disulfide for 160 scans at a load of 0.44 N and a sliding speed of 4 mm/s. The spectra were collected at various take-of angles, indicated adjacent to the corresponding spectrum. .... 121

Figure 6-3 A series of small-spot-size S 2p angle-resolved XPS spectra inside the wear track after rubbing a clean copper sample after the completion of a run-in period in the presence of a

background pressure of  $5 \times 10^{-8}$  Torr of dimethyl disulfide for 160 scans at a load of 0.44 N and a sliding speed of 4 mm/s. The spectra were collected at various take-of angles, indicated adjacent to the corresponding spectrum. .... 121

Figure 6-4 Plot of the integrated area of the S 2p XPS feature, taken from the data shown in Figure 3 as a function of emission angle measured with respect to the surface for a sample that had been rubbed 40 ( $\blacktriangledown$ ), 80 ( $\blacklozenge$ ) and 160 ( $\blacktriangle$ ) times in  $5 \times 10^{-8}$  Torr of DMDS with a load on 0.44 N at 4 mm/s. The lines represent calculated variations in S 2p intensity as a function of detection angle after rubbing as discussed in the text. .... 122

Figure 6-5 Cu KLL Auger spectra obtained within the rubbed region for a sample that had been rubbed for 160 scans in  $5 \times 10^{-8}$  Torr of DMDS and then ion bombarded for 42 s to remove the contaminant layer, collected at detection angles of (a)  $20^\circ$  and (b)  $70^\circ$  with respect to the surface. Shown also are fitted Auger profiles. .... 123

Figure 6-6 Plots of the calculated coverages of adsorbed methyl thiolate, sulfur, the clean surface and subsurface sulfur as a function of the number of passes using parameters that gave the best fit to the friction data (Figure 1). .... 127

Figure 6-7 Plot of the subsurface sulfur concentration as a function of the total number of passes, 40 ( $\blacksquare$ ), 80 ( $\bullet$ ) and 160 ( $\blacktriangle$ ), where the concentration is plotted in units of monolayers of sulfur (ML), and the depth,  $z$  is ratioed to the electron mean free path  $\lambda$  for S 2p electrons with a kinetic energy of  $\sim 1100$  eV when using an Al  $K\alpha$  source ..... **Error! Bookmark not defined.**

Figure 7-1 Methyl thiolate on Cu (100) with a top slab of Cu (100) at 8 Å, lowered in 0.2 Angstrom steps..... 141

Figure 7-2 A low (~0.125 ML) coverage methyl thiolate Cu (100) surface. During calculations methyl group is tilted steps of 10 degrees in the direction of and diagonal to the lattice. Directions of tilt are indicated by arrows. .... 142

Figure 7-3 Energy to lower the top copper slab toward the methyl thiolate species on the surface. Insets are beginning and end state of the compression. .... 144

.....**Error! Bookmark not defined.**

Figure 7-4 Change in activation energy as the top Cu (100) slab moves toward the bottom Cu (100) slab from the non-interacting distance, where the slab separation is indicated by the color of the line. Arrows highlight the change in energy of reactant and transition state.**Error! Bookmark not defined.**

.....**Error! Bookmark not defined.**

Figure 7-5 Energy (eV) versus distance upper slab moved (Å) from the minimum energy position. Red line is a quadratic fit to the curves, the elastic modulus is 0.51 eV/ Å<sup>2</sup>**Error! Bookmark not defined.**

.....**defined.**

Figure 7-6 Distance between top and bottom slab and change in bond length between methyl group and copper atom, and distance that copper atom moved upward from the lattice position. Transition state of the 8 and 5.6 Angstrom cNEBs are on the left as a guide. .... 147

..... 148

Figure 7-7 Activation energy in eV versus force, F, in eV/ Å acting on the top slab. The red line is the equation 3 fit and shows good agreement to the data..... 148

Figure 7-8 A-F moving the methyl group 0.5 0.15, 0.20, 0.25, 0.4, and 0.50 angstroms along the lattice direction. A-C show the copper atoms moving with the sulfur atom and then relaxing back to lattice positions in D. D-F show the methyl thiolate moving over the bridge site. .... 149

Figure 7-9 Charge-density difference calculation between the methyl thiolate and copper calculated separately and together. Blue regions indicate a decrease in charge density, red indicates a decrease. The carbon-sulfur bond shows a decrease in charge-density, indicating  $\pi^*$  back bonding, as discussed in the text..... 150

Figure 7-10 A – C Energy, force, and spring constant for moving the methyl group along the lattice. D-F Energy, force, and spring constant for moving the methyl group diagonal to the lattice. Steps in which one or more copper-sulfur bonds break are marked with a blue line. The inflection points of the energy with distance show bond breaking events..... 151

Figure 7-12 Force to tilt the copper toward bridge (black) or atop (red). The force is low until around 60 degrees, when it increases dramatically due to repulsive force between the methyl group and copper. .... 152

Figure 7-11 Methyl thiolate tilting by 10, 60, and 90 degrees in the lattice direction and D-F, diagonal to it. Copper atoms in the direction of the tilt are repulsed by the methyl group at higher tilts, moving from their lattice positions ..... 152

Figure 7-13 Energy to translate a tilted methyl thiolate over the surface in A) the lattice direction and B) diagonal to it. As the tilt increases the energy of translation increases due to repulsion between the copper and methyl group. .... 153

Figure 8-1 A) Friction coefficients of the first scan of a WC pin across a methyl thiolate covered copper surfaces. Average of the friction coefficient is  $0.34 \pm 0.02$ . B) Friction coefficient of the 15<sup>th</sup> scan shows a wider range, with the 0.88N load value being significantly different from lower loads. .... 161

Figure 8-2 The rate constant for sliding-induced decomposition of methyl thiolate is constant for all loads,  $0.55 \pm 0.09$ ..... 162

Figure 8-3 Total of areas for masses, 15,16 ,26 and 30 AMU for first peak of decomposition of methyl thiolate on copper foil rubbed with WC pin. Rate of increase in gas-phase product with load  $3.26 \pm 0.53$  increase in signal/N ..... 163

Figure 8-4 (A) Friction coefficient of the first pass over a methyl thiolate covered surface has a constant value of  $0.2 \pm 0.02$  with speed. (B) change in friction with rubbing for all normal loads tested. .... 164

Figure 8-5 Rate constant for methyl thiolate decomposition as a function of rubbing speed,  $0.59 \pm 0.05$ . Inset shows the peak area vs scan number for all scans. .... 165

Figure 8-6 Peak area of the 16 amu peak of first scan when sliding on a methyl thiolate covered copper foil for each velocity compared to a 4 mm/s scan done immediately after. .... 166

Figure 8-7 Continuous dosing of dimethyl disulfide while rubbing. Methane production is only present during rubbing. (B) Width of the peak indicates that production of methane from the surface is dependent on contact with the pin. .... 170

Figure 8-8 Rate constant for the release of the methane per pass from a methyl thiolate covered copper surface vs the number of cycles of annealing and bombardment performed at 1000K.. 171

# ACKNOWLEDGMENTS

First, I want to thank my mother, for raising me right, believing in me, providing an example of an ambitious woman, and helping me a tremendous amount as I pursued this degree. She taught me to love curiosity and learning, and her faith in me borders on fanatical. I literally could not have done it without her. Next, I want to thank my daughter. She is patient, and sweet, and knowing that she is watching me gave me courage and strength.

I want to thank Robert Adams, and Anna, John and Stephanie Williams for their support. I appreciate all of them for their support and encouragement. I needed it very much and they came through for me time after time. Also, thank you to my grandmothers, Renny and Rose, and grandpa Cliff.

I would also like to thank my advisor, Dr. Tysoe. More than anyone I've met in graduate school, or outside of it, he takes his responsibilities seriously. He is dedicated to the advancement of science and his passion for guiding the next generation of scientists is inspiring.

My committee members went above and beyond in their help in revising this dissertation and I really appreciate it. Dr. Kotvis has been an amazingly positive and helpful guide to tribology and I am so happy that he has been a part of my committee. Drs. Bennett and Weinert have provided an enormous amount of feedback that has improved both my computational skills and my writing tremendously. Finally, Dr. Woehl was very helpful and his insights into this work have proven very helpful.

I want to thank Dr. Mausumi Mahapatra, for being an anchor and an inspiration. I'm unbelievably proud to be your friend. I want to thank Dr. Ted Theuning for being a legit friend

(the real kind) and Amanda Leichtfuss for quickly becoming one of my favorite people to work with because of her quick understanding and passion for science. I want to say that I appreciate, deeply, Dustin Olson for his passion for science and challenging every statement I make, Dr. John Kestell for showing me the UHV ropes and having an enormous amount of faith in me, Rasha Abuflaha for her tenacity and friendship, Resham Rana for his determination and grit, Sree Roy for his good temper and patience, and Alejandro Boscoboinik for his overwhelming compassion and empathy.

Lastly, I want to thank Dr. Mike Garvey for being a kind and caring mentor who has a passion for making things perfect.

# Chapter 1

## Introduction

Chemical reaction rates can be accelerated by supplying energy thermally, photochemically, by an external electrical potential, or mechanically, the mechanisms by which the latter operates being the least well-understood.<sup>1</sup> Despite this lack of understanding, over the past decades, a large number of mechanochemical syntheses have been discovered.<sup>2-5</sup> Most fundamental insights into how mechanical energy can accelerate a chemical reaction comes from single-molecule force spectroscopy experiments<sup>6-8</sup> that take advantage of the sensitivity of the atomic force microscope and this approach also enables the direction of the force to be controlled with respect to the surface-mediated molecular orientation. The results of such single-molecule pulling experiments have been analyzed theoretically using density functional theory (DFT), where, for example, it has been found that pulling alkyl thiolates from gold<sup>9</sup> or copper<sup>10</sup> causes gold or copper atoms to be plucked out of the surface along with the alkyl thiolate group.

While such experiments and theoretical analyses provide an understanding of the effect of tensional forces, the majority of technologically important mechanochemical reactions are induced by interfacial shear, for example by ball milling or in a sliding contact, where a lubricant additive reacts with a surface to form a film that reduces friction and/or wear. Perhaps the most economically and technologically important mechanochemistry involves the sliding-induced or

“tribochemical” reactions of additives in lubricating oils to form a film that reduces friction and/or wear; it has been suggested that about a third of the fuel in automobile engines is wasted in overcoming friction.<sup>11</sup> Mechanochemical removal of adsorbed layers by shear has been observed in the atomic force microscope<sup>12-14</sup> but the resulting small scan area precludes meaningful surface analyses of the rubbed region from being carried out. DFT analyses have also been used to examine the effect of lateral force on adsorbed layers. For example, it has been shown that shear forces on alkyl thiolates on gold cause lateral motion both of thiolate-gold entities and the surface gold layer<sup>15</sup> in accord with the restructuring of gold surfaces covered by sulfur-containing molecules during scanning.

Analyzing the chemical processes occurring at such sliding solid-solid interfaces, and measuring their reaction rates, is the most challenging of surface chemistry problems since *in situ* spectroscopies, certainly surface-sensitive techniques based on electrons, are impossible. Buried interfaces can be interrogated only using optical spectroscopies when one of the counter-faces is transparent<sup>16</sup> severely limiting the kinds of reactions capable of study.

Because of the lack of access of spectroscopic probes (for example, photons or electrons) to a non-transparent solid-solid interface, there are, as far as we are aware, only three in-situ techniques available for studying chemical reactions and their rates at such interfaces. The first is to measure the change in friction force as a surface reaction proceeds. By arguing that the different intermediates and products have different characteristic frictional properties, the time dependence of the friction force (or friction coefficient) reflects the kinetics of the surface reaction. Thus, if there are several reactants, intermediates and products on the surface, and if the  $i^{\text{th}}$  component has a relative, pass-dependent coverage  $\Theta_i(p)$ , with an associated friction coefficient  $\mu_i$ , then the time evolution of the friction coefficient  $\mu(t)$  can be written as:

$$\mu(t) = \sum_i \mu_i \theta_i(p) \quad (1).$$

This approach is particularly useful in the case of a simple, first-order reaction,  $A_{(\text{ads})} \rightarrow B_{(\text{ads})}$  since,  $\mu_A$  and  $\mu_B$  can be measured before and after reaction to obtain the pass-dependent coverages and has recently been used to follow shear-induced reactions in an atomic force microscope (AFM).<sup>17</sup>

The second approach is to measure the electrical contact resistance while sliding.<sup>18</sup> This technique tends to be more useful for thicker films, but is often difficult to interpret unless the film structure and its conductivity are known. The final approach, developed as part of this dissertation, is to measure the gas-phase products evolved during rubbing using a mass spectrometer. Since the amount of product formed from such a small contact is relatively low, these experiments are carried out under high<sup>19,20</sup> or ultrahigh vacuum. This approach allows both the reaction kinetics to be measured and the nature of the gas-phase products to be monitored.

In this dissertation, Chapter 2 discusses the experimental techniques used in Chapters 4-6 and 8, and Chapter 3 provides a brief summation of density functional theory methods used to analyze the data.

In Chapter 4, these experimental challenges are addressed by using a model mechanochemical system consisting of a ball sliding on a methyl thiolate- ( $\text{CH}_3\text{-S-}$ ) covered copper surface in ultrahigh vacuum (UHV) and by measuring mechanochemical reaction kinetics from the gas-phase products formed during sliding. While DMDS is not a commercial lubricant, it does have the essential ingredients of these additives since DMDS contains S-S linkages that are commonly found in commercial, sulfur-containing lubricants. Crucially, calculations of frictional heating for this experiment reveal a temperature rise much less than 1 K; the interfacial temperature is well defined and has a Boltzmann energy distribution. The experiments are

supplemented by DFT calculations of the reaction energy profiles and molecular dynamics (MD) simulations of the sliding interface to analyze the force distribution on the methyl thiolates during sliding.

Chapter 5 explores the relationship between the force, both normal and shear, on the decomposition of ethyl and methyl thiolate species on a copper foil in ultrahigh vacuum. Ethyl and methyl thiolates decompose under normal and shear forces to form gas-phase alkanes and alkenes, and deposit surface sulfur. The sulfur is then transferred to the bulk, creating a clean copper surface. A model for predicting the composition of the sliding interface is developed using the friction coefficient of each surface species (methyl or ethyl thiolate, sulfur and copper) and their relative coverage as an in-situ analysis of surface coverage. The simplicity of the model system enables the elementary steps in the reaction pathway, in particular those that are mechanochemically induced, to be identified. The first of these is the mechanochemically induced decomposition of methyl thiolate ( $\text{CH}_3\text{-S}_{(\text{ads})}$ ) species, that form rapidly from DMDS on copper, to evolve gas-phase hydrocarbons (methane, ethylene and ethane) and deposit sulfur on the surface. The second is the transport of adsorbed sulfur into the subsurface region of the copper that regenerates a clean surface.<sup>21</sup>

The work in Chapter 6 focuses on the gas-phase lubrication of copper by DMDS by pressurizing the UHV chamber while rubbing the copper sample. The work described in Chapter 4 and 5 identified the elementary-step reactions for the tribochemical reaction of DMDS, which rapidly forms adsorbed methyl thiolate species. This reaction cycle involves the shear-induced decomposition of methyl thiolate species to evolve small, gas-phase hydrocarbons and deposit sulfur on the surface, followed by a step in which sliding causes sulfur to be transported into the subsurface region of the sample, to regenerate clean surface sites. Continually repeating this

mechanochemical reaction cycle by pressurizing the sample while rubbing should result in the accumulation of a layer of sulfur in the subsurface region of the copper which provides a friction-reducing tribofilm. This can be viewed either as a tribochemical reaction that produces a friction-reducing film, or a model mechano-catalytic reaction in which surface chemistry and mechanical forces combine to induce a catalytic reaction that would not occur in the absence of the external force.

A combination of in-situ and ex-situ surface analytical techniques was used to identify the state and concentration of the sub-surface sulfur. It is likely that this model includes, perhaps with some modifications, the essential ingredients of mechanochemical reaction processes in general.

Chapter 7 is a description of the density functional theory (DFT) simulations of pulling a methyl thiolate molecule across a Cu (100) surface and climbing nudged elastic band (cNEB) calculations of the normal-force-induced decomposition of methyl thiolate on that surface. By combining the two processes, an understanding of how normal forces lower the activation energy is obtained and compared to the extended Bell model.

A quasi-static approach to force was used to simulate the effect of normal and lateral force on the decomposition of methyl thiolate on Cu (100). Atoms are moved step-wise through a range of motion and allowed to relax at each position to replicate sliding experiment speeds of  $\sim 10^{-7}$  Å/s. This speed is slow compared to the frequency of the atomic vibrations that determine the time-scale for the molecules to respond to force, which are  $\sim 10^{12}$ /s, therefore the quasi-static calculations in this chapter are a good approach to understanding the experimental results in Chapters 4-6.

Climbing Nudged Elastic Band (cNEB) calculations were done using a top slab of copper lowered toward a methyl-thiolate covered copper surface. The change in activation energy is

found as a function of normal force applied to the reactant and transition states by a copper slab and the result is compared to the extended-Bell model theory. To find the effect of shear on bond strength the methyl thiolate was moved step-wise in directions along and diagonal to the lattice vector across a Cu (100) surface after being tilted from the surface normal.

Chapter 8 explores the relationship between force, both normal and shear, on the decomposition of methyl thiolate species adsorbed on a copper foil by exploiting the relationships between area and force present at a plastic interface. Interfaces are difficult to study because they are ephemeral by nature with buried, nano-scale effects occurring within macroscale objects. In particular, a method of measuring the real contact area of a rough contact on a plastically-deformed surface is of interest to the tribology community because sliding interfaces have been found to be composed of asperities, and consequently the real contact area is smaller than the apparent contact area.<sup>22,23</sup> The decomposition of a marker molecule on the surface can provide useful information about the contact mechanics and surface structure of a contact during rubbing. In this chapter the nature of the contact is explored, an initial hypothesis is put forth and a set of experiments is presented as a proof-of-concept.

## References

1. Dong, Y., Vadakkepatt, A. & Martini, A. Analytical Models for Atomic Friction. *Tribol. Lett.* **44**, 367–386 (2011).
2. Urakaev, F. K. & Boldyrev, V. V. Mechanism and kinetics of mechanochemical processes in comminuting devices: 1. Theory. *Powder Technol.* **107**, 93–107 (2000).
3. Falconer, J. L. & Madix, R. J. The kinetics and mechanism of the autocatalytic decomposition of HCOOH on clean Ni(110). *Surf. Sci.* **46**, 473–504 (1974).
4. Yue, D.-C. *et al.* Tribochemistry of Phosphoric Acid Sheared between Quartz Surfaces: A Reactive Molecular Dynamics Study. *J. Phys. Chem. C* **117**, 25604–25614 (2013).
5. Furlong, O., Gao, F., Kotvis, P. & Tysoe, W. T. Understanding the tribological chemistry of chlorine-, sulfur- and phosphorus-containing additives. *Tribol. Int.* **40**, 699–708 (2007).
6. Liang, J. & Fernandez, J. M. Mechanochemistry: One Bond at a Time. *ACS Nano* **3**, 1628–1645 (2009).
7. Schwaderer, P. *et al.* Single-molecule measurement of the strength of a siloxane bond. *Langmuir* **24**, 1343–1349 (2008).
8. Ribas-Arino, J., Shiga, M. & Marx, D. Understanding Covalent Mechanochemistry. *Angew. Chemie Int. Ed.* **48**, 4190–4193 (2009).
9. Konôpka, M., Rousseau, R., Štich, I. & Marx, D. Detaching thiolates from copper and gold clusters: Which bonds to break? *J. Am. Chem. Soc.* **126**, 12103–12111 (2004).
10. Konôpka, M., Turanský, R., Dubecký, M., Marx, D. & Štich, I. Molecular

- mechanochemistry understood at the nanoscale: Thiolate interfaces and junctions with copper surfaces and clusters. *J. Phys. Chem. C* **113**, 8878–8887 (2009).
11. Holmberg, K., Andersson, P. & Erdemir, A. Global energy consumption due to friction in passenger cars. *Tribol. Int.* **47**, 221–234 (2012).
  12. Helt, J. M. & Batteas, J. D. Wear of Mica under Aqueous Environments: Direct Observation of Defect Nucleation by AFM. *Langmuir* **21**, 633–639 (2005).
  13. Felts, J. R. *et al.* Direct mechanochemical cleavage of functional groups from graphene. *Nat Commun* **6**, (2015).
  14. Li, Q., Tullis, T. E., Goldsby, D. & Carpick, R. W. Frictional ageing from interfacial bonding and the origins of rate and state friction. *Nature* **480**, 233–6 (2011).
  15. Seema, P., Behler, J. & Marx, D. Force-induced mechanical response of molecule-metal interfaces: molecular nanomechanics of propanethiolate self-assembled monolayers on Au(111). *Phys. Chem. Chem. Phys.* **15**, 16001–16011 (2013).
  16. Philippon, D. *et al.* Role of nascent metallic surfaces on the tribochemistry of phosphite lubricant additives. *Tribol. Int.* **44**, 684–691 (2011).
  17. Greiner, C., Felts, J. R., Dai, Z., King, W. P. & Carpick, R. W. Temperature Dependence of Nanoscale Friction Investigated with Thermal AFM Probes. *MRS Proc.* **1226**, 1226-NaN-2 (2009).
  18. Gao, F. *et al.* The tribological properties of monolayer KCl films on iron in ultrahigh vacuum: Modeling the extreme-pressure lubricating interface. *Tribol. Lett.* **14**, 99–104 (2003).

19. Rusanov, A. *et al.* Probing the tribochemical degradation of hydrogenated amorphous carbon using mechanically stimulated gas emission spectroscopy. *Carbon N. Y.* **81**, 788–799 (2015).
20. Rusanov, A., Nevshupa, R., Martin, J.-M., Garrido, M. Á. & Roman, E. Tribochemistry of hydrogenated amorphous carbon through analysis of Mechanically Stimulated Gas Emission. *Diam. Relat. Mater.* **55**, 32–40 (2015).
21. Miller, B., Furlong, O. & Tysoe, W. The Kinetics of Shear-Induced Boundary Film Formation from Dimethyl Disulfide on Copper. *Tribol. Lett.* **Submitted**, (2102).
22. Müser, M. H. *et al.* Meeting the Contact-Mechanics Challenge. *Tribol. Lett.* **65**, 118 (2017).
23. Luan, B. & Robbins, M. O. The breakdown of continuum models for mechanical contacts. *Nature* **435**, 929–32 (2005).

# Chapter 2

## Experimental Methods

### *2.1 Introduction*

This Chapter contains a brief description of the resources used to investigate tribochemical reactions and an outline of the principles behind the experimental technique. It is not intended as a thorough report of the inner workings of the equipment, there are many good resources on ultrahigh vacuum equipment when more information is needed.<sup>1-3,4</sup>

### *2.2 Vacuum equipment*

The work described in this dissertation was done in ultrahigh vacuum (UHV) chambers, that is, self-contained miniature laboratory in which the background pressure is in the  $10^{-10}$  Torr range. Ultrahigh vacuum system experiments have several advantages to those carried out in ambient atmosphere. First, it allows careful control of the type and number of molecules allowed to interact with the surface to provide control over the chemical reactions taking place without interference from the background. Second, in many cases low pressures allow molecules to desorb from the surface at relatively low temperatures, allowing desorption of reactants at temperatures below the decomposition thresholds for the compound of interest, thereby allowing reaction products to be detected. Third, the pressures of the desorbing species are much higher than the sum of the background pressure in ultrahigh vacuum. For example, a desorption experiment that causes an increase in pressure from gas-phase product evolution of  $1 \times 10^{-9}$  Torr provides an increase of total pressure of up to an order of magnitude over the background pressure in UHV,

whereas in atmosphere the same amount of gas production gives a change of approximately 1 part per trillion in the total gas molecules. Last, it allows for the use of electrons as spectroscopic probes due to the longer mean-free-path of particles at UHV pressures.

## **Pressure measurement**

Fundamental to the use of vacuum systems is the issue of accurately measuring pressure. For many experiments, the number of molecules and the rate of their introduction to the chamber have a profound effect on the results. Equipment designed to be used inside an ultra high vacuum chamber is, in many cases, only capable of operating within the high-vacuum regime, and therefore it is important to know the pressure in the system to protect delicate equipment.

An accurate and precise measure of the gas pressure of the system is a fundamental requirement for carrying out controlled, repeatable ultrahigh vacuum experiments. The next sections describe the workings of two kinds of commonly used pressure gauges.

## **Diaphragm gauges**

Diaphragm manometers are pressure gauges that work by a deformation of a diaphragm caused by a pressure differential on either side of it. In a digital system like the one shown in Figure 1, the diaphragm bends in response to pressure, and the change in conformation causes a change in resistance in the strain sensors attached to the diaphragm. This electrical signal is

converted to pressure by a calibration constant. A solid block is placed in the vacuum side of the

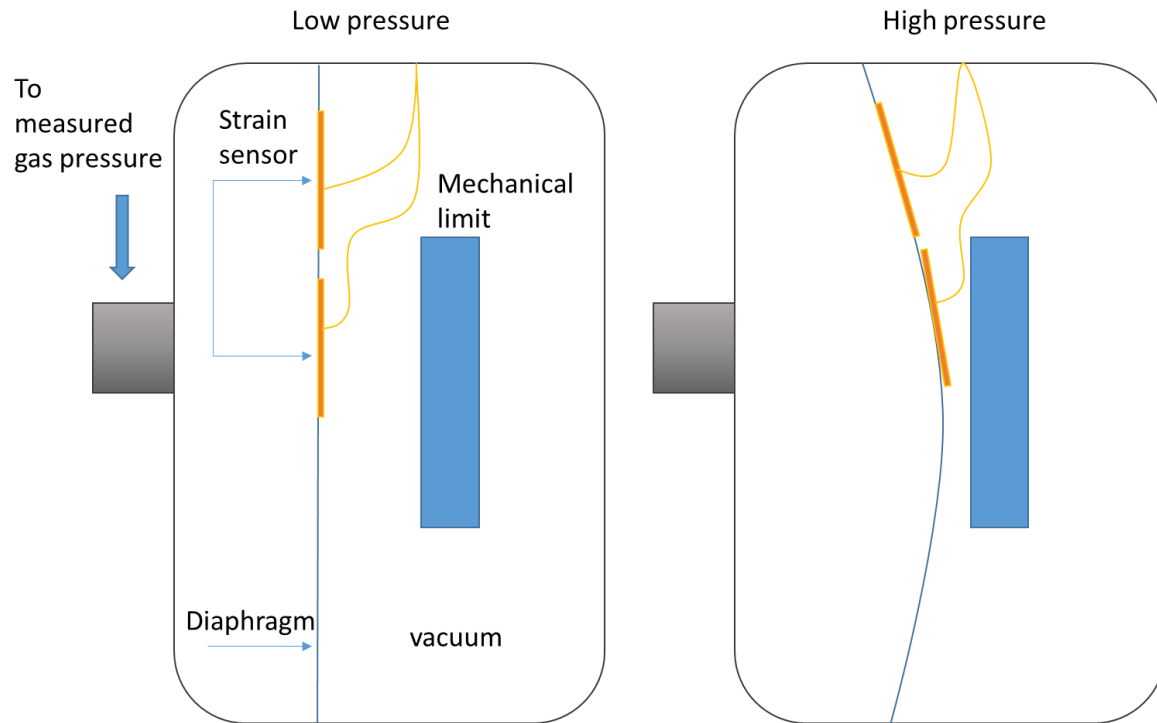


**Figure 2-1 Schematic of a diaphragm gauge of a system at low (left) and high (right) pressure**

gauge to relieve strain from the diaphragm and prolong the life of the gauge.

Diaphragm gauges have the benefits of being insensitive to the type of gas and operate over a wide range of pressures. A typical range for an electric diaphragm gauges is from ~millitorr to 1000 Torr and the gauge can be made to work over a variety of ranges, but the sensitivity suffers if the range becomes too large. A diaphragm gauge is used to monitor the pressure of the gas-handling line, but cannot be used to read pressures inside a UHV chamber. The material of the diaphragm must be such that it responds to pressure differential across the diaphragm by changing shape. As the pressure differential decreases, the diaphragm must be thinner and more flexible and ultimately the pressure can become low enough so there is no practical material capable of a readable response.

## Ionization gauges

Ionization gauges operate at very low pressures because they function using hot filaments that eject electrons, rather than the collective action used in diaphragm gauges.

The first ionization gauge was designed Alpert, and then further design work was done to increase the sensitivity by Alpert, Bayard, and Nottingham<sup>4</sup>. A schematic of an ion gauge is shown in Figure 2. An ionization gauge consists of a filament, usually tungsten or tantalum, a metal grid, and a collector. A positive potential is applied to the grid and electrons ejected from the hot

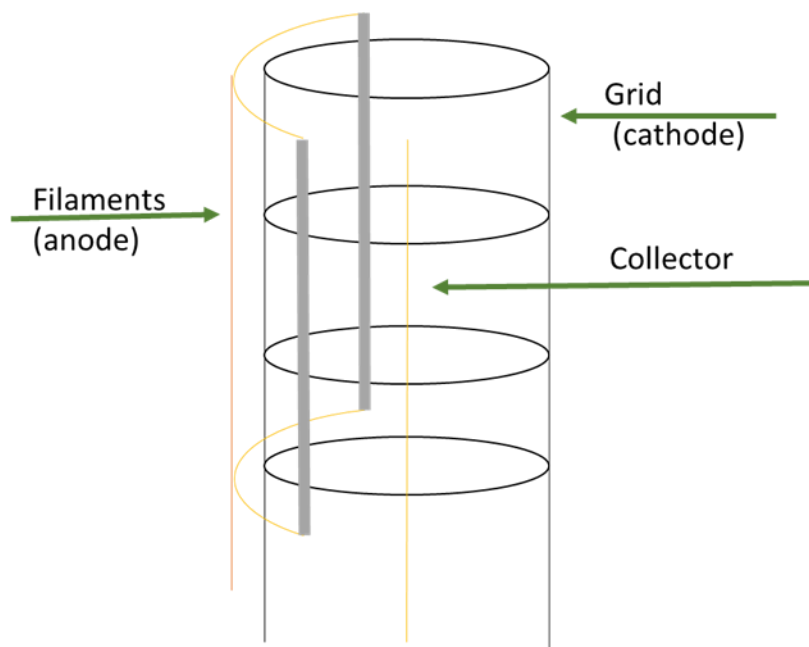


**Figure 2-2 Ion gauge schematic showing the filament, grid and collector**

filament are drawn to the grid. On the way, the electrons collide with gas molecules to form positive ions, which are then drawn to the anode by a negative bias. This produces a flow of charge to the collector and a resulting current, which can be measured and converted to pressure.

The current produced by the collisions of the ion with the collector depends on the probability that the electrons from the filament will encounter a gas molecule on their path to the grid and the probability that encounter will result in an ion. The probability of an ionization event occurring is dependent on the type of molecule and its ionization potential. This ionization factor,  $\alpha$ , varies significantly between gases. This makes absolute pressure measurement difficult, as most

chambers have a mixture of gases present. In this work it is assumed that the gases in the chamber have the same sensitivity as nitrogen so that pressures are not corrected for these sensitivity factors.

The probability of collision between an electron and a gas molecule,  $L$ , is directly proportional to the collector current and depends on the distance the electron travels from the filament to the grid,  $l$ , and the number of molecules in the chamber,  $N$ .

$$L = \frac{l}{N} \quad (1)$$

Conversion of the number of molecules to pressure uses the density of the molecules,  $\rho$  and the probability of the gas ionizing as a function of the filament current. The volume between the filament and the grid is a fundamental part of the gauge design and is used as the volume that the atoms occupy when being converted. The filament current,  $i_e$ , is also controlled by the gauge and is some known constant,  $\alpha$  is the sensitivity constant, and  $L$  is the number of ionization events given in equation 1. These factors give equation 2, which shows the current at the collector is proportional to the density of gas and the ionization sensitivity.

$$i = i_e \rho \alpha L \quad (2)$$

Assuming an average value for the ionization energy allows us to account for that factor, and so the current at the collector is then a sensitivity factor,  $S$ , multiplied by the number of molecules per unit volume in the chamber, and can be easily converted to pressure with a conversion factor dependent on the pressure units,  $P$ . In this work the pressure is given in Torr and it is assumed that the gases in the chamber have the same sensitivity as nitrogen and equation 3 is used related to the current to pressure in the Bayert-Alpert ionization gauge.

$$i = Si_e P \quad (3)$$

## Attaining low pressure

Ultrahigh vacuum is achieved through several stages of pumping because it is not generally possible to decrease the pressure from atmosphere to the ultra high vacuum regime using a single pump. The ultrahigh vacuum here was achieved using a series of pumps: mechanical, diffusion, turbo-molecular, and ion pumps to attain ultimate background pressures in the  $10^{-10}$  Torr range. Figure 3 shows a graph of pumping speed in L/s versus pressure in Torr for various types of vacuum pump, and a discussion of the benefits and drawbacks of each type of pump is given in the following section.

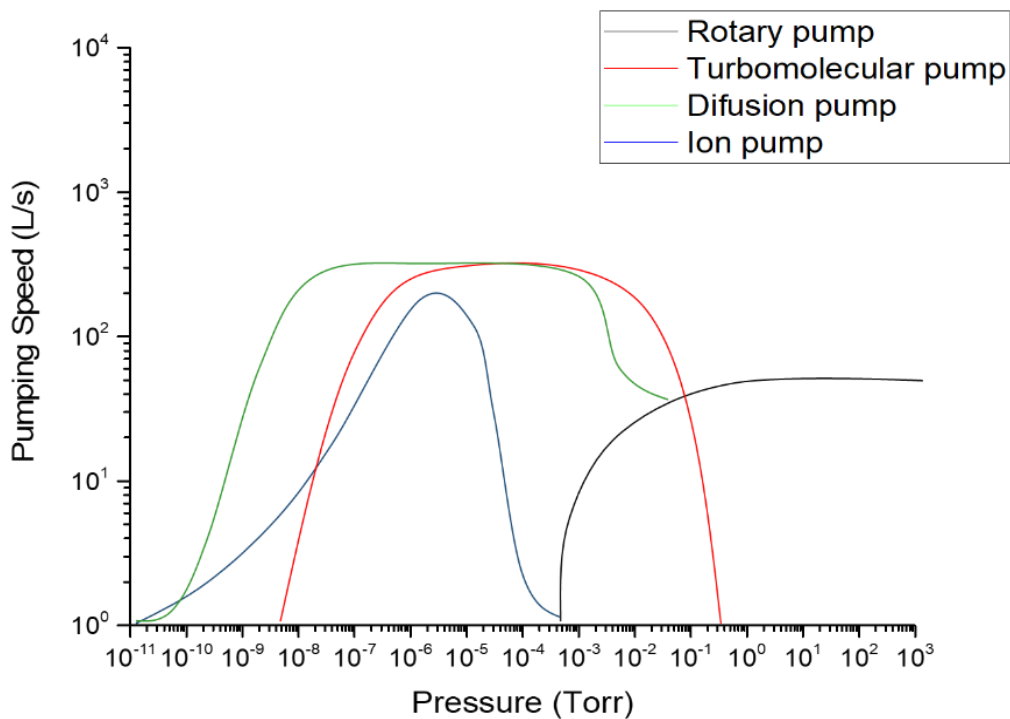


**Figure 2-3** Graph with curves representing typical pumping speeds versus pressure for the pumps discussed in this work. Black - rotary pump, red - turbo pump, green - diffusion pump and blue - ion pump

## Mechanical pumps

Mechanical pumps function by gases expanding into a cavity that is being opened and swept out by a stator with movable blades and shown in Figure 4 (A). As the stator moves, it traps the gas from the inlet and compresses it until it reaches the outlet valve. Once the pressure on the outlet valve becomes sufficiently large to force the valve open, the gas is expelled. Rotary pumps require oil to lubricate the stator and this oil can become contaminated by the vapors of volatile liquids, causing a loss of efficiency as they evaporate during pumping. In this case, air is leaked into the pump through a “ballast” to displace the vapor from the oil. This can take a considerable amount of time in the case of non-polar liquids that mix well with the oil.

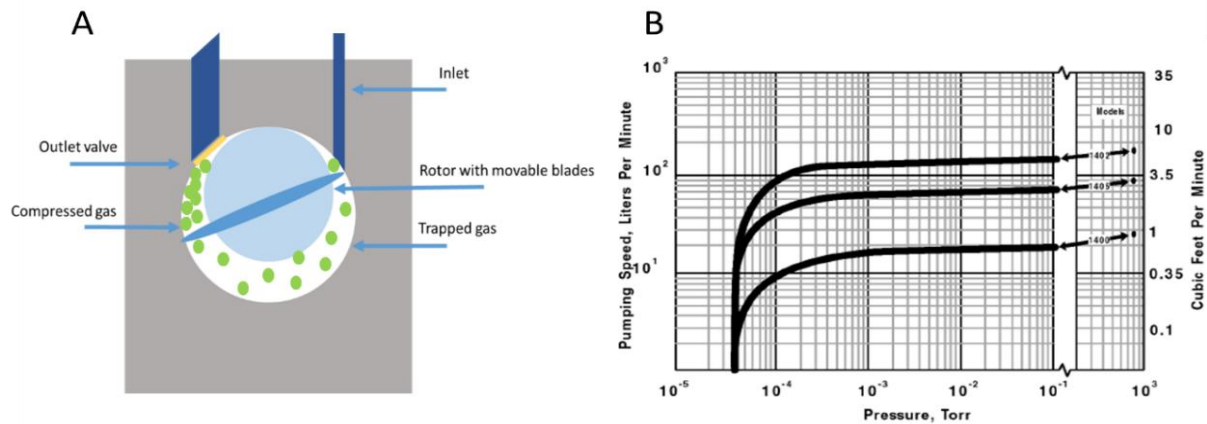


**Figure 2-4 A) Mechanical pump schematic and B) Welch Vacuum graph of pumping speed versus Pressure for the Welch Duo seal pump users from the manual reprinted with permission from Welch Vacuum Corp**

Rotary pumps are robust, but limited to relatively high pressures of gas being pumped because a sufficiently-high pressure in the compression phase is required to open the outlet valve.

This means that it cannot attain pressures below the millitorr range, as shown in Figure 4 (B).<sup>5</sup> Pressures lower than that can be obtained using a turbo molecular or diffusion pump as discussed in the next sections.

## Turbo-molecular pumps

Turbo-molecular, or “turbo”, pumps can be used to decrease the pressure of a system below the millitorr range and a diagram and of the pumping speed versus pressure variation are displayed

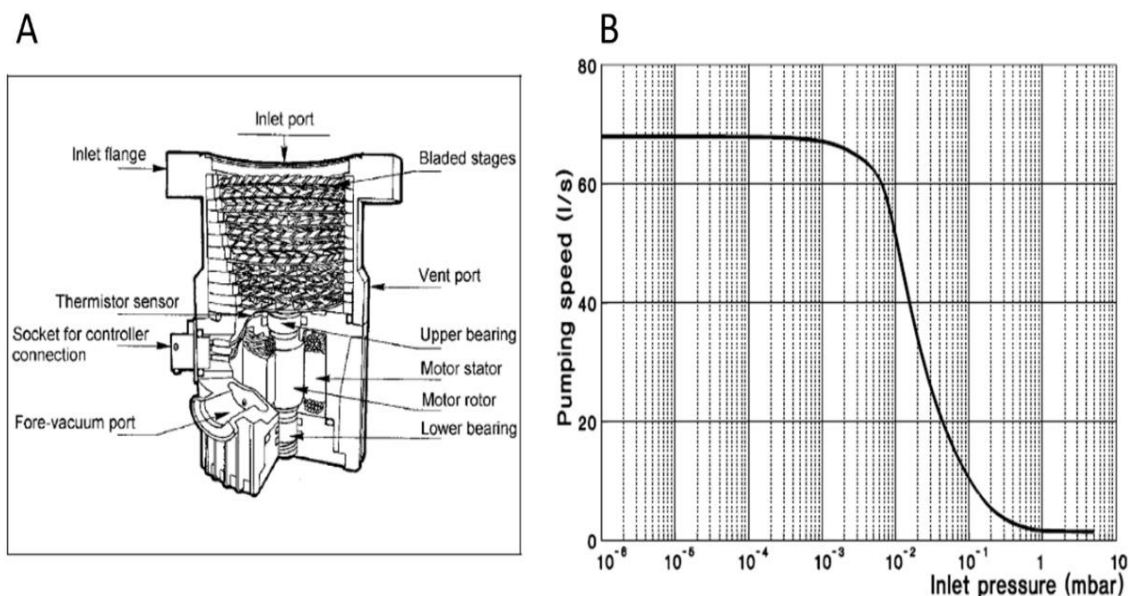


**Figure 2-5 Turbo pump diagram from Varian V-70 turbo pump manual. (B) Pumping speed versus inlet pressure for Varian turbo pump from Varian v-70 turbo pump manual. Reprinted with permission from Varian**

in Figures 5 A and B. Turbo pumps operate using a series of spinning fins that collide with gas molecules and push them to the next set of fins, and finally to the backing pump, generally a mechanical pump and their major advantage compared to diffusion pumps (see next section) is that they operate without oil, which can contaminate a UHV chamber. The fins spin at up to 75,000

rpm and each set of fins is canted at a smaller angle than the previous set to prevent gas migration back through the pump.

Turbo pumps do not work well at pressures above tens of millitorr, as seen from the graph in Figure 5(B). Pressures above that range allow too many gas molecules to hit the fins, slowing them down, or worse, knocking the bladed stages off their bearings. It is clear from the graph that the turbo pump does not pump effectively in the pressure regime above  $10^{-3}$  mbar, and sudden exposure to pressure above  $10^{-3}$  mbar while the blades are spinning can cause catastrophic damage.

Care must be taken with turbo pumps as they require a backing pump to lower the pressure on the outlet. If the backing pump fails, the turbo will also fail, causing damage, and allowing a stream of oil from the backing pump to contaminate the chamber.

Another limitation of this pump is its poor pumping of hydrogen. The hydrogen molecule is small enough to diffuse back through the fins and is not easily pumped from the chamber by turbomolecular pumps.

Finally, the low-pressure limit for turbo pumps is reached when the movement of gas becomes fully molecular, rather than flow-based. When too few molecules move together to allow liquid flow, each gas molecule must contact the blade to be pushed in the direction of the exhaust. The pumping mechanism becomes a pure scattering and the probability of back scattering into the chamber is only slightly lower (due to the angle of the blades) than the probability of scattering into the pump and being removed from the system.<sup>6</sup>

## **Diffusion Pumps**

If the pressure of the chamber is low then pressure gradients, which enable the gas to diffuse toward an outlet, are too small to be effective. Below the pressure in which gases can be

said to “flow,” diffusion and ion pumps work by collisions between the pump and the gas molecules. The first pump of this kind discussed is the diffusion pump and is pictured in Figure 6 (A).

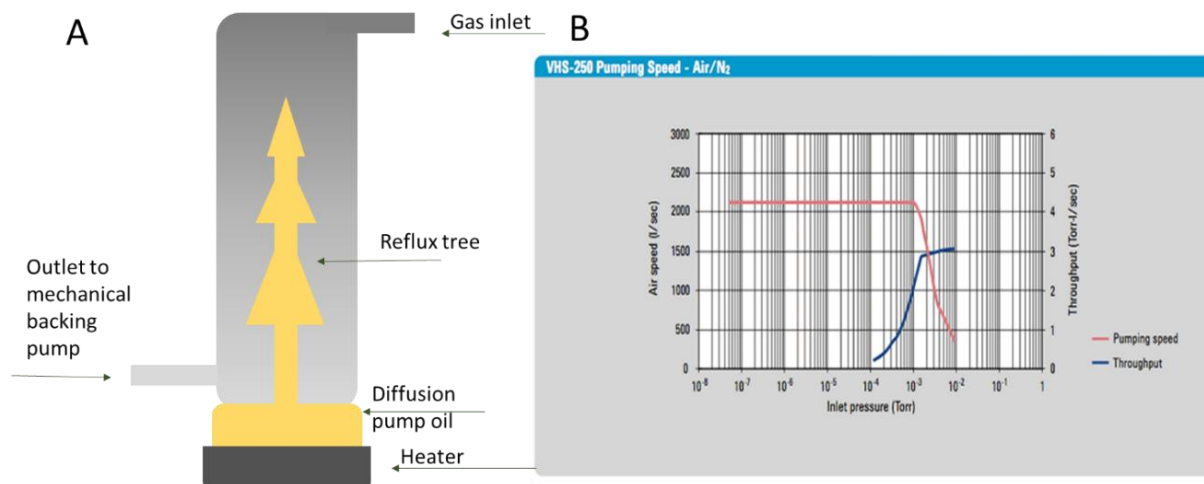


**Figure 2-6 Schematic of a diffusion pump. Cooling lines are not shown. Diffusion pumping speed graph versus pressure is shown from an Agilent Diffusion pump description. Reprinted with permission**

Diffusion pumps function by refluxing oil that cascades down a set of angled pieces of metal or glass, known as a “Christmas tree” as it recondenses, causing oil molecules at the top of the tree to form an “umbrella” of liquid that moves at faster than the speed of sound. The condensation of oil by the tree is aided by water cooling. As the molecules of oil descend, they collide with gas molecules in the background and the fast-moving particles lower the pressure above them while preventing back migration of the pumped gases. In addition, a liquid nitrogen trap can be added to the inlet of the diffusion pump, which acts to prevent oil from back-streaming into the chamber. A rotary backing pump keeps the pressure directly above the oil sufficiently low to allow it to reflux.

The diffusion pump in this work was used to pump gases being introduced to the chamber from a glass gas-handling line. The pressure did not need to be in the UHV range and so no water cooling or liquid nitrogen trap was needed on the diffusion pump and the pump was air-cooled.

The advantage to diffusion pumps is that they pump small, relatively inactive molecules like hydrogen. They continue to pump to very low pressure and at their upper pressure limit the backing pump takes over, as seen in Figure 6(B).

The limitations of diffusion pumps are both the high-pumping speeds, which is not desirable for every experiment, and the catastrophic consequences of their potential failure. For example, failure of the cooling system can cause hot oil to spray over the chamber. Failure of the backing pump can cause contaminants to build up in the oil, oxidizing it and causing the physical properties of the oil to change. Most alarmingly, if the hot oil encounters oxygen, the pump can explode.

## **Ion Pump**

The lowest pressures attained for the work described in this dissertation were achieved by an ion pump. The benefit of ion pumps over diffusion pumps is that ion pumps do not use oil and pump failures are not dangerous or likely to cause contamination of the chamber.

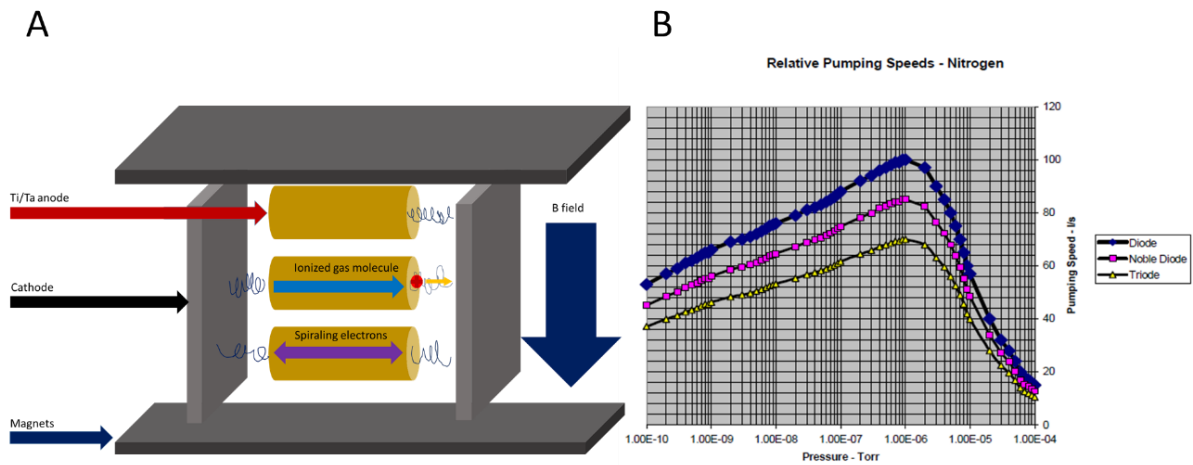


**Figure 2-7 (A) Ion pump diagram. (B) Pumping speed versus pressure for diode, noble diode and triode ion pumps**

Ion pumps operate by ionizing the gas molecules to be pumped and accelerating them toward metal plates where the ions are chemically or physically trapped. The design is based on that of ion gauges described earlier and ion pumps were developed by Alpert in conjunction with Penning,<sup>4</sup> which allows many ion pumps to simultaneously act as a pressure gauge and vacuum pump. A schematic of an ion pump is shown in Figure 7(A). Gas molecules are ionized by the high electric fields in a process known as Penning ionization and metal cylinders or wires shaped into tubes act as anodes. Electrons are trapped inside the anodes by cathodes on either end. The electrons are induced to move in a spiral by a magnetic field supplied by large magnets in the outer case of the pump, which increases their total path, enabling them to collide with more molecules to improve pumping speed. The spiraling electrons and ions collide with gas molecules which are then ionized and accelerate towards the cathode. The ions are captured by the cathode, which is typically made of titanium. The ions can be trapped by reacting with the titanium metal plates, by being buried in the metal due to the momentum of the ion, or by sputtering highly reactive titanium

atoms from the surface and reacting with those atoms to form a metal organic compound that adsorbs onto the titanium plates.

Due to the sacrificial nature of the titanium surfaces and voltages that are high enough to cause arcing in air, ion pumps can only be used below the millitorr range, as shown in Figure 7(B). Another limitation is poor pumping of noble gases and hydrogen. Even when ionized, noble gases do not react with the titanium metal surfaces, so that the only method of pumping inert gases such as argon is to bury them in the titanium plates with the momentum supplied by the high voltage. This causes an increase in the temperature in the cathode, which then causes the argon atoms, as well as other gases, to be released. Hydrogen has a high affinity for titanium and can diffuse into metals, but since diffusion is a reversible process, it is also not pumped effectively.<sup>7</sup>

### ***2.3 UHV Chambers***

The base materials of chambers intended for UHV work must be carefully considered order to maintain the tight control of the environment in UHV chambers.

#### **Chamber body**

The body of the chamber is made of 1/8" thick, 304 or 316 stainless steel. The chamber material must have an extremely low vapor pressure, have a high melting or sublimation temperature, and be chemically inert. Carbonaceous steel, or any alloy that includes zinc, lead, most plastics and all glues must be avoided in UHV systems.

Even relatively inert stainless-steel chambers accumulate gas, especially water, on the walls of the chamber when exposed to atmosphere. These adsorbates will slowly desorb and be pumped away, leading to extended periods of higher than desired pressures. To increase the rate of adsorbate, particularly water, desorption, the chamber is heated by wrapping it in heating wire

and heating to 130-150 °C for 24 to 36 hours in a process referred to as baking. This procedure is required every time the chamber is opened to atmosphere.

## Flanges

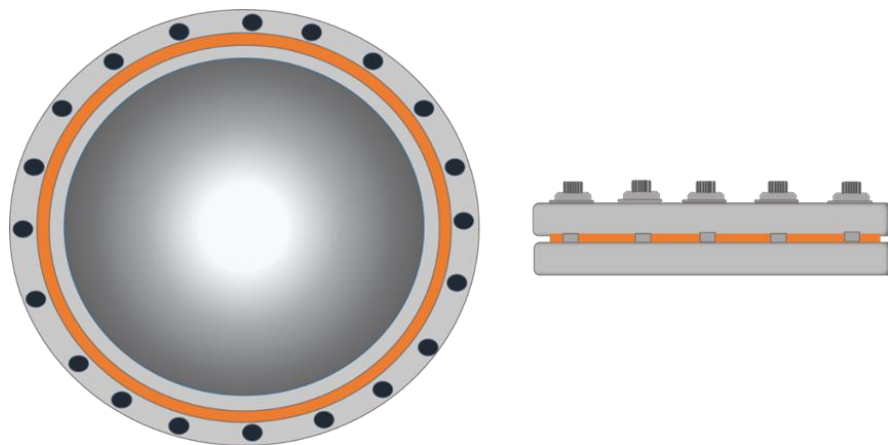


*Figure 2-8 Top (left) and side (right) view of a conflat flange*

The chamber is fabricated with various ports of standard sizes to allow attachment of sample manipulators, instruments, pumps, and leak valves. Flanges are made of thick stainless steel, and the

flange is sealed to the port with low-oxygen copper gaskets to provide a seal. The copper plastically deforms by pressure from a knife edge on each flange to provide a conformal contact between surfaces. A schematic is shown in Figure 8. This design is called a Con-flat flange and is effective, but each copper gasket can only be used once due to deformation and work hardening during use. Tightening the bolts in a star pattern twice and then going once around the perimeter is recommended to uniformly compress the copper and obtain a good vacuum seal.

## *Working in UHV*

Ultrahigh vacuum (UHV), is used to create an environment to study surface chemical systems of tribological interest. To carry out experiments in UHV, metal samples, reactants, motion, and electrical power must be introduced into the UHV system.

## Metal Sample

The copper foil, the most commonly used substrate in this work, was transferred into the chamber by opening the chamber. The sample is attached to a manipulator that allows rotary, as well as x, y, and z linear motion. A ceramic rod thermally and electrically isolates the sample from the chamber and is clamped using a tension fit and bolts. As shown in Figure 9, tantalum rods

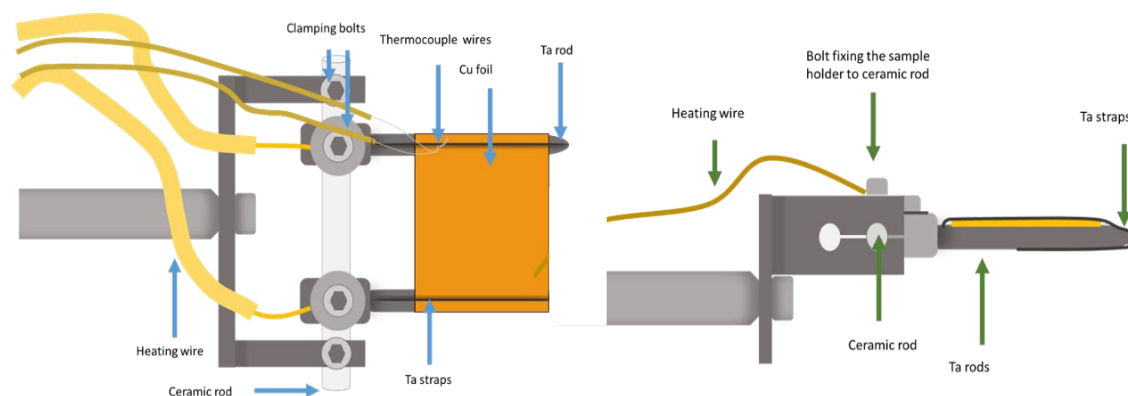


**Figure 2-9** Top(left) and side (right) view of the sample holder with a copper foil sample mounted on tantalum rods with heating wires and thermocouple attached.

support the sample and tantalum straps secure it to the rods to prevent movement of the sample during experiments.

Resistive heating of the sample is used to increase the temperature, and the temperature is measured using a thermocouple attached to the sample by spot-welding and welding it to the sample holder under tantalum straps to prevent movement. The heating and thermocouple wires are insulated to prevent them from grounding to the chamber or shorting to each other.

## Introducing Gaseous Reactants

Gases and the vapors of volatile liquids are introduced to the chamber via leak valves attached to a glass gas-handling line. The gas line consists of a glass tube with valves attached to it that allow the line to be pumped, first by a rotary pump, and then to lower pressures by a diffusion

pump. The rotary pump backs the diffusion pump when it is not used for rough pumping the line, and the valves that control the pumping are set so that the rotary pump is open to the diffusion pump but closed to the gas line when the line is not being actively pumped by the rotary pump to maintain a low pressure on the diffusion pump. Figure 10 shows a schematic diagram of the gas line used in this work.

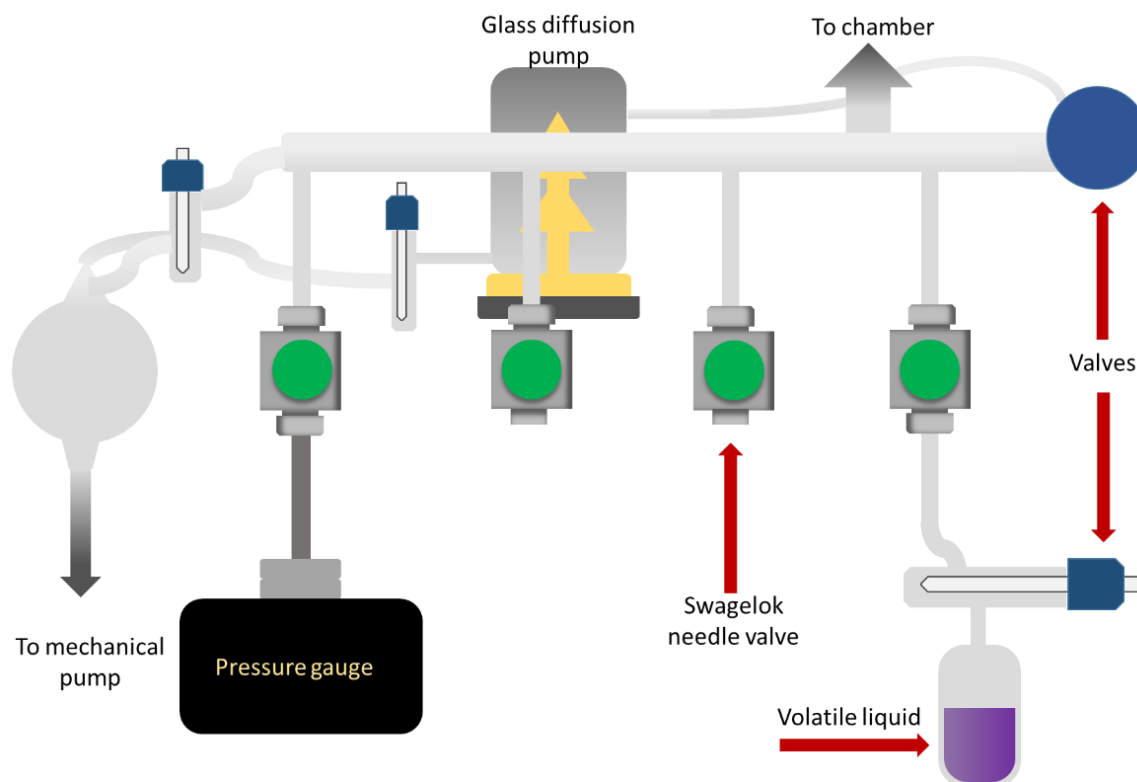


**Figure 2-10 Diagram of the gas-handling line**

Teflon tubes connected to gas cylinders, or glass vials containing volatile liquids, are attached to the gas line via Swagelok valves. A diaphragm pressure gauge with a range from 1000 Torr to 1 mTorr monitors the pressure in the gas-handling line.

## Leak valves

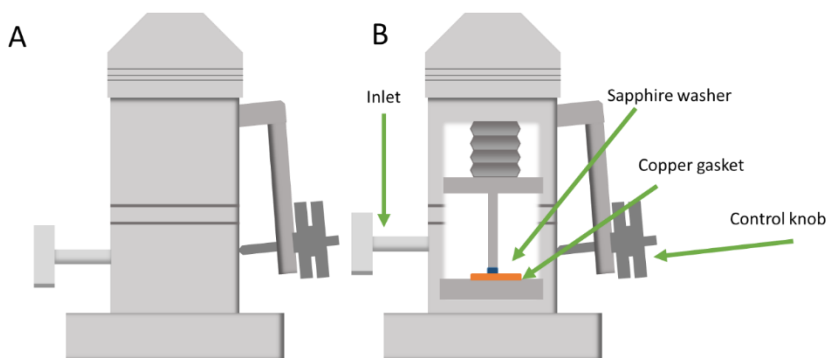


**Figure 2-11** Drawing of *A) outer and B) inner workings of a typical leak valve*

Leak valves allow the controlled introduction of molecules and atoms from the gas line to the UHV chamber by allowing precise control of the chamber pressure as

shown in Figure 11 (A). Fine control of the gas flow is accomplished by lowering a shaft with a sapphire washer on to the end of a copper gasket as shown in Figure 11 (B). The copper gasket will eventually lose elasticity that allows the conformational contact and eventually cause leaks with repeated use. Exposing the leak valve to air when the chamber is baking will oxidize the copper gasket and speed the hardening process, lowering precision.

## Linear motion

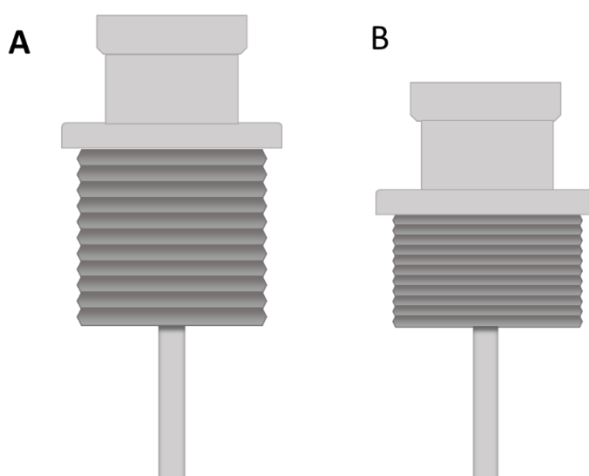


**Figure 2-12** Linear motion feed through in the retracted (A) and extended (B) positions

Transferring motion to the inside of the vacuum chamber, while keeping the inside separate from the atmosphere, is accomplished by encasing the moving parts in a flexible bellows that can be compressed to translate a rod in and out of the chamber. These are somewhat prone to leaking after years of use and it is a good idea to check them for leaks if

one is suspected. Figure 12 shows representations of a retracted and extended linear motion feedthroughs.

## Rotary motion

Rotary motion requires a universal joint to transfer torque without twisting the bellows that isolates the chamber from atmosphere. When the end is rotated, the universal joint revolves around the center of the shaft, forcing it to rotate inside a bellows, as shown in Figure 12.

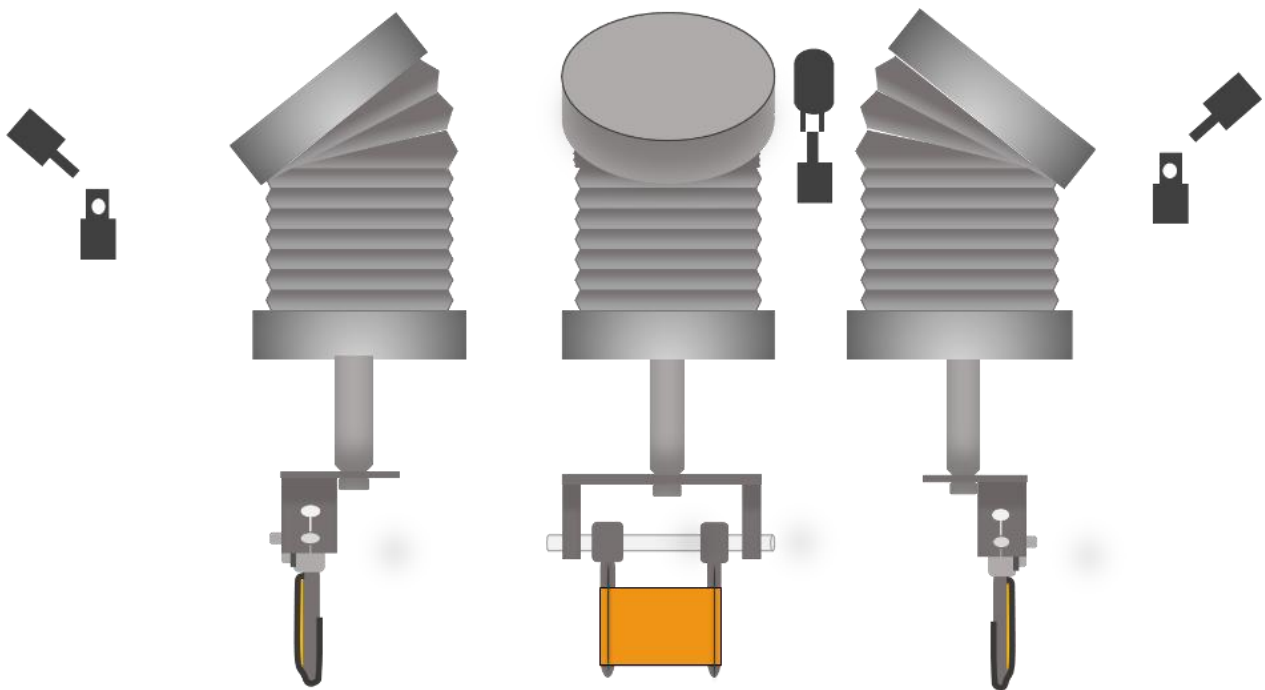


*Figure 2-13 Rotary motion feedthrough with universal joint*

## Electricity

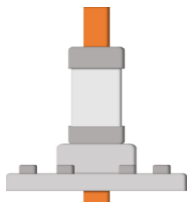


*Figure 2-14 Copper feedthrough with ceramic insulation on a conflat flange*

It is often necessary to introduce electrical power into the vacuum system, for example, to resistively heat the sample, however, the metal of the vacuum chamber must be isolated from the current-carrying conductor and is

accomplished by using a ceramic insulator attached to the feedthrough and sealed to a metal cap. The ceramics can develop leaks if they experience collisions or strain and are a good place to check for leaks.

## ***2.4 Instruments***

The elemental composition of the surface of the copper sample was analyzed using Auger Electron Spectroscopy (AES), the gases evolved from the surface were monitored by a quadrupole mass spectrometer, and the friction of the sample was monitored by a custom-built tribometer. The next sections describe those techniques and the instruments for measuring them.

### **Auger Electron Spectroscopy**

Auger electron spectroscopy, or AES, is a surface analytic technique because it relies on electrons which only penetrate a small distance into the sample. Electrons are accelerated toward the surface from an electron gun with an energy of several kilovolts, either from an axial gun included in the electron-energy analyzer or one mounted to the chamber at an angle above the Auger electron analyzer. The high-energy primary electrons cause inner shell electrons in the atoms of the sample to be ejected from atoms on the surface. The newly vacant inner shell energy levels in the ionized atoms are then filled by the decay of outer-shell electrons. The energy gained by this transition can be released either by emitting an x-ray or by ejection of another, so-called Auger, electron. The ejected electron has a kinetic energy that depends only on the energy levels of the atoms and so is insensitive to fluctuations in the energy of the incident electrons, if that energy is sufficient to eject a core electron. For example, in one of the copper Auger signals, (Figure 15) the K shell and the  $L_1$  shell and excess energy is dissipated by emission of an  $L_{2,3}$  electron and the calculated kinetic energy of the emitted electron is given by equation 4, where the

work function,  $\Phi$ , is included to account for the energy required to remove an electron from the sample.

$$K.E = E_K - E_{L1} - E_{L2,3} - \Phi \quad (4)$$

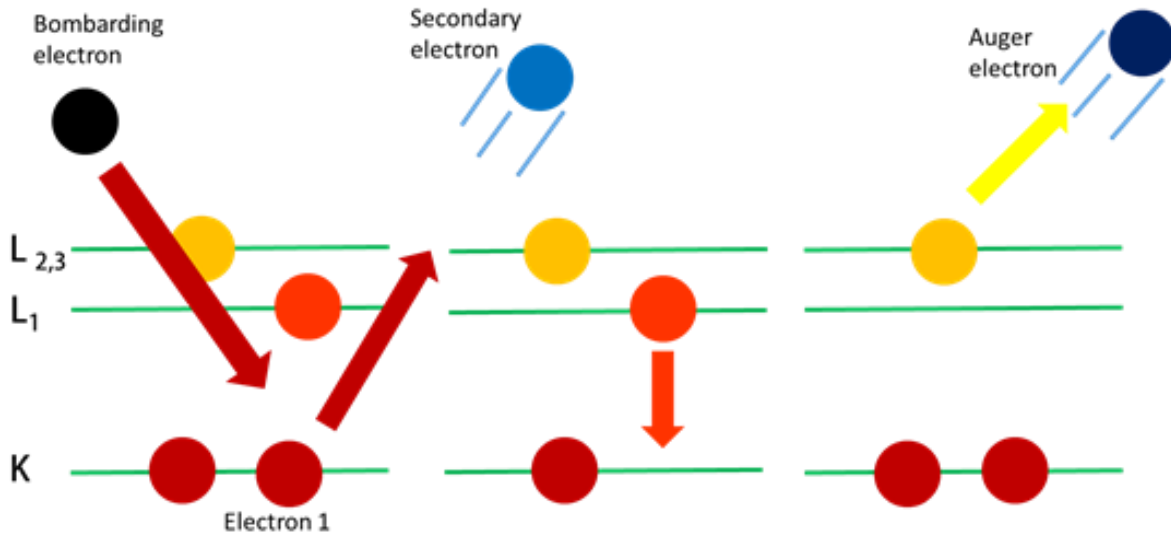


**Figure 2-15 Diagram of the ejection of a KLL Auger electron. The primary electron is shown in black, shell electrons go from yellow to red, secondary electrons are light blue and Auger electron is dark blue**

The energies of the electrons ejected from the sample are analyzed by a cylindrical mirror analyzer, or CMA shown in Figure 16, showing a Phi Electronics model 10-150. The CMA functions by applying a voltage difference between two concentric cylinders; the inner cylinder is grounded, while the outer cylinder has a positive potential applied to it such that the electrons follow a curved path between the two cylinders to pass through slits in the inner cylinder, which selects for electrons with a given energy. The electrons are detected by an electron multiplier. Electrons outside the desired energy will collide with one of the two cylinders, rather than passing through slits to complete the path to the detector.

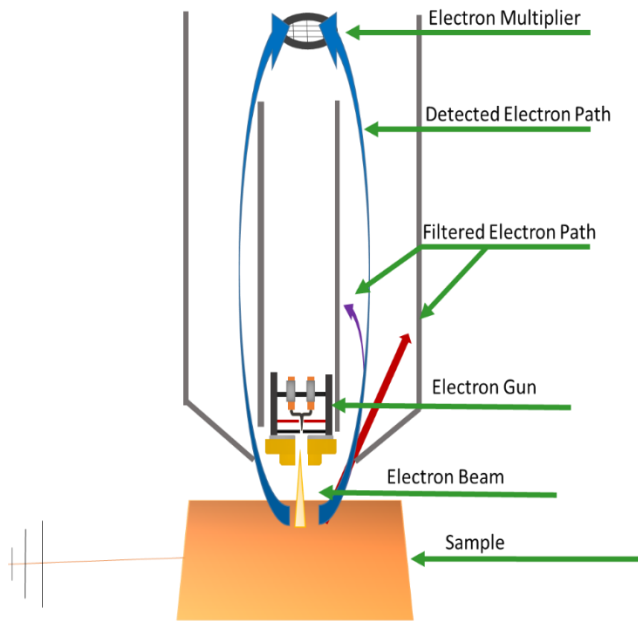


**Figure 2-16 Auger spectroscopy system composed of cylindrical mirror analyzer, electron gun, and detector.**

The electron multiplier operates by an electron cascade mechanism, in which a single electron causes the ejection of several electrons from the walls of the multiplier. The ejected electrons collide once again with the walls of the multiplier, causing even more electrons to be ejected. This continues until the electrons reach the end of the multiplier and are read as a current which is proportional to the number of electron

collisions that caused the cascade.

## Mass Spectrometer

A mass spectrometer was used to detect species desorbing from the sample, to analyze background gases and for leak detection using a UTI 100 mass spectrometer to monitor gas-phase molecules within the chamber. A mass spectrometer operates by ionizing molecules by an electron beam with an energy generally of  $\sim 70$  eV that are emitted from a filament, in a similar manner to the electron gun and ion gauge, described in previous sections. J.J. Thompson found that these ions could be separated spatially by applying an electric field.<sup>4</sup>

The ions formed by electron collision are accelerated into a quadrupole mass filter where ions of a specific mass to charge ratio are selected. Figure 17 shows a schematic diagram of how a quadrupole mass spectrometer operates by applying a voltage that varies with a frequency in the radio-wave frequency regime to four rods. As the ions are accelerated toward one rod, the rod

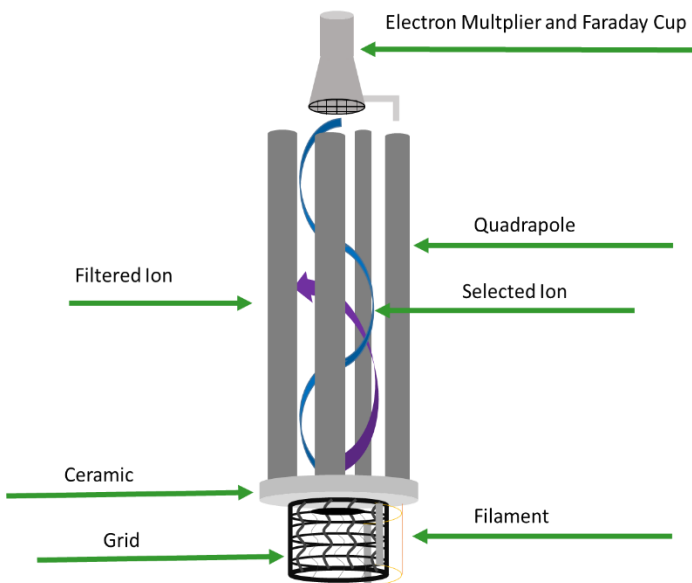


**Figure 2-17 Quadrupole mass spectrometer diagram**

shifts voltage, and the ions are repelled. If the ion has a high mass-to-charge ratio, then the change in voltage will not slow it in time to avoid a collision with the rods, due to the large momentum. If the ion has a low mass to charge ratio it will accelerate too quickly and collide with the rod. Selected ions can travel through the rods in resonance with the applied frequency. In this way the

quadrupole filters out undesired ions from the analyte stream before they are collected by the multiplier. The ions are detected either by the Faraday cup or by an electron multiplier.

## Ultrahigh Vacuum Tribometer

A tribometer applies a normal load to the sample surface via a ball contact and measures the friction coefficient, the ratio of the lateral force to normal load. The tribometer used in this dissertation is a UHV-compatible, custom-built instrument. The tribometer has an arm that moves the contact ball at a precise speed, apply precisely controlled loads, and sense the resulting lateral force on the arm.

The tribometer motion is controlled by stepper motors located outside the chamber that can position the arm at a specified location using custom-designed software. Motion limits of the arm are calibrated by moving it over a range defined by the size and location of the sample. The

software determines the arm calibration by counting the number of steps to reach the edges of the calibrated zone. This calibration allows the arm to precisely travel to the same position.

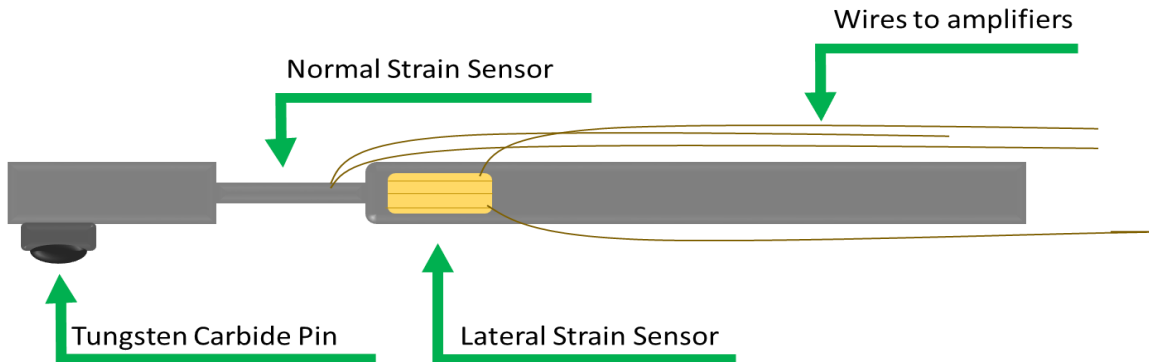


**Figure 2-18 Tribometer Arm with strain sensors**

Figure 18 shows the tribometer arm. The load is applied by bringing a tungsten carbide ball of 9.5 mm in diameter into contact with the sample surface. The force is measured by strain gauges attached to thinned portion of the arm of the tribometer. The tribometer signal is amplified by an external amplifier, and then read by the software via a National Instruments data acquisition (DAQ) board. Once a specified load has been reached, the motion of the arm stops. Sliding is then initiated at a preset sliding speed at the specified load, and the lateral force is measured by strain gauges, also attached to thinned portions of the arm. The software collects the lateral and normal forces as a function of time, which can be used to find the friction coefficient with the equation,  $F = \mu N$ , where  $F$  is the friction force,  $N$  is the normal force, and  $\mu$  is the friction coefficient.

## **2.5 Experimental Protocols**

### **Liquid-Sample Purification**

Volatile liquids must be purified before use and is accomplished by freeze-pump-thaw cycles, where the liquid is frozen by immersing the vial in a bath of liquid nitrogen. The solid is

pumped to remove any air and, as the solid warms and thaws, dissolved impurities are removed. The process repeated until the pressure gauge shows a slow increase in pressure as the liquid warms. It is important to note that this process does not necessarily completely purify the liquid because any contaminant with a lower vapor pressure would remain in solution.

## Sample Cleaning

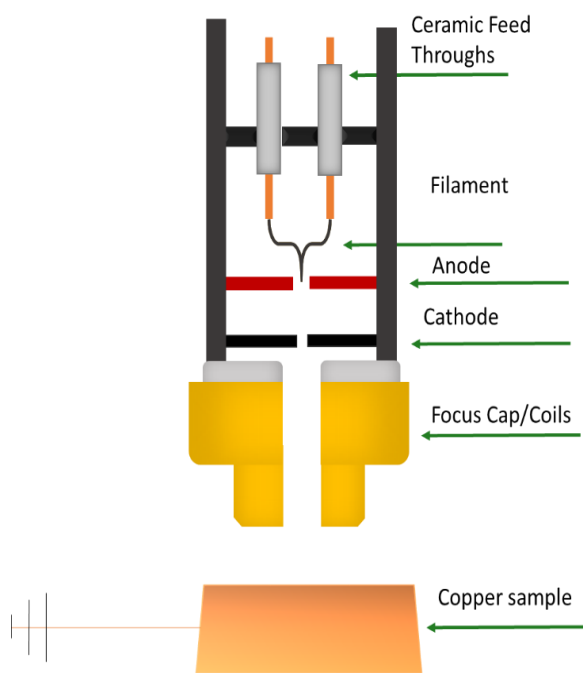


**Figure 2-19 Diagram of an ion gun**

Copper foils were used as the substrate in this work and were cleaned by cycles of argon ion bombardment and annealing. Argon ion bombardment is carried out by an ion gun, Figure 18, which consists of a filament that emits electrons that are accelerated so that argon atoms are ionized by collision. The ions are then accelerated through a one kilovolt potential by charged plates, one of which contains a hole to allow ions to pass through. The ions pass through an electric lens to focus

them onto the sample.

The sample is grounded to avoid charge build-up. The ions impact the grounded copper sample and remove contaminants from the surface by momentum transfer. The surface is roughened by this process and may be annealed to recrystallize the sample and allow contaminants to diffuse to the surface from the bulk. Several rounds of bombardment and annealing are generally required to obtain a clean metal sample, and the surface cleanliness is assessed by Auger spectroscopy.

## Aligning the Sample in the Tribometer

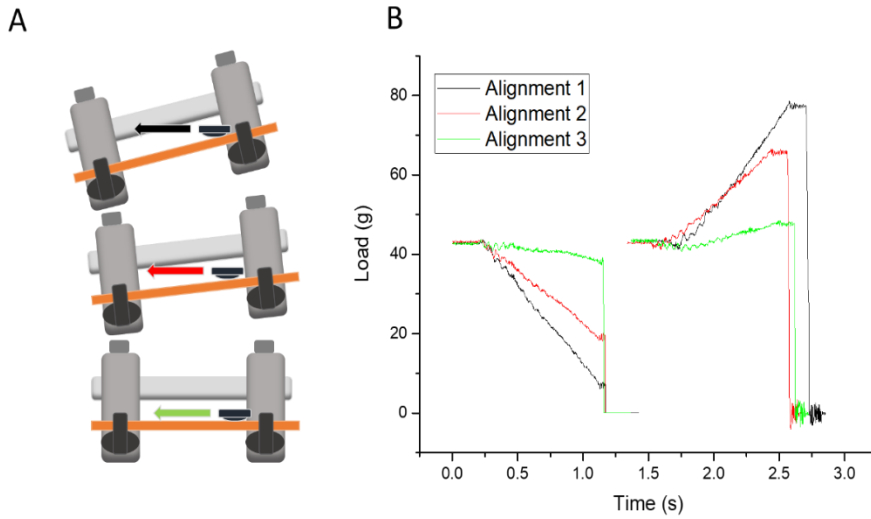


**Figure 2-20A) representation of the sample alignment with respect to the direction of travel of the tip. B) graphs of load versus time for a reciprocal slide of the tribometer pin as the sample is corrected from far out of alignment, black line, to better aligned, red line, to green line, where the sample is parallel to the path of the pin**

The sample must be aligned parallel to the motion of the pin to ensure that the load is constant during sliding. If a viewing window is available, the first step is to orient the sample visually. Further refinement can be

made by measuring the load as the pin passes across the surface. Adjustments to the sample are made until the load read by the tribometer strain gauge is constant during translation across the surface. Figure 20 A demonstrates the path of the pin with respect to the surface depending on sample angle. Figure 20 B shows the resulting graphs of load versus position from the configurations illustrated in Figure 20(A).

## 2.6 Tribometer Chamber

An ultrahigh vacuum chamber is typically made from stainless steel, has several ports for windows, a manipulator for moving the sample, a cleaning apparatus, instruments, and vacuum pumps. Each port is sealed with a compressed copper gasket, and all electrical feedthroughs are made with ceramics to insulate the electrical conductor from the metal chamber while keeping air out of the chamber. The gaskets, wire insulators, and metals used must have a vapor pressure that is negligible and in the ultrahigh vacuum range. The chamber is baked at about 150 degrees Celsius for several days to remove volatile contaminants from the walls before experiments are

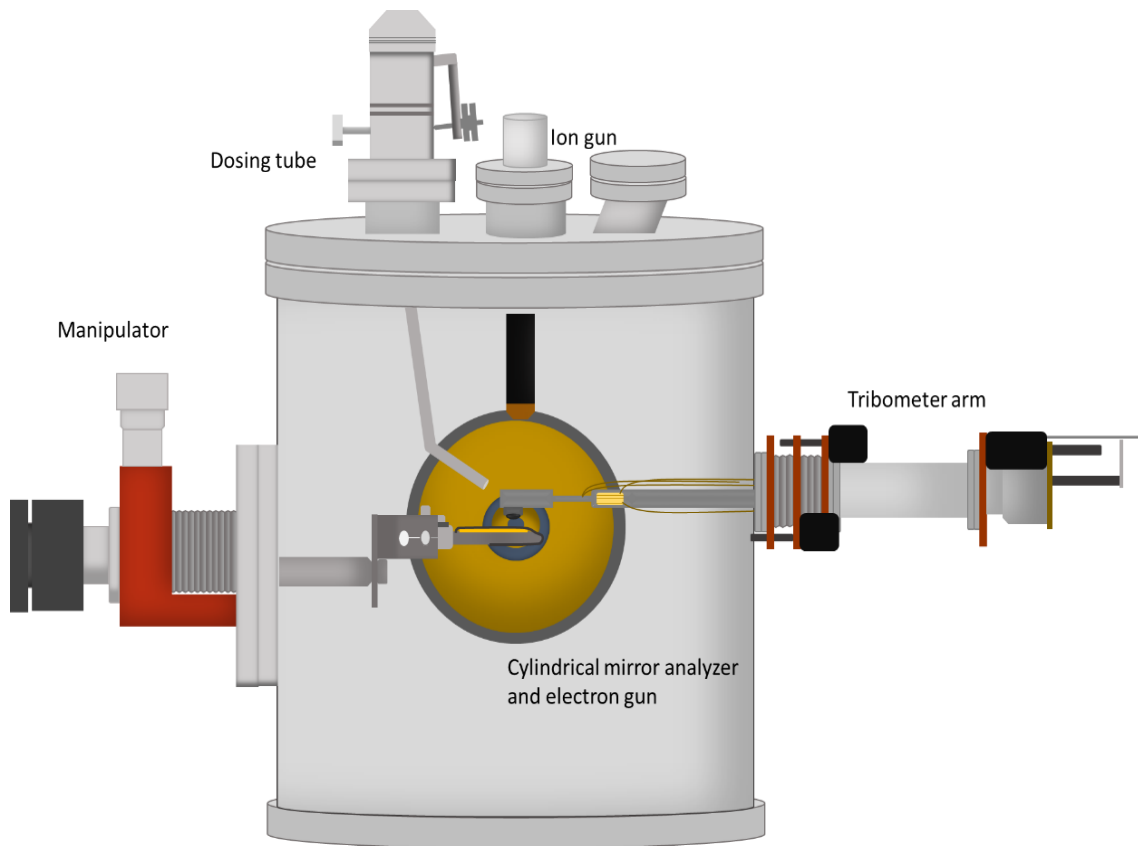


*Figure 2-21 Cutaway, side-view of the tribometer chamber*

done. This is accomplished with resistive heating wires, variacs, and the chamber is insulated using aluminum foil. Diagrams of the chamber are shown in Figures 21 and 22.

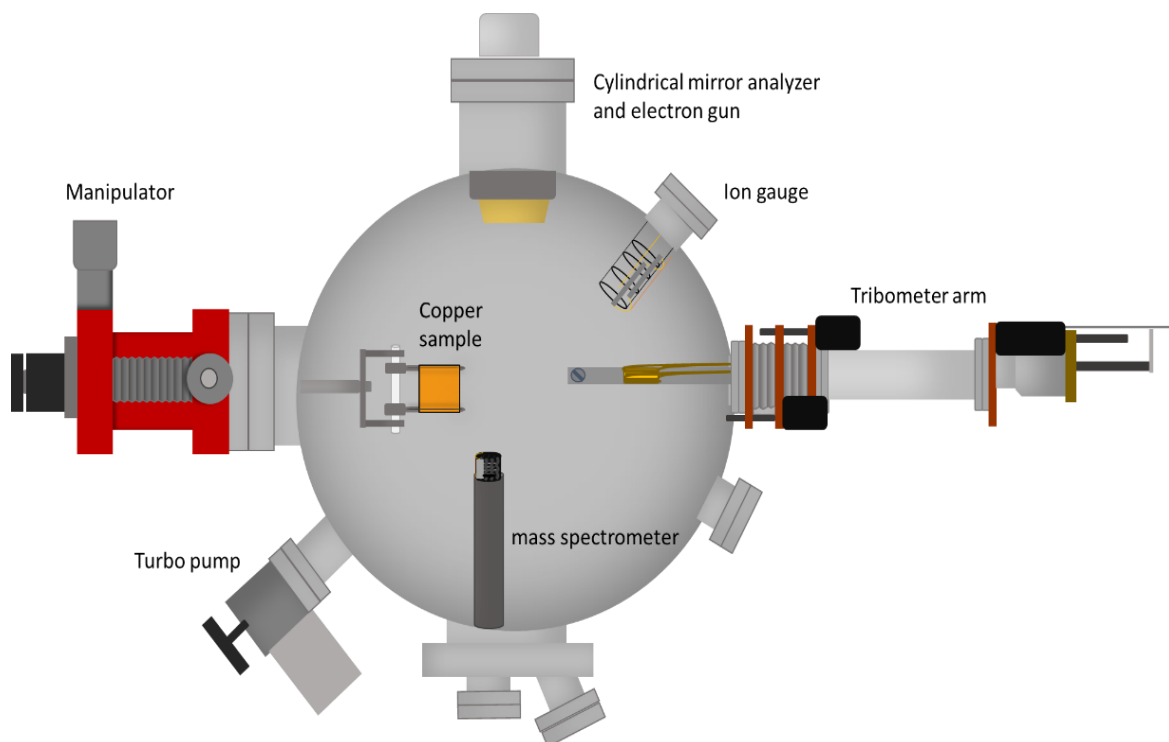


*Figure 2-22 Cut-away top view of tribometer chamber.*

### **Monolayer dosing experiments**

In the case of these experiments, experiments were carried out using adsorbed monolayers on the copper substrate. The tribometer arm was positioned above the clean copper sample and the pin was rubbed across the sample for approximately 50 scans to create an initial “wear scar” that results in a constant contact area and friction coefficient

The clean adsorbate was dosed via a leak valve connected to a dosing tube mounted above the sample to minimize the background pressure in the chamber while dosing. The tribometer arm was then lowered again and the sample was rubbed at the desired load and velocity, and the friction

coefficient and gas-phase products due to adsorbate decomposition induced by sliding by a mass spectrometer placed close to, and in line-of-site of the contact between the ball and the sample were measured. Both reciprocating and unidirectional sliding paths were used.

Once the friction experiments were finished, the tribometer arm was retracted and the rubbed region was analyzed by Auger spectroscopy using a small-spot-size electron gun to ensure that only the rubbed region was investigated.

### **Continuous-dosing experiments**

Other experiments were performed in which the sample was rubbed while the chamber was pressurized with a reactant. The sample preparation for these continuous-dosing experiments was the same as the monolayer dosing experiments. The wear scar was created by reciprocating rubbing of sample for about 50 passes and then the chamber was pressurized with the gas-phase reactant. The surface was rubbed while dosing under various loads, and friction coefficient was measured. The tribometer arm was then retracted and Auger spectra were collected from the rubbed surface.

## ***2.7 Conclusion***

This chapter contains a brief description of the techniques and instruments used to collect data for this dissertation. The limitations and advantages of the equipment used is necessary to understand the experiments in chapters 4 through 7 of this dissertation.

## 2.8 References

1. O'Hanlon, J. F. *A user's guide to vacuum technology / John F. O'Hanlon.* (1989).
2. Beck, A. H. W. (Arnold H. W. *Handbook of vacuum physics. / Edited by A. H. Beck.* (Pergamon Press; [distributed in the Western Hemisphere by Macmillan, New York], 1964).
3. Carpenter, L. G. *Vacuum technology; an introduction / by L.G. Carpenter.* (1970).
4. Robinson, N. *The Physical Principles of Ultra-High Vacuum Systems and Equipment.* (Chapman and Hall, 1968).
5. Welch. *Duoseal 1397 Rotary Vane Pump User Manual. 8606,*
6. Varian. *Varian V70 Turbo pump manual.* (Varian Vacuum Technology, 2006).
7. Duniway. *Ion Pump manual.* (Duniway, 1996). doi:10.1016/S0022-3913(12)00047-9

# Chapter 4

## Theoretical Methods

### *3.1 Introduction*

Developing models for predicting chemical bonding has been an important, and considering scientific history, relatively recent, advancement in chemistry, allowing for breakthroughs in fields from interpreting STM data to tailoring semi-conductor properties<sup>1-4</sup>. Advancements in the understanding of the nature of electrons, combined with an increase in computing power, have allowed efficient, accurate predictions of chemical structure and energetics to be made by predicting whether a given set of atoms is most likely to form molecules or remain atomic.

The most probable distribution of a set of electrons in space, or electron density distribution, can be found by exploiting the wave-like nature of the electron using the principles of quantum mechanics. The nuclear positions, by contrast, can be treated semi-classically,

ignoring their wave-like behavior because of their significantly larger mass by using the Born-Oppenheimer approximation. The motion of the atomic cores follows the forces defined by the electron density distribution. An understanding of the way computer programs determine the electron density and energy of a system and use that information to search for the lowest-energy atomic configuration is crucial to being able to adequately model chemical interactions.

This Chapter is meant to serve as an analog to the experimental methods Chapter 2, for calculations. Density functional theory, DFT, is a powerful tool for predicting and identifying surface structures and reactions, but as with any resource, it has limitations. The following Chapter is meant to serve as a basic explanation of the resources used in this dissertation for calculations, not as a thorough description of the principles of DFT.

First, the general principles of a single-electron system are explained briefly to introduce concepts that are necessary to use a reasonable implementation of DFT. Then the necessity of using DFT and the basic decisions that affect accuracy for the electronic states are explained in the following sections. Finally, some simple discussions of the issues that can arise from movement of the ions are given.

### ***3.2 Single-electron model***

The description of the properties of multi-electrons systems starts with the behavior of a single electron. The observable properties of an electron at a given position in space: kinetic and potential energies, and momentum, can be described mathematically using a wave function as a function of position,  $\Psi(x, y, z)$ . The wave function can be used in two ways. First, multiplying the wavefunction by its complex conjugate gives the probability that the electron will be found at a given position with coordinates  $x, y, z$  within an infinitely small volume,  $dx dy dz$ .

$$p(x, y, z)dx dy dz = \Psi(x, y, z)\Psi^*(x, y, z)dx dy dz \quad (1)$$

Second, an operator may be applied to the wave function to obtain an observable quantity. The observable may be position, energy, momentum, kinetic energy, or the angular momentum in the z-direction. The operator that provides the energy observable is called the Hamiltonian operator and can be used in the Schrödinger equation, where H is the Hamiltonian operator, E is an eigenvalue equal to the total energy, and  $\Psi(x, y, z)$  is the eigenfunction, or wavefunction.

$$H\Psi(x, y, z) = E\Psi(x, y, z) \quad (2)$$

The wavefunction must meet several conditions: it must be smooth and continuous, and the square of the wave function must integrate over all space to one, that is, the probability of finding the electron somewhere in space is unity. All observables must be real, so that quantum mechanical operators are Hermitian.

In most cases, the exact wavefunction of an electron is not known, and so an approximate wavefunction must be identified to predict probability distributions. First, a set of basis functions are used to develop an approximate wavefunction. The variational principle uses the Schrödinger equation to find the linear combination of these basis functions that give the lowest energy, or ground state of the electron. The variational principle states that the lowest energy possible for a system with an approximate wavefunction is greater than or equal to the energy given by using the true ground-state wavefunction,  $E_0$ .

$$\iiint_{-\infty}^{\infty} \Psi(x, y, z)H\Psi(x, y, z) dx dy dz \geq E_0 \quad (3)$$

Taking the derivative of the energy found in equation 2 with respect to the trial parameters of the wavefunction and setting the result equal to zero yields the energy minimum with the parameters

used to describe the trial wavefunction and the resulting parameters provide the best approximation of the trial wavefunction to the true, ground-state wavefunction of the system.

Building the system up from a single to a multi-electron model is not trivial due to electron-electron interactions and the Fermionic anti-symmetric conditions on the wavefunction. The Hamiltonian depends on the potential energy of the electron interaction with the nuclei, the potential energy contribution from interactions between electrons, and the kinetic energy. Electrons and nucleus are charged particles and change velocity in response to changes in potential energy, which is a function of position, this will be important later in the chapter when potential energy terms are discussed. To simplify the potential energy terms, nuclei are considered fixed in space in accord with the Born-Oppenheimer approximation, discussed above. Even with this approximation, as electrons are added to the system, the potential contribution of each electron-electron interaction becomes more complicated to calculate, reaching a situation in which there is no analytical solution to the Schrödinger equation even for a system with three electrons. This is a serious problem for making chemical predictions on interesting systems using the wavefunctions of electrons.

To treat multiple electrons, John Slater developed the Slater determinant, which constructs a multi-electron wavefunction by using a linear combination of the orbitals where the electrons are indistinguishable and anti-symmetric to one another as required for Fermions. This means that the probability of finding the same electron in two different orbitals is zero, so that the probability of finding more than one electron with the same spin in the same orbital is also zero. Using a Slater determinant as the trial function results in the Hartree-Fock equation, that yields an explicit exchange term arising from the antisymmetric nature of the wavefunction. This topic will be covered in more detail in the Potentials section.

### ***3.3 Density Functional Theory***

Rather than treating the wavefunctions of individual electrons, Thomas<sup>5</sup> and Fermi<sup>6</sup> developed a model of metals using discrete volumes of constant electron density by assuming that the local distribution of electrons could be approximated by the equations that describe a uniform electron gas. This treats the energy directly as a function of average electron density. The drastic approximations to both the kinetic energy and electron-electron interaction make the Thomas-Fermi model underestimate bonding and is not useful to describe chemical systems.

This concept was improved upon by Hohenberg-Kohn,<sup>7</sup> later improved by Kohn and Sham<sup>8</sup>, which states that a unique functional that fully describes the energy of the ground state electron density distribution will have the lowest energy, and any approximation to that distribution will be higher. Hohenberg, Kohn and Sham further showed that the energies of the system were uniquely determined by the electron density distribution. The energies are given by functionals, i.e. functions that depend on another function, of the electron distribution. Accordingly, gives the density functionals,  $F[\xi]$ , based on the density distribution of the electrons without having to treat the electrons individually, under the influence of an external potential energy component, generally defined by the nuclei positions, given by  $V_{ext}[\xi]$ , electron-electron potential energy term,  $V_{ee}[\xi]$ , kinetic energy term,  $T_s[\xi]$ , and contributions from exchange and correlation energies,  $E_{xc}[\xi]$ . Kohn-Sham described these functionals in terms of an auxiliary set of orbitals,  $\phi$ , that are used to describe the density distribution.

$$F[\xi] = T_s[\xi] + V_{ee}[\xi] + V_{ext}[\xi] + E_{xc}[\xi] \quad (4)$$

$$T_s = \sum \langle \phi_i | -\frac{1}{2} \nabla^2 | \phi_i \rangle \quad (5)$$

$$\xi = \sum |\phi_i|^2 \quad (6)$$

The basic approach has been described above, but the exact nature of the functionals,  $T_s[\xi]$  and  $V[\xi]$  used to determine the energy from the density distribution need to be determined.

### 3.4 Potentials

As mentioned previously, to avoid solving for the wave function as a function of the position of each electron, the Hartree-Fock model treats the kinetic and potential energies of the system as orbitals so that terms,  $T_s[\xi]$ ,  $V_{\text{ext}}[\xi]$  and  $V_{\text{ee}}[\xi]$  (the mean field Hartree-Coulomb interaction among electrons) correspond to the kinetic and potential energies predicted by the non-interacting system of electrons, then added the exchange and correlation energy ( $E_{\text{xc}}[\xi]$ ) to account for the difference in kinetic and potential energies between the non-interacting auxiliary model system and interacting systems in which there are several interactions that must be counted. Building the functional is accomplished by adding the external field (that of the nuclei), the kinetic energy, and the contribution from the interaction on the kinetic and potential terms, which is called the exchange-correlation energy, or  $E_{\text{xc}}$ .

$$F[\xi] = T_s[\xi] + V_{\text{EE}}[\xi] + V_{\text{ext}}[\xi] + E_{\text{xc}}[\xi] \quad (7)$$

The form of  $E_{\text{xc}}$  is not known exactly, since that would correspond to exactly solving the many-body problem, and must be approximated in some way, since it is crucial to being able to solve density functional problems. The local density approximation (LDA) assumes that the exchange-correlation energy can be approximated by a uniform electron gas. This is done by weighting the exchange-correlation energy at a position,  $r$ , with the density probability at  $r$ . The

exchange correlation energy can be split into exchange term,  $\epsilon_x$  for an electron in a uniform electron gas, called the Slater exchange, and a correlation term,  $\epsilon_c$ .

$$E_{xc}^{LDA} = \int \xi(r) \epsilon_{xc} \xi(r) d(r) \quad (8)$$

$$\epsilon_{xc} = \epsilon_x(\xi(r)) + \epsilon_c(\xi(r)) \quad (9)$$

Systems in which the electron density drops off or increases rapidly in space, i.e. most systems, do not closely resemble this approximation. It is somewhat effective, however in predicting some real systems because (i) in the case of high densities, these Coulomb interactions are dominant, and (ii) in the low-density region the contribution to the energies are small. In addition, the LDA satisfies a number of important sum rules. It has been shown to be entirely ineffective in many metallic systems where non-local effects on the exchange energy must be taken into account.<sup>9,10,11</sup>

The gradient-corrected approximation (GGA) modifies the LDA by using the gradient of the electron density distribution, thereby introducing a non-homogeneous element. The gradient contribution to  $E_{xc}$  are not directly known, and many methods for including a gradient term can and have been used. GGA functionals can be tailored to work for specific problems, i.e., situations in which hydrogen bonding is important, metallic systems, or large or small molecules. VASP includes access to several potentials for calculations. The potential used in this work is the GGA potential developed by Perdew, Burke, and Ernzerhof and is called the PBE functional.<sup>12</sup>

### ***3.5 Projector-Augmented plane-wave approximations***

The systems described in this dissertation are methyl thiolate adsorbed on a Cu (100) surface under the influence of various perturbations. Many programs are available to calculate the

energy of chemical states, and have been shown to be useful for predicting experimental results.<sup>13-</sup>

<sup>15</sup> The work done in this dissertation has used one such program, VASP, the Vienna Ab-Initio Simulation Package, which is a projector-augmented plane-wave package. The single particle orbitals are described by a set of plane-waves, and near the atoms, within the muffin-tin radii, by an atomic-like wavefunction. The wavefunction can be described as a periodic and using Bloch's theorem, a solution for the extended lattice can be found using only one cell where the states are labeled by a quasi-momentum vector,  $\vec{k}$ . Thus, a metal with a near-infinite supply of conduction-band electrons can be approximated more accurately than they would be if limited to a collection of only a hundred or two atoms. The atoms are treated as ions, with core electrons having a fixed density distribution, as they are not involved in bonding or the electron conduction. The number of planewaves used to determine the wavefunction in practice have a cut-off for high kinetic-energy states.

The effective number of momentum vectors is determined by the number of points sampled to adequately describe the electron density distribution over the Brillouin zone. The points for these calculations are obtained by the Monkhorst-Pack scheme, which distributes the given number of points over the Brillouin zone. The so-called gamma point, of the Brillouin zone, is chosen as the center of the mesh and is included as a point that is sampled. The points are generated to avoid sampling multiple symmetrically equivalent points. In practice, calculations using several k-point schemes are used until the energies are consistent for several sets of k-point.

### 3.6 Ionic Minimization

For a given set of energy cut-offs and k-point samplings, the variational principle is used to optimize the electron density distribution for a fixed set of atomic positions (the Born-Oppenheimer approximation.) It is not computationally feasible to sample every possible position of an array of ions to manually compare the energy of each configuration to find likely positions. A method of finding the lowest energy for the ionic positions is necessary for modeling realistic systems because the initial structural guesses are not usually the best choice. Even so, VASP is only capable of determining configurations of ions with no energy barrier from the initial guess. Figure 1 shows a schematic of a potential energy surface of one ion, in gray, in a multi-atomic system.

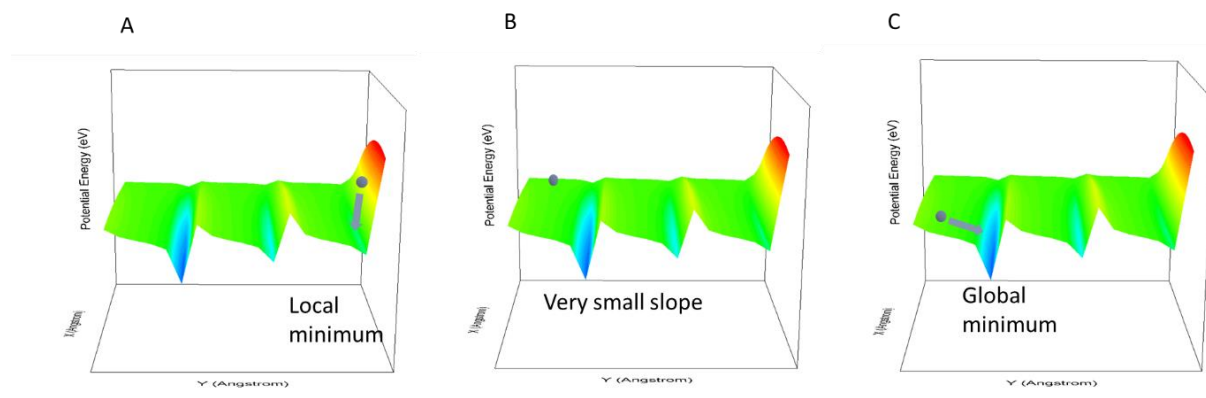


**Figure 4-1 Searching for the global minimum of energy for an ion (in gray) on a potential energy surface. A) and B) give false minimums due to the proximity of a local minimum and a small slope, respectively. C) shows an ion that could move along lines of force to the global minimum**

The VASP software finds the optimum structure is accomplished by generating trial steps of the atomic position based on the forces calculated from the Hellman-Feynman theorem. In this work, two ways of finding the local minimum-energy configurations were used. Both use the local force acting on the atom obtained from the derivative of the potential energy with respect to position, called the Hessian, and an appropriate force factor to calculate how to move the ions

toward the local minimum. The minimization is done in steps because it allows all ions to move simultaneously in the calculation, and so must be done in an iterative fashion to map out new regions of the potential energy surface during each step.

For an initial search, a conjugate gradient method was used. This method uses forces to define a direction for atomic position that minimizes the energy, and estimates the local minimum based on the energy and its first and second derivatives. For a conjugate gradient search, a trial step is taken, the energy is recalculated, and a corrector step is made to adjust the direction of movement. Once the movement is in the direction towards the estimated minimum, the cycle begins with another trial step. Figure 2 illustrates the path of an ion following the conjugate gradient method of minimization. This is a time-consuming process, but is important if the system is not close to a minimum energy configuration to establish the optimum direction of motion without over-shooting the minimum position when large forces are present.

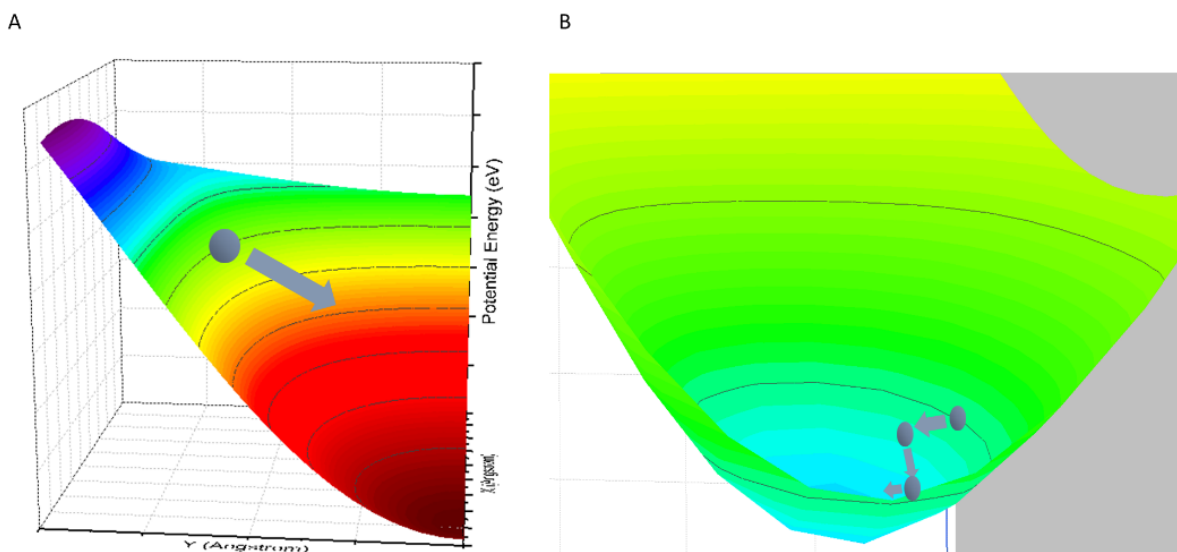


**Figure 3-2** The ion movement determined by conjugate gradient method. A) shows the path of the ion at an angle to that of steepest descent. B) shows several steps along the path near the minimum.

Once the atomic position approaches the minimum energy configuration, the relaxation process can be set to a quasi-Newtonian method, which uses information from the previous step, and this is usually the faster convergence method as the force on the atoms becomes low. This method sometimes causes the force to accelerate the atomic position to overshoot the minimum energy configuration, and so that the quasi-Newtonian method should only be used near a minimum. Figure 3 illustrates the method of quasi-Newtonian relaxation. Once the total force reaches a value equal to or less than the convergence criterion, then the relaxation is considered complete.

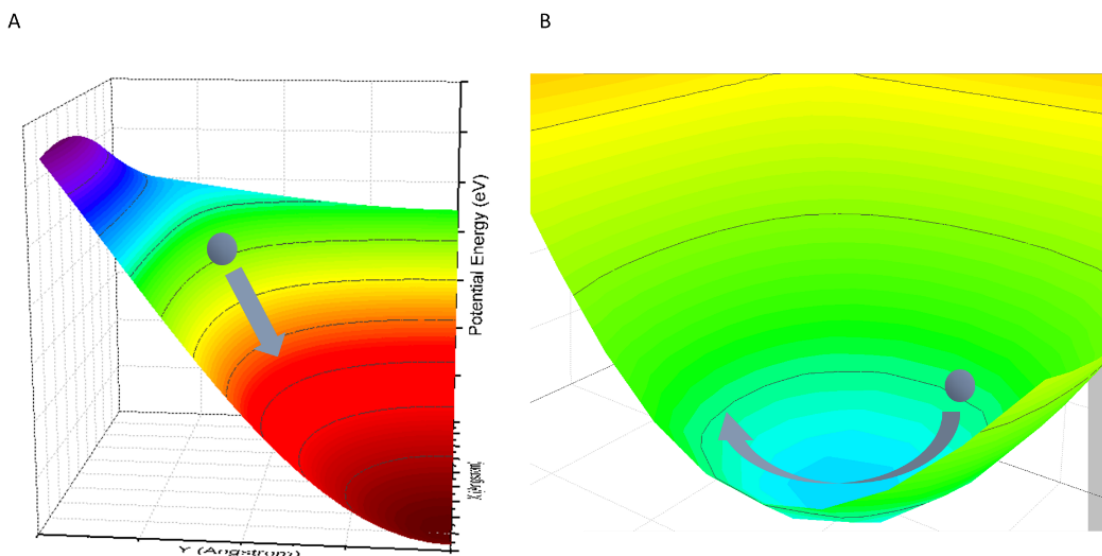


**Figure 3-4** Movement determined by the quasi-Newtonian force method. *A)* shows the ion moving along the path of steepest descent of a potential energy surface. *B)* shows the path of an ion accelerated using a time-step that moves the ion too far through the minimum.

### **3.7 Minimum Energy Pathway for a reaction**

Frequently, information is required about the path a chemical state reaction toward a reactant through a transition state to a reaction product. The reaction pathway and energy of the transition state can be compared with experimentally measured activation energies.

However, an issue with calculating reaction energy pathways is that the transition state structure is not at an energy minimum because it, by definition, is at a saddle point in the plot of energy versus reaction coordinate. This precludes the variational principle from being used to calculate the structure and energy of the transition state.

To solve this problem, the energies of the reaction pathway and at the transition state must be calculated subject to some set of constraints that prevent the structure from relaxing to the minimum energy (either reactant or product) structures.

This is accomplished in this work by the chain-of-states method. Converged structures for the initial and final states of the reaction are found. The intermediate steps in the reaction pathway from the reactant to the product structures are described by a series of images, or atomic positions along a trial reaction pathway. In the so-called nudged-elastic-band, NEB, a pseudo-force or spring force connects the images, allowing the energy of each image to be minimized in the direction tangential to the reaction pathway, while preventing the images from moving independently and keeping them evenly spaced along the path. Figure 4 A shows an illustration of a pathway across a potential energy surface.

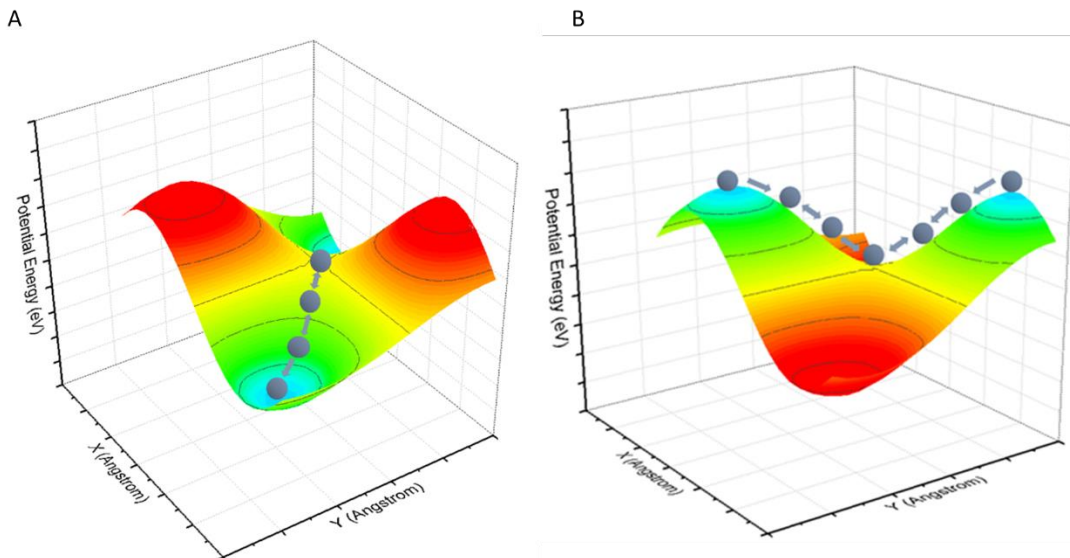


**Figure 3-4** A) NEB method for finding the MEP. The ionic positions are constrained by a spring force between them, represented by gray arrows, along the direction of the reaction path that keeps the steps equally spaced. The path goes through the saddle point, but it is not necessarily likely to find an image located directly at the transition state. B) cut-away image of cNEB method. The same potential energy surface is used as in figure 4, but the forces are inverted along the potential energy path.

In contrast to NEB calculations, the climbing nudged-elastic-band, cNEB, (illustrated in 4 B) ensures that the saddle-point configuration is found, rather than points on either side of it, by inverting the forces along the band to ensure that there is a “false” local minimum at the transition state. The images relax toward this minimum and yield the transition state structure.

These methods require a converged product, which, if incorrect, can skew the minimum energy pathway (MEP) by pulling the images of the chain out of this pathway with the spring forces lining up toward a false minimum.

This Chapter has briefly described the fundamental steps to computationally model chemical systems using DFT. The models obtained using DFT with reasonable convergence criteria, appropriate starting positions, accurate potentials and precise sampling positions provide high degrees of accuracy in predicting a variety of physical phenomena.<sup>16</sup>

### ***3.8 Conclusion***

DFT does a reasonably good job in predicting chemical systems if the correct decisions are made in implementing the method. Converge reactant and product configuration must be found for cNEB calculations to be able to find the true minimum-energy pathway, and to avoid spring forces dragging the path through a false minimum. Appropriate force constants and structural convergence criteria must be set based on the potential energy surface and the size of the system balance with the time to complete the calculation versus the required precision of energy and position. The initial structural guesses must be those that result in a force that directs the structure toward the global minimum, which can never be known and depend on judgements of whether the final structure is chemically and physically reasonable. Multiple initial configurations for systems are generally checked to ensure a correctly converge structure. The software uses the variational principle to refine the electronic energies and charge densities until the convergence criteria is met. K-points and convergence criteria must be checked by doing multiple calculations and finding the point where there is no change in energy with change in k-points and convergence criteria.

This Chapter is, as stated in the introduction, not a history of quantum mechanics or a full exposition of the subject, but should be treated as a field guide for performing DFT calculations. There are many excellent resources for those looking for a more in-depth understanding of the principles of quantum mechanics.<sup>17-20 21</sup>

### 3.9 References

1. Garvey, M., Weinert, M. & Tysoe, W. T. On the Pressure Dependence of Shear Strengths in Sliding, Boundary-Layer Friction. *Tribol. Lett.* **44**, 67 (2011).
2. Kestell, J. *et al.* Structural Changes in Self-Catalyzed Adsorption of Carbon Monoxide on 1,4-Phenylene Diisocyanide Modified Au(111). *J. Phys. Chem. C* **119**, 18317–18325 (2015).
3. Li, Y. Y., Chen, M. X., Weinert, M. & Li, L. Direct experimental determination of onset of electron–electron interactions in gap opening of zigzag graphene nanoribbons. **5**, 4311 (2014).
4. Mahapatra, M. & Tysoe, W. T. three-point bonding. *Phys. Chem. Chem. Phys.* **17**, 5450–5458 (2015).
5. Thomas, L. H. The calculation of atomic fields. *Math. Proc. Cambridge Philos. Soc.* **23**, 542–548 (1927).
6. Fermi, E. A statistical method for determining some properties of the atom. *Rend. Accad. Lincei* **6**, 602–7 (1927).
7. Hohenberg, P. & Kohn, W. Inhomogeneous Electron Gas. *Phys. Rev.* **136**, B864–B871 (1964).
8. Kohn, W. & Sham, L. J. Self-consistent equations including exchange and correlation effects. *Phys. Rev.* **140**, (1965).
9. Lazzeri, M., Attaccalite, C., Wirtz, L. & Mauri, F. Impact of the electron–electron correlation on phonon dispersion: Failure of LDA and GGA DFT functionals in graphene and graphite. *Phys. Rev. B* **78**, 81406 (2008).
10. Cohen, A. J., Mori-Sánchez, P. & Yang, W. Insights into Current Limitations of Density Functional Theory. *Science (80-. )*. **321**, 792 LP-794 (2008).
11. YAKOVKIN, I. N. & DOWBEN, P. A. THE PROBLEM OF THE BAND GAP IN LDA CALCULATIONS. *Surf. Rev. Lett.* **14**, 481–487 (2007).
12. Perdew, J. P., Burke, K. & Ernzerhof, M. Generalized Gradient Approximation Made Simple. *Phys. Rev. Lett.* **77**, 3865–3868 (1996).
13. Sholl, D. S. & Steckel, J. A. in *Density Functional Theory* 35–48 (John Wiley & Sons, Inc., 2009). doi:10.1002/9780470447710.ch2
14. Li, X., Gellman, A. J. & Sholl, D. S. Orientation of ethoxy, mono-, di-, and tri-fluoroethoxy on Cu(111): a DFT study. *J. Mol. Catal. A Chem.* **228**, 77–82 (2005).
15. Bradley, M. K., Woodruff, D. P. & Robinson, J. Adsorbate-induced surface stress, surface strain and surface reconstruction: S on Cu(100) and Ni(100). *Surf. Sci.* **613**, 21–27 (2013).

16. Adams, H. L. *et al.* Shear-Induced Mechanochemistry: Pushing Molecules Around. *J. Phys. Chem. C* **119**, 7115–7123 (2015).
17. Harrison, N. M. An Introduction to Density Functional Theory. *Technology* **2**, 1–26 (1995).
18. Gibson, M. C. Implementation and application of advanced density functionals. (Durham University, 2006). at [http://etheses.dur.ac.uk/2938/1/2938\\_769.pdf](http://etheses.dur.ac.uk/2938/1/2938_769.pdf)
19. Sholl, D. S. & Steckel, J. A. in *Density Functional Theory* 83–112 (John Wiley & Sons, Inc., 2009). doi:10.1002/9780470447710.ch4
20. Wang, G.-C., Li, J., Xu, X.-F., Li, R.-F. & Nakamura, J. The relationship between adsorption energies of methyl on metals and the metallic electronic properties: A first-principles DFT study. *J. Comput. Chem.* **26**, 871–878 (2005).
21. Koch, W. & Holthausen, M. C. *Wolfram Koch, Max C. Holthausen A Chemist's Guide to Density Functional Theory. Neural Networks* **3**, (2001).

# Chapter 4

## Mechanical Activation of Decomposition of Methyl Thiolate on Copper Foil

### *4.1 Introduction*

Chemical reaction rates can be accelerated by supplying energy thermally, photochemically, by an external electrical potential, or mechanically, the mechanisms by which the latter operates being the least well-understood.<sup>1</sup> Despite this lack of understanding, over the past decades, a large number of mechanochemical syntheses have been discovered.<sup>2-6</sup> Most fundamental insights into how mechanical energy can accelerate a chemical reaction comes from single-molecule force spectroscopy experiments<sup>7-9</sup> that take advantage of the exquisite sensitivity of the atomic force microscope and this approach also enables the direction of the force to be controlled with respect to the surface-mediated molecular orientation. The results of such single-molecule pulling experiments have been analyzed theoretically using density functional theory (DFT), where, for example, it has been found that pulling alkyl thiolates from gold<sup>10</sup> or copper<sup>11</sup> causes gold atoms to be plucked out of the surface along with the alkyl thiolate group.

While such experiments and theoretical analyses provide an understanding of the effect of tensional forces, the majority of technologically important mechanochemical reactions are induced by interfacial shear, for example by ball milling or in a sliding contact, where a lubricant additive reacts with a surface to form a film that reduces friction and/or wear. Mechanochemical removal of adsorbed layers by shear has been observed in the atomic force microscope<sup>12-13</sup> but the resulting small scan area precludes meaningful surface analyses of the rubbed region from being carried out. DFT analyses have also been used to examine the effect of lateral force on adsorbed layers. For example, it has been shown that shear forces on alkyl thiolates on gold cause lateral motion both of thiolate-gold entities and the surface gold layer<sup>10</sup> in accord with the restructuring of gold surfaces covered by sulfur-containing molecules during scanning.<sup>14</sup>

Analyzing the chemical processes occurring at such sliding solid-solid interfaces, in particular measuring reaction rates, is the most challenging of surface chemistry problems since *in situ* spectroscopies, certainly surface-sensitive techniques based on electrons, are impossible, so that buried interfaces can be interrogated only using optical spectroscopies when one of the counter faces is transparent.<sup>15</sup> Although X-ray diffraction has recently been used to monitor mechanochemical reactions *in situ*,<sup>16</sup> the technique is not surface sensitive. Adding to these experimental problems is the fact that frictional heating can lead to uncertainties in the reaction temperature<sup>17</sup> and may result in an interface in which the energy distribution is no longer described by a Boltzmann probability.<sup>18</sup>

These experimental challenges are addressed by using a model mechanochemical system consisting of a ball sliding on a methyl thiolate- ( $\text{CH}_3\text{-S-}$ ) covered copper surface in ultrahigh vacuum (UHV) and by measuring mechanochemical reaction kinetics from the gas-phase products formed during sliding. Crucially, calculations of frictional heating for this experiment reveal a

temperature rise much less than 1 K; the interfacial temperature is well defined and has a Boltzmann energy distribution. The experiments are supplemented by DFT calculations of the reaction energy profiles and molecular dynamics (MD) simulations of the sliding interface to analyze the force distribution on the methyl thiolates during sliding.

## ***4.2 Experimental***

Experiments were carried out in a stainless-steel, UHV chamber operating at a base pressure of  $\sim 2 \times 10^{-10}$  Torr following bake out, which has been described in detail elsewhere.<sup>19-20</sup> The chamber was equipped with a UHV-compatible tribometer in which a pin can be slid against a flat substrate, which simultaneously measures the normal load and lateral force by means of strain gauges. The contact resistance between the pin and substrate can be monitored. Measurements were made using speeds of 1 or  $4 \times 10^{-3}$  m/s at a normal load of 0.44 N. The spherical pin ( $\sim 1.27 \times 10^{-2}$  m diameter) was made from tungsten carbide containing some cobalt binder and could be heated by electron bombardment *in vacuo* to clean it. Adsorbed methyl thiolate species were prepared by dosing dimethyl disulfide (DMDS) through a high-precision leak valve connected to a dosing tube (with an internal diameter of  $4 \times 10^{-3}$  m) directed towards the sample so that the pressure at the sample was enhanced compared to the measured background pressure, which was set at  $2 \times 10^{-8}$  Torr during DMDS dosing (where pressures are not corrected for ionization gauge sensitivity). Experiments were performed by initially rubbing the pin against the clean copper sample ( $\sim 1 \times 1$  cm<sup>2</sup> by  $\sim 1$  mm thick) 50 times until a constant friction coefficient was obtained.

The chamber also contained a single-pass, cylindrical-mirror analyzer (CMA) for Auger analysis, and an argon ion bombardment source for sample cleaning and depth profiling. Auger

spectra were collected using an electron beam energy of 5 keV. A high spatial resolution electron gun and a channeltron secondary electron detector were also incorporated into the system. This allowed scanning electron microscopy (SEM) images of the wear scar to be collected. Finally, the chamber also included a quadrupole mass spectrometer (UTI model 100C) placed in line of sight of and  $\sim 10$  cm away from the sliding contact. The filament of the mass spectrometer was extensively outgassed prior to any experiments being carried out to minimize the background pressure. The mass spectrometer was interfaced using a LabView program, which controlled the detected mass and monitored the mass spectrometer signal as a function of time. The mass spectrometer was also used for leak checking and for gauging reactant purity. An experiment was carried out by initially saturating the copper foil with DMDS after completion of the initial run-in period on the clean copper sample. The pin then approached the surface until reaching a preset load and was then moved across the surface at a preset sliding speed while simultaneously monitoring the normal load ( $F_N$ ), lateral force ( $F_L$ ), and mass spectrometer signal. The normal load remained constant during the scan and the friction coefficient was calculated from  $\mu = \frac{F_L}{F_N}$ .

The copper samples (Alfa Aesar, 99.99% pure, 1 mm thick) were polished to a mirror finish using 1  $\mu\text{m}$  diamond paste and then rinsed with deionized water and cleaned ultrasonically in acetone. Once in UHV, the copper sample was further cleaned using a procedure that consisted of Argon ion bombardment ( $\sim 1$  kV,  $\sim 2$   $\mu\text{A}/\text{cm}^2$ ) and annealing cycles up to  $\sim 850$  K. The cleanliness of the samples was monitored using Auger spectroscopy and it was found to exhibit rectangular low-energy electron diffraction (LEED) patterns after cleaning and annealing in UHV, indicating that the surface contained well-ordered Cu (100) regions.<sup>21</sup>

The DMDS (Aldrich, 99.0% purity) was transferred to a glass bottle and attached to the gas-handling system of the vacuum chamber, where it was subjected to several freeze-pump-thaw cycles. The purity of the DMDS was monitored using mass spectroscopy.

### 4.3 Theoretical Methods

Density functional theory (DFT) calculations were performed with the projector augmented wave method<sup>22-23</sup> as implemented in the Vienna *ab initio* simulation package, VASP.<sup>24-26</sup> The exchange-correlation potential was described using the generalized gradient approximation of Perdew, Burke and Ernzerhof.<sup>27</sup> A cutoff of 400 eV was used for the planewave basis set, and the wavefunctions and electron density were converged to within  $1 \times 10^{-6}$  eV. The first Brillouin zone was sampled with a  $7 \times 7 \times 1$  Monkhorst-Pack grid.<sup>28</sup> Geometric relaxations were converged when the force was less than 0.01 eV/Å on all unrestricted atoms. Activation energies were calculated using the climbing image nudged elastic band method. The initial and final states (first and last points on Figure 1) were first calculated with DFT and a linear interpolation of the atomic positions was used to determine the initial positions of the starting nudged elastic band (NEB) images.<sup>29-30</sup>

Molecular dynamics (MD) simulations were performed on a system consisting of methyl thiolate species ( $\text{CH}_3\text{-S-}$ ) adsorbed onto two copper, Cu (100) plates. The system was periodic in the plane of the  $4 \times 4 \text{ nm}^2$  surfaces of the face-centered-cubic copper plates. The initial simulation structure was constructed using Accelrys Materials Studio<sup>©</sup>, and subsequent simulations performed using Large Atomic/Molecular Massively Parallel Simulation (LAMMPS) software.<sup>31</sup> The Polymer Consistent Force Field (PCFF) with a global cutoff of 1.0 nm was used to describe bond, angle, torsion, and out-of-plane interactions between all atoms. A Noé-Hoover thermostat

<sup>32-33</sup> maintained the model temperature at 300 K and simulations were run with a time step of 0.005 fs.

An initialization process was used to create methyl thiolate-covered surfaces. First, the system was equilibrated with weak non-bonded interactions between the Cu and the S atoms from the methyl thiolate molecules. The simulation was equilibrated for 10 ps, the time required for the system to reach a stable potential energy, during which the CH<sub>3</sub>-S- groups moved freely between the two copper plates. Then, the strength of the non-bonded interactions between Cu and S was artificially increased such that the S atoms migrated towards the Cu plates. After the adsorbed system reached a stable potential energy, the positions of the adsorbed S atoms on the plates were fixed and the Cu-S interactions reduced to their initial values.

Production simulations consisted of applying load and then shear. First, a pressure of 450 MPa was applied to the top copper plate and the system was allowed to equilibrate for 0.35 ns, the time necessary for the force between S atoms and methyl (CH<sub>3</sub>-) groups to achieve a Gaussian distribution with zero mean force in the lateral directions. The top plate was then translated laterally with a sliding speed of 4 mm/s. The force in the sliding direction on each S-C bond was calculated at each time step. Details on the bond force calculation are available in Section 5 of the Supporting Information. The top plate slid laterally a total of 2 nm, and the distributions of bond forces were averaged over the last 1 nm of sliding. An animation of the simulation is shown in Movie S1.

## ***4.4 Results***

Experiments were performed on a copper surface saturated with methyl thiolate species that are grafted onto an atomically clean copper foil in UHV by exposure to dimethyl disulfide

(CH<sub>3</sub>-S-S-CH<sub>3</sub>, DMDS) at room temperature. It has been shown that DMDS initially reacts by rapidly cleaving the S-S bond to form adsorbed methyl thiolate (CH<sub>3</sub>-S<sub>(ads)</sub>) species that decompose thermally to evolve predominantly methane (along with some ethylene and ethane) displaying a peak centered at ~425 K in temperature-programmed desorption (TPD).<sup>21</sup> Here the additional hydrogen required to form methane from methyl thiolate species is provided by formation of C<sub>2</sub> hydrocarbons.<sup>21</sup> Thus, for a room-temperature experiment, the temperature rise required to cause methyl thiolate decomposition (~125 K) is much larger than that caused by frictional heating; any reaction products detected during sliding must be formed mechanically. A reaction activation energy for methane formation is estimated from the TPD peak temperature by assuming a typical pre-exponential factor of  $1 \times 10^{13} \text{ s}^{-1}$ <sup>34</sup> to be ~100 kJ/mol,<sup>21</sup> giving a thermal reaction rate constant of  $\sim 4 \pm 1 \times 10^{-5} \text{ s}^{-1}$  at 290 K.

Control experiments were performed to ensure that the methane formed during rubbing evolved from the sliding contact and was not due to desorption from other moving parts of the vacuum chamber. In the first experiment, a thiolate-saturated copper sample was heated to 450 K to thermally decompose the thiolate species. The relatively short heating time of ~30 s ensured that only the sample and no other parts of the apparatus were heated. No methane was detected after this procedure while rubbing, indicating that the methane detected for the methyl thiolate-covered surface is due to adsorbed methyl thiolate decomposition. Second, a thiolate saturated sample was rubbed in both directions (towards and away from the mass spectrometer). The resulting plot of 16 amu (methane) signal as a function of the number of passes, with a normal load on 0.44 N and a sliding speed of  $4 \times 10^{-3} \text{ m/s}$  is displayed in Figure 1(A). This no longer shows the exponential decrease in pulse height as a function of the number of scans, but relatively larger signals when the pin slides away from the mass spectrometer than towards it.

This confirms that the methane evolves from the sliding contact rather than being due to outgassing of other moving parts of the vacuum chamber since the latter would not depend on the sliding direction. This indicates that the gas-phase products are trapped in the interface and released as the pin moves past, giving a directionality to the release of hydrocarbons. Similar trapping of shear-induced reaction products has been found in MD simulations. An expanded methane desorption pulse is shown in Figure 1(B), which indicates that methane is only detected while rubbing.

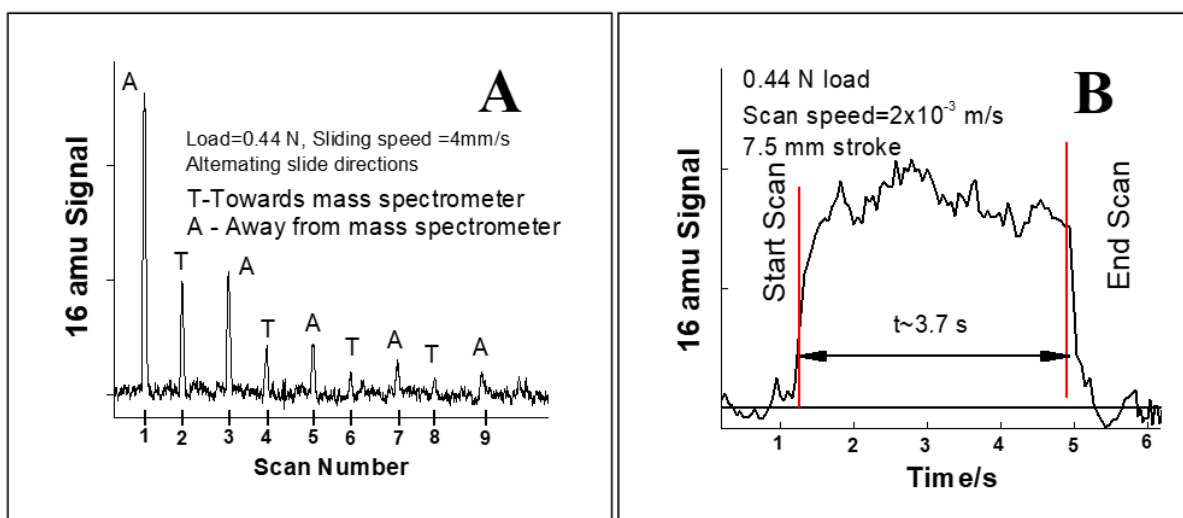


**Figure 4-1 (A)** Plot of the 16 amu (methane) signal measured during reciprocating sliding on a thiolate-saturated copper foil as a function of the number of scans at a sliding speed of  $4 \times 10^{-3}$  m/s with a normal load of 0.44 N. The methane signals measured while the pin is moving towards the sample are labeled T and those measured with the pin moving away from the sample are labeled A. **(B)** Expanded profile of a methane desorption pulse measured at a sliding speed of  $2 \times 10^{-3}$  m/s with a normal load of 0.44 N.

DFT calculations are used to explore the lowest-energy decomposition pathway for methyl thiolate species on copper using the NEB method on a Cu(100) substrate, since this surface structure was detected by low-energy electron diffraction (LEED) for a copper foil that had been cleaned and annealed in UHV.<sup>21</sup> The slab is composed of  $2 \times 2 \times 4$  copper atoms, with the lowest layers two layers of the slab frozen and a methyl thiol in a hollow on the top copper layer in a  $p2 \times 2$

cell, under a significant vacuum gap. This configuration corresponds to half coverage. The resulting energy profile is shown in Figure 2, yielding a reaction activation energy for C–S bond scission of  $\sim 106$  kJ/mol, in excellent agreement with the value for methane formation estimated from the TPD experiment. Experiments on the thermal chemistry of DMDS on copper foils<sup>21</sup> showed that methane formation at  $\sim 425$  K was accompanied by methyl thiolate decomposition as evidenced by the shift of the S  $2p$  X-ray photoelectron peak due to the formation of adsorbed sulfur. A small feature at  $\sim 2827$   $\text{cm}^{-1}$  in the infrared spectrum of the surface observed while heating a methyl thiolate-covered surface was assigned either to the presence of methyl groups on the surface or an overtone. XPS indicated that thiolate decomposition to form adsorbed sulfur occurred over the same temperature range at which methane was detected, consistent with thiolate decomposition being the rate-limiting step in the reaction. If the subsequent reactions of the methyl species formed by C–S bond scission were rate limiting, the activation energy for methane formation would be larger than that calculated by DFT; the agreement between the calculated activation barrier for methyl thiolate decomposition and the measured activation energy for methane formation provide evidence that the rate-limiting step is methyl thiolate decomposition to  $\text{CH}_3(\text{ads})$  and  $\text{S}(\text{ads})$ . The detection of methane at room temperature during sliding (see below) indicates that, for our system, the subsequent reaction steps after C–S bond cleavage are fast.

Figure 2 also shows how the structure of adsorbed methyl thiolate evolves during the reaction, revealing that the methyl group moves laterally relative to the copper surface, which provides a reference plane, in going from the initial ( $\text{CH}_3\text{--S}(\text{ads})$ ) state to the transition state. This motion is collinear with the friction force, which is parallel to the surface thus providing an ideal system for understanding mechanochemical mechanisms at a sliding interface. The key to accomplishing this is the ability to measure mechanochemical reaction rates which is achieved by

monitoring the gas-phase products formed during sliding of a tungsten carbide ball containing a copper transfer film formed during a run-in period, against a methyl thiolate-covered copper sample. In this case, the shear forces are exerted directly on the methyl thiolate species in an analogous manner to that found for fluid shear.<sup>35</sup>

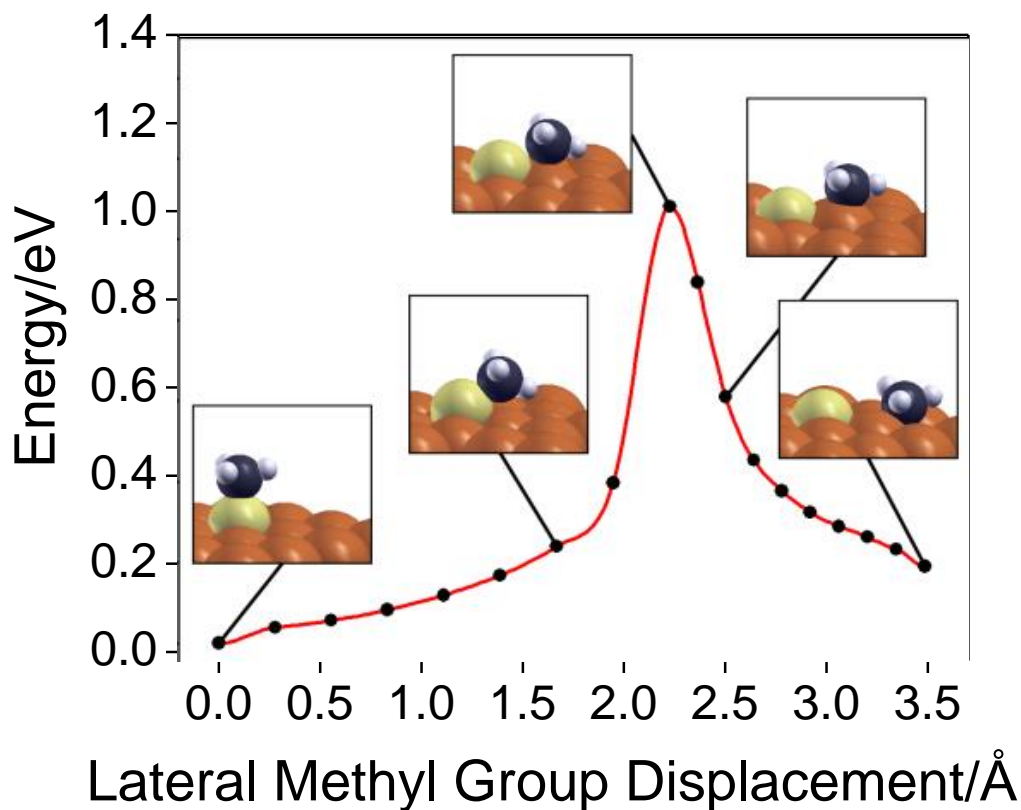


**Figure 4-2** The profile of energy versus the lateral displacement of the methyl group in methyl thiolate, for the decomposition of methyl thiolate species on a Cu (100) surface obtained using density functional theory calculations. The calculated activation energy ( $\sim 1.1$  eV,  $\sim 106$  kJ/mol) is in good agreement with the experimental value measured by temperature-programmed desorption.<sup>21</sup> Shown also in the figure is the evolution in the structure of the thiolate species as it forms adsorbed methyl species.

The experiment is carried out in UHV at a sliding speed of  $4 \times 10^{-3}$  m/s under a normal load of 0.44 N by monitoring the gas-phase 16 amu (methane) signal using a quadrupole mass spectrometer placed close to and in-line-of-sight of the contact between the ball and sample. A

wear track is first created on the clean copper sample, resulting in a stable friction coefficient  $\mu = F_L/F_N = 0.52 \pm 0.06$ , where  $F_L$  is the lateral force and  $F_N$  the normal load, causing the transfer of copper to the tribopin. The surface is exposed to DMDS at room temperature to saturate it with methyl thiolate species and the sample is then rubbed in one direction, away from the mass spectrometer, on the previously rubbed region, while simultaneously monitoring any desorbing species, where the friction coefficient decreased to  $0.28 \pm 0.06$ . The resulting plot of the 16-amu (methane) signal as a function of the number of sliding passes is displayed in Figure 3A.

Measuring the signals at other masses confirms that methane is formed, as in the thermal reaction, and control experiments established that the methane evolved from the sliding contact. The results of scanning until the methane evolution has decreased to zero (after  $\sim 8$  passes) and then re-exposing the surface to DMDS to again saturate the previously rubbed region with methyl thiolate species are shown as an inset to Figure 3A. This plots the desorption yields calculated from the integrated areas under the desorption pulses for each scan *versus* the number of scans. The results are identical within experimental error, which is  $\sim 10\%$  of the signal, for each experiment, indicating that the mechanochemical reaction reforms a clean surface, in accord with previous elemental analyses of the rubbed region using Auger spectroscopy where it was shown that adsorbed sulfur is transported into the subsurface region.<sup>19</sup> The results indicate that several passes over the initially thiolate-saturated surface are required to completely remove all methyl thiolate species, thereby allowing the rate constant for the mechanically induced decomposition of the methyl thiolate species to be measured.

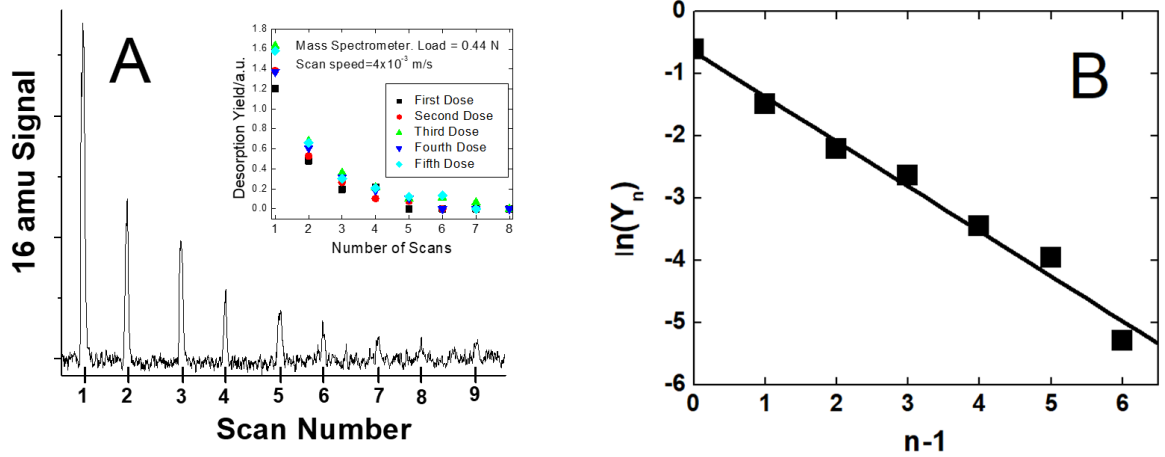


**Figure 4-3 (A)** The 16 amu (methane) signal measured by sliding a tungsten carbide pin containing a copper transfer film on a pre-rubbed (50 scans) clean copper foil as a function of the number of scans at a sliding speed of  $1 \times 10^{-3}$  m/s with a normal load of 0.44 N showing the decay in methane desorption yield as a function of the number of scans. Shown as an inset is the desorption yield measured from the area under each methane pulse as a function of the number of scans. After collecting data for the first DMDS dose while sliding at  $4 \times 10^{-3}$  m/s, until no more methane was detected (■), the sample was re-saturated with DMDS and the 16 amu signal again monitored (●). This experiment was repeated for the third (▲), fourth (▼) and fifth (◆) DMDS doses, where the evolution of methane yield as a function of the number of scans is identical within experimental error. **(B)** Plot of the desorption yield measured from the integrated area under each desorption pulse for the  $n^{\text{th}}$  pass  $Y_n$  for the desorption of methane during sliding, taken from the data in Figure 2A, plotted versus  $(n-1)$ .

For a first-order reaction with a shear force  $F$ ,  $k(F)$ , the rate of change of surface coverage  $\theta$  due to mechanochemical desorption is:

$$-\frac{d\theta}{dt} = k(F)\theta \quad (1)$$

Defining the coverage at the inlet of the contact as  $\theta_i$ , and the coverage at the outlet as  $\theta_o$  as the contact slides over a portion of an adsorbate-covered wear track, the decrease in coverage  $\Delta\theta = \theta_i - \theta_o$  is given by:

$$\theta_o = \theta_i \exp(-k(F)) \quad (2)$$

so that  $\Delta\theta = \theta_l(1 - \exp(-k(F)))$ . The decrease in thiolate coverage results in gas-phase methane formation so that the methane yield  $Y$ , measured from the integrated area under the methane desorption pulse, is proportional to  $\Delta\theta$  so that  $Y = A\theta_l(1 - \exp(-k(F)))$ , where  $A$  is a normalization constant. The inlet thiolate coverage for the first pass  $\theta_l(1) = 1$  so that the methane desorption yield during the first pass is  $Y_1 = A(1 - \exp(-k(F)))$ . The inlet coverage for the second pass,  $\theta_l(2)$  equals the outlet coverage for the first pass;  $\theta_l(2) = \exp(-k(F))$ . Thus, the desorption yield in the second pass is given by:  $Y_2 = A\exp(-k(F))(1 - \exp(-k(F)))$ . Repeating this process shows that the yield for the  $n^{\text{th}}$  pass, defined as the total amount of methane produced in each pass, is given by:

$$Y_n = A(1 - \exp(-k(F)))\exp(-(n-1)k(F)) \quad (3)$$

The sum over all yields should be the initial coverage (unity). Putting  $\alpha = \exp(-k(F))$  gives  $Y_n = A(1 - \alpha)\alpha^{(n-1)}$ . The total yield  $Y_{tot}$  is obtained by summing over all values of  $n$ :

$$Y_{tot} = A(1 - \alpha)\sum_{n=1}^{\infty} \alpha^{(n-1)} \quad (4)$$

Since  $\alpha$  is less than unity, the series converges giving  $Y_{tot} = A = 1$  leading to an equation for  $Y_n$ :

$$Y_n = (1 - \alpha)\alpha^{(n-1)} \quad (5)$$

and yields an equation that depends on  $k(F)$  for a first-order reaction with respect to number of passes.

The experiments were all carried out at the same speed and a time dependence is not known. If a time dependence is assumed, the contact time would be a constant in each pass. Assuming there is a time dependence, eq. 3 can then be measured from the integrated areas under

each desorption pulse,  $Y_n$  for the  $n^{\text{th}}$  pass, modeled as a first-order, time dependent reaction is given by:

$$Y_n = (1 - \exp(-k(F)t_C))(\exp(-k(F)t_C))^{(n-1)} \quad (6)$$

where  $k(F)$  is the rate constant under the influence of a lateral force  $F$ , and  $t_C$  is the time required for the pin to traverse the contact. The data in Figure 2A are replotted as  $\ln(Y_n)$  versus  $(n-1)$  (Figure 2B), which is linear, thus confirming the validity of equation (3), yielding a value of  $k(F)$  or  $k(F)t_C = 0.78 \pm 0.02$  pass<sup>-1</sup> or s<sup>-1</sup>, respectively.

To determine the time dependent rate, if any, the nature of the contact must be known. Assuming that the surface deforms elastically with a conformal contact between the ball and groove after completion of the formation of the initial wear track gives a contact length of  $37 \pm 2$   $\mu\text{m}$ , an average contact pressure  $P_C = 120 \pm 6$  MPa,<sup>36</sup> so that  $k(F) = 21 \pm 1$  s<sup>-1</sup> with  $t_C = 36 \pm 2$  ms at a sliding speed of  $1 \times 10^{-3}$  m/s. This rate constant yields an activation energy of  $65.0 \pm 0.5$  kJ/mol using the standard value of the pre-exponential factor at a temperature of 290 K. Assuming that the elastic contact arises from a groove radius that is slightly larger than that of the ball (see Supporting Information, Section 3.2) yields an average contact pressure  $P_C = 95 \pm 5$  MPa and an average contact length of  $\sim 40$   $\mu\text{m}$ , giving that  $k(F) = 19.5 \pm 1$  s<sup>-1</sup>, changing the activation energy negligibly to  $65.0 \pm 0.5$  kJ/mol. Finally, assuming that the surface deforms plastically results in a shorter contact length ( $\sim 10$   $\mu\text{m}$ ). Using this value to estimate  $t_C$  yields  $k(F) = 78 \pm 2$  s<sup>-1</sup>. However, this change again only has a relatively modest effect on the mechanochemical activation energy, which is reduced to  $61.8 \pm 0.2$  kJ/mol. The values for the different contact model are summarized in Table 1.

Note that the differences in shear-induced rate constants depending on the nature of the assumed contact are much smaller than the change caused by interfacial sliding from the thermal

rate constant at this temperature ( $4 \pm 1 \times 10^{-5} \text{ s}^{-1}$ ). The availability of an experimental value of the shear-induced rate constant,  $k(F)$  allows the mechanism by which a shear force accelerates a chemical reaction to be explored in detail.

## 4.5 Discussion

It is clear that the rate of methyl thiolate decomposition is significantly accelerated at the sliding interface. The mechanism by which this works will need thorough study to be explained. It is unlikely that low coordination sites are the cause for the decomposition due to the extremely low decomposition temperature of methyl thiolate on a more open or strained surface<sup>1,2</sup> relatively given high, measurable decomposition rate during rubbing. The sulfur-carbon bond is not being broken immediately on dosing a full monolayer, but is instead decomposing slowly while rubbing. The exponential decay of the signal with scan number indicates a probabilistic function is an appropriate starting point for analysis.

Assuming a time-dependent model, the external work carried out during sliding directly lowers the energy barrier and the most commonly used model for describing mechanochemical reaction rates, the Bell model<sup>35, 38-39</sup> proposes that the reaction activation energy,  $E_{act}$  decreases by an amount equal to the external work performed on the system,  $\vec{F} \cdot \Delta\vec{x}$ , where  $\Delta\vec{x}$  is a vector aligned along the reaction coordinate from the initial state towards the transition state under the influence of an external mechanical force  $\vec{F}$ . Bell pointed out that the activation energy becomes zero if  $|\Delta\vec{x}|$  equals the distance from the reactant to the transition state  $|\Delta\vec{x}^\ddagger|$ ,<sup>38</sup> yielding a simple formula for the rate constant  $k(F)$ :

$$k(F) = k_0 \exp\left(\frac{\vec{F} \cdot \Delta\vec{x}^\ddagger}{k_B T}\right) \quad (7)$$

where  $k_B$  is the Boltzmann constant,  $k_0 = A \exp\left(-\frac{E_{act}}{k_B T}\right)$ , the thermal rate constant at a temperature  $T$ , and  $A$  the reaction pre-exponential factor. Analogous ideas have been used to model atomic-scale wear during sliding<sup>40-41</sup> and to model viscosity.<sup>35</sup> Modifications of this equation have been proposed,<sup>9, 39, 42-43</sup> but the simple EB model has been found to work reasonably well at low stresses,<sup>44</sup> although it has been suggested that  $|\Delta x^\ddagger|$  should be considered to be a variable that is fit to the data. However, the model assumes that the shape of the energy profile is not influenced by the imposition of an external force although this simple model is particularly useful since the shape of the energy profile is often not known. However, in this work, the thermal reaction profile is available from DFT calculations (Fig. 2). This allows a more complete analysis to be performed to gauge the effect of a shear force  $F$  on the reaction profile. This is achieved by superimposing an external potential,  $V_e(x) = -Fx$  due to the imposed force  $F$  on the reaction energy profile  $V_r(x)$  (Fig. 2). This yields a total energy profile as a function of the external force,  $V(F) = V_r(x) - Fx$ . The variation in the height of the activation barrier of the combined potential is calculated numerically as a function of  $F$  and the results are shown in Fig.4 (■) and demonstrate that the energy barrier decreases with increasing lateral force, as expected. Shown also plotted on this graph is the prediction of the Bell model using a value of  $|\Delta x^\ddagger| = 0.22$  nm taken from Fig. 2. This model correctly predicts the decrease in energy barrier only for very low forces, but deviates quite substantially from the values obtained from the full profile (■) at higher forces. This effect arises since the curvature of the energy profile for the initial state is much smaller than that for the transition state (Fig. 2). This causes the position of the minimum in energy for the initial state to move to higher  $x$  values more rapidly than the position of the transition state under the influence of the external potential  $V(x) = -Fx$ .

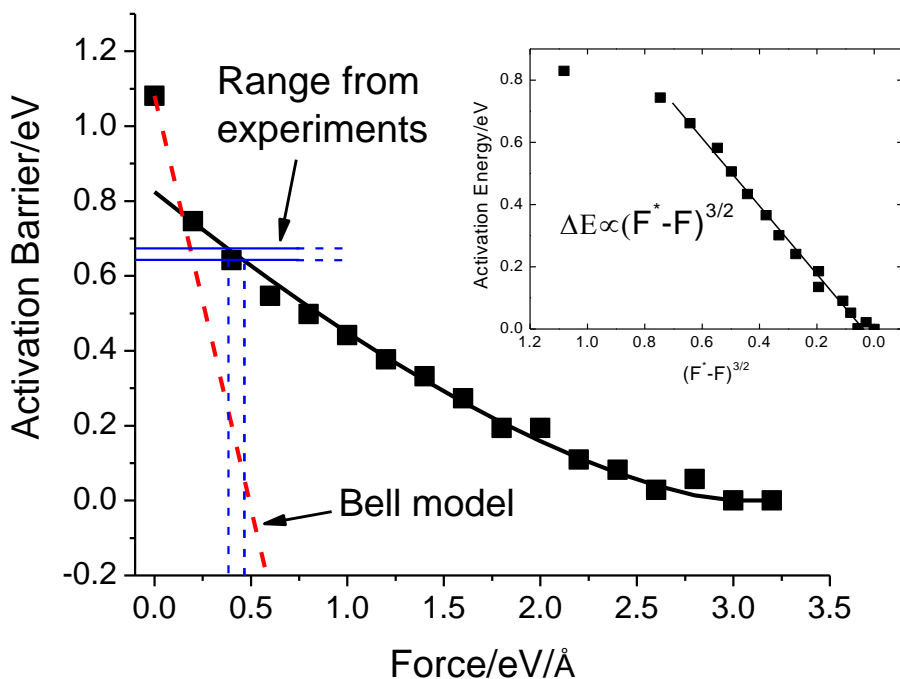


**Figure 4-4** Plot of the calculated energy barrier as a function of the shear force obtained from the calculated energy profile for the decomposition of thiolate species (Fig. 2) by superimposing a potential due to the external force,  $V(x)=-Fx$ . This is compared with the prediction of the conventional Bell model, drawn as a red line. Indicated also as thick lines is the discrete force (of  $\sim 0.5$  eV/Å) that would be required to lower the activation barrier to the experimentally measured values of between 64 and 58 kJ/mol). An inset shows a plot of the height of the activation barrier as a function of  $[(F^*-F)]^{3/2}$ , where  $F^*$  is the value of the force at which the energy barrier decreases to zero.

Prandtl carried out the earliest work on the effect of an external force on lowering the barrier of an activated process<sup>45</sup> and showed that the energy barrier should decrease to zero at some critical force  $F^*$  and vary as a function of energy as the force approaches this value as  $E_a(F) \propto (F^* - F)^{3/2}$ . This theory, generally known as the Tomlinson/Prandtl model, has been successfully used to describe the temperature and velocity dependences of nanoscale friction measured using an atomic force microscope (AFM).<sup>46-51</sup> The calculated energy barrier is therefore plotted *versus*  $(F^* - F)^{3/2}$  and the result is shown as an inset in Figure 4. This reproduces the variation in energy barrier with shear force over a reasonable range of forces using a value of  $F^* \sim 2.85$  eV/Å ( $\sim 1.78$

nN). Shown also plotted onto this figure are the values of shear force that would be required to lower the activation barrier to the experimentally measured values (~62 to 65 kJ/mol), suggesting that this would require a force  $F \sim 0.5 \text{ eV/\AA}$  (~0.3 nN/molecule).

The value of  $F$  can be obtained from the shear strength  $S$  (sliding force per unit area) from  $\mu = S/P_C$  where  $\mu$  is the friction coefficient ( $0.28 \pm 0.06$ ) and  $P_C$  the contact pressure (Table 1). Thiolate species on Cu(100) saturate in a  $c(2 \times 2)$  over layer corresponding to a theoretical saturation coverage of 0.5 ML (monolayers, where coverages in this case are normalized to the copper atom density on the Cu(100) face).<sup>52-54</sup> However, since the thiolates form due to dissociative adsorption of dimethyl disulfide, which will require the presence of two adjacent adsorption sites, the true saturation coverage will not attain this value, so that a more realistic saturation coverage of 0.45 ML is used to take this into account. This yields a value of the average lateral force  $F$  from ~0.015 to 0.018 nN/molecule for elastic contacts and a value of  $F = 0.07 \pm 0.01$  nN/molecule for a plastic contact and the values are summarized in Table 1. These values are much lower, by an order of magnitude or more, than that required to yield the measured shear-induced activation barrier (~0.3 nN/molecule, Fig. 4).

However, the multiplicity of molecular contacts at the sliding interface can result in a distribution of lateral forces as found previously in MD simulations of organic molecules on surfaces.<sup>55-56</sup> Accordingly, MD simulations were carried out with a contact pressure of 450 MPa, corresponding to the measured hardness of the cleaned and annealed copper foil,<sup>57</sup> at a sliding speed of  $4 \times 10^{-3}$  m/s to characterize the force distribution on a methyl thiolate over layer on copper. The results reveal that there is a broad, Gaussian distribution in forces acting on the carbon-sulfur bonds as shown in Figure 5, where the average calculated shear force per molecule  $F_\theta$  is ~0.08 nN, in reasonable agreement with the experimental values above. Note that this distribution of bond

forces is symmetric, consistent with the harmonic form of the bond term in the empirical potential; this is different from the asymmetry expected from the contact force distribution.<sup>56</sup>

The Polymer Consistent Force Field (PCFF) with a global cutoff of 1.0 nm was used to describe bond, angle, torsion, and out-of-plane interactions between all atoms. Bond interactions are described by  $E = K_2(r - r_0)^2 + K_3(r - r_0)^3 + K_4(r - r_0)^4$  where  $E$  is energy,  $r$  is distance, and  $r_0$ ,  $K_2$ ,  $K_3$ , and  $K_4$  are coefficients. PCFF is not a reactive potential, so that the bonds cannot break. Instead the form of the equation is harmonic such that the force is zero when the bonds are at their equilibrium lengths and then increases rapidly when the bonds are stretched or compressed. The interactions between two contact surface atoms are captured by the Lennard-Jones potential,  $E = 4\varepsilon \left[ \left(\frac{\sigma}{r}\right)^{12} - \left(\frac{\sigma}{r}\right)^6 \right]$  where  $E$  is energy,  $r$  is distance,  $\varepsilon$  is the depth of the potential well and  $\sigma$  is the distance at which potential is zero.

## 5.2 Shear Force per Molecule

The shear force per molecule is estimated as the x-direction force on the bond between the sulfur and carbon atoms. This value is calculated based on the following equation:

$$d = \sqrt{(x_1 - x_2)^2 + (y_1 - y_2)^2 + (z_1 - z_2)^2}$$

$$f_{x-bond} = f_{total-bond} \left| \frac{(x_2 - x_1)}{d} \right| \quad (8)$$

where  $d$  is distance,  $x$ ,  $y$ ,  $z$  are coordinates of atom 1 (sulfur) and 2 (carbon),  $f_{x-bond}$  is the x-directional bond force, and  $f_{total-bond}$  is the total bond force (per the empirical potential described in the previous section). Since there are many sulfur-carbon bonds in the simulation, there is a distribution of bond forces at any given time. The average shear force per molecule is estimated

as the mean of the  $x$ -direction bond-force distribution. We confirm that the simulation has converged by ensuring that the time-dependent average shear force per molecule is constant.

The contact pressure is calculated from the net normal force acting on the top copper plate divided by the contact area. We also partially validate the simulations by analyzing the distribution of the normal and shear forces on the plates. This is calculated from the non-bonded (Lennard-Jones) force between the carbon atoms on the top plate and the carbon atoms on the bottom plate. Figure 5 shows the contact force distributions in the loading (normal) and sliding (shear) directions. These distributions are obtained from forces output every 0.25ps during a 1 nm simulation. The results are consistent with distribution reported in a previous simulation study.

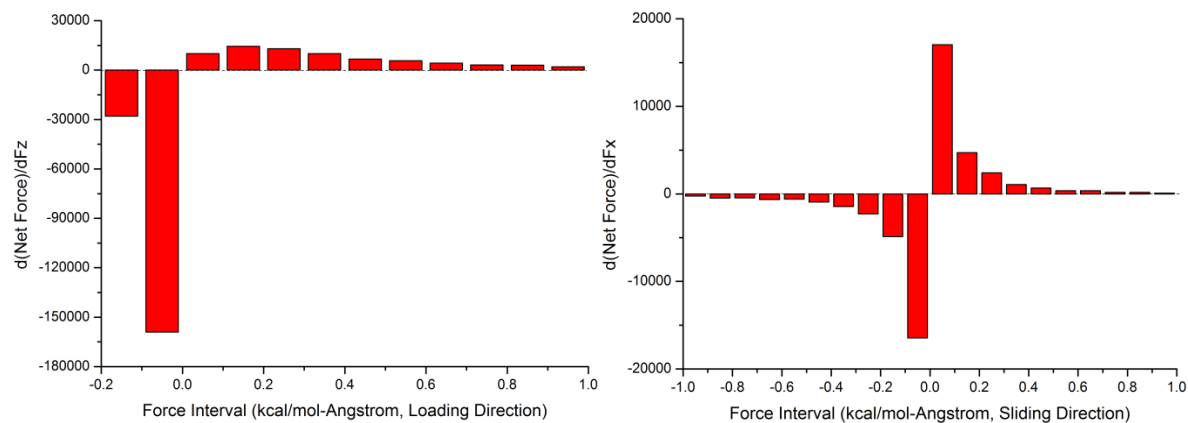


**Figure 4-5 Contact force distributions along the loading (left figure) and sliding (right figure) directions taken at a sliding speed of 40 m/s with a contact pressure of 450 MPa.**

Defining a parameter  $D = \sigma/F_0$ , where  $\sigma$  is the standard deviation of the Gaussian force distribution and  $F_0$  is the average force predicts a value of  $D \sim 7$  from the MD simulations. Since the MD simulations we carried out for a relatively small contact area, such a force distribution is likely to occur not only in the microscale contacts present in the sliding of a pin on a copper substrate studied here but also in the nanocontact of an AFM tip. Similar calculations were carried

at using higher pressures and the results are summarized in Table 2 showing that contact pressure does not appear to strongly influence the value of  $D$ .

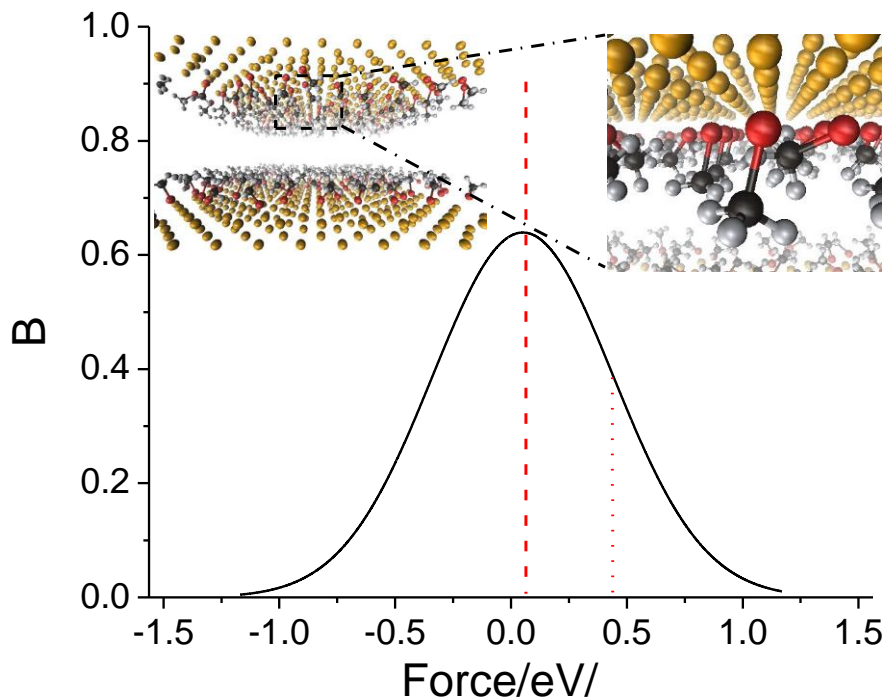


**Figure 4-6** The calculated force distribution from MD simulations of  $\sim 0.45$  monolayers of methyl thiolate species on Cu (100) (where a monolayer is defined as the number of thiolate molecules per copper atom on the (100) surface) at a sliding speed of 4 mm/s with a contact pressure of 450 MPa; snapshots of the simulations are shown in the insets and a movie is shown in the Supporting Information section. The calculated average force  $F_0$  is  $\sim 0.08$  nN (dashed line in figure). However, the distribution of forces is Gaussian with a significant proportion of molecules experiencing much larger forces than the average value. The calculations show that  $D$ , defined as  $\sigma/F_0$ , where  $\sigma$  is the standard deviation of the force distribution (dotted line in figure) is  $\sim 6.9$

Such a force distribution implies that there are much larger forces acting on the methyl thiolate over layer on copper than indicated by the average force and that they are sufficiently high to enable the methyl thiolates to decompose at room temperature. To explore whether the range of values of  $D$  obtained using MD simulations are sufficient to reproduce the experimentally observed activation energies, the effective rate constants  $k(F)$  and the corresponding activation

energies,  $E_a(F)$ , were calculated for a Gaussian distribution of forces using the variation in activation barrier with force shown in Fig. 4.

A Gaussian force distribution  $p(F)$  is found from MD simulations:

$$p(F) = \frac{1}{\sqrt{2\pi}\sigma} \exp\left(-\frac{(F-F_0)^2}{2\sigma^2}\right) \quad (9)$$

where  $F_0$  is the average force and  $\sigma$  is the width of the distribution. Rewriting this using  $D = \sigma/F_0$  gives:

$$p(F) = \frac{1}{\sqrt{2\pi}DF_0} \exp\left(-\frac{(F-F_0)^2}{2D^2F_0^2}\right) \quad (10).$$

The activation energy varies with force as  $\Delta E_a(F)$  as shown in Fig. 3 so that the number of molecules  $\delta n$  that have activation barriers between  $E_a(F)$  and  $E_a(F) + \delta E_a(F)$  is given by:  $\delta n = Np(E_a(F))dE_a(F)$  where  $N$  is the total number of molecules. For a first-order reaction, the reaction rate  $\delta r = Ae^{-\left(\frac{\Delta E_a(F)}{k_B T}\right)}\delta n = Ae^{-\left(\frac{\Delta E_a(F)}{k_B T}\right)}Np(E_a(F))dE_a(F)$ . The total rate of reaction  $R$  is obtained by integrating over all rates:  $R = AN \int_0^\infty e^{-\left(\frac{\Delta E_a(F)}{k_B T}\right)}p(E_a(F))dE_a(F)$ , yielding an effective, shear-induced rate constant  $k(F)$  given by:

$$k(F) = A \int_0^\infty e^{-\left(\frac{\Delta E_a(F)}{k_B T}\right)}p(E_a(F))dE_a(F) \quad (11).$$

This barrier is related to the effective activation energy (measured experimentally) through  $A \exp\left(-\frac{E_a(F)}{k_B T}\right)$ , so that:

$$\exp\left(-\frac{E_a(F)}{k_B T}\right) = \int_0^\infty e^{-\left(\frac{E_a(F)}{k_B T}\right)}p(E_a(F))dE_a(F) \quad (12).$$

The integral is evaluated numerically for both elastic and plastic contacts. The value of the energy distribution  $\Delta E_a(F)$  is evaluated both using the  $(F^* - F)^{3/2}$  dependence alone (inset to Fig. 3) and by using the full variation that includes the initial decrease at low forces calculated from the Bell

model as a function of  $D$ . The results for the elastic contact are displayed in Fig. 5, showing that  $E_a(F)$  decreases with increasing values of  $D$ , as expected.

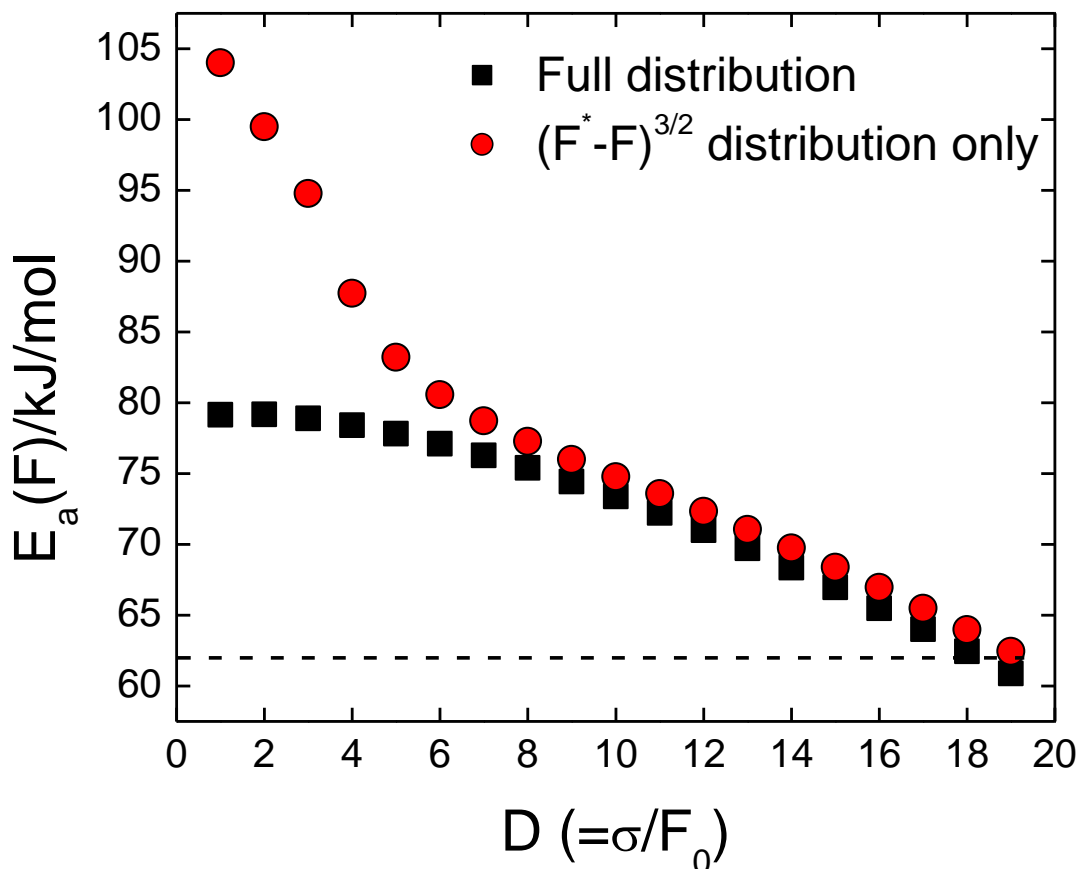


**Figure 4-7** Plot of the influence on the effective activation energy  $E_a(F)$  for a Gaussian force distribution with an average force of  $F_0 \sim 0.018$  nN/molecule with a width at half maximum of  $\sigma$ , where the energy is plotted versus  $D$ , defined as  $D = \sigma/F_0$ . In this case, the value of  $F_0$  was estimated by assuming that the surface deforms elastically. The horizontal line shows the measured value of the shear-induced methyl thiolate decomposition activation energy again assuming elastic deformation of the contact.

There are significant differences between the predictions when only considering the  $(F^* - F)^{3/2}$  force distribution compared with the full distribution, but this difference disappears for larger  $D$  values, as the width of the force distribution becomes larger and so is dominated by higher forces

(Fig. 4). Comparison with the experimental value of activation energy under shear for an elastically deforming interface (Table 1) predicts that a rather large  $D$  value of  $\sim 18$  is required to reproduce the experimental results.

	Contact pressure, $P_C$ /MPa	Track length/ $\mu$ m	Force per molecule/nN	$k(F)/s^{-1}$	$E_a(F)/kJ/mol$
Plastic contact	450	10	$0.07 \pm 0.01$	$78 \pm 2$	$61.8 \pm 0.2$
Elastic contact (identical tip and groove radii)	$120 \pm 6$	37	$0.018 \pm$ $0.003$	$21 \pm 1$	$65.0 \pm 0.5$
Elastic contact (different tip and groove radii)	$95 \pm 4$	40	$0.015 \pm$ $0.003$	$19.5 \pm 1$	$65.0 \pm 0.2$

**Table 4.1** The average contact pressure and track length calculated for various contact models (see Supporting Information, Section 3). Shown also is the average force per molecule, and the calculated shear-induced methyl thiolate decomposition rate constant,  $k(F)$  and well as the corresponding reaction activation energy calculated assuming a standard pre-exponential factor of  $1 \times 10^{13} s^{-1}$

Similar results for the plastically deforming contact are shown in Fig. 6. Now, because of the larger value of  $F_0$  (Table 1), the error in neglecting the initial activation energy decrease (Fig. 3) is less and both curves rapidly converge to similar values. Now the calculation yields a value of  $D \sim 5$ , much closer to the predictions from MD simulations (Table 2). These results indicate that the large forces present in the tail of the broad force distribution exerted on a methyl thiolate over layer at a sliding interface is responsible for the experimentally observed rate of methyl thiolate decomposition.

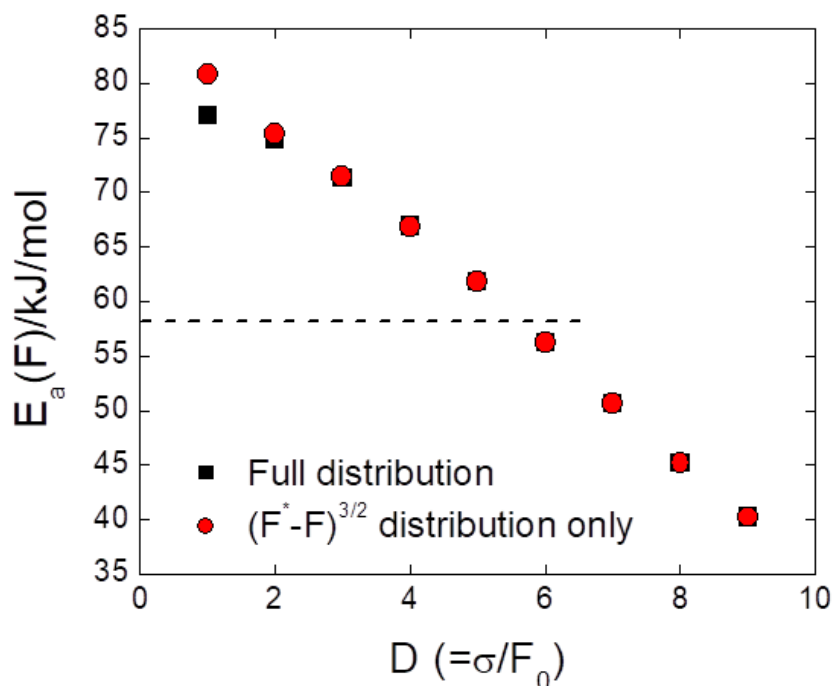


*Figure 4-8 Plot of the influence on the effective activation energy  $E_a(F)$  for a Gaussian force distribution with an average force of  $F_0 \sim 0.07$  nN/molecule with a width at half maximum of  $\sigma$ , where the energy is plotted versus  $D$ , defined as  $D = \sigma/F_0$ . In this case, the value of  $F_0$  was estimated by assuming that the surface deforms plastically. The horizontal line shows the measured value of the shear-induced methyl thiolate decomposition activation energy again assuming plastic deformation of the contact.*

Pressure/GPa	$D$
0.45	7.1
1	7.3
2	7.2
4	7.5

***Table 4-2 Values of  $D$  obtained from the molecular dynamics simulation at different normal pressures at a sliding speed of 40 m/s.***

The larger value of  $D$  for the elastic contact can be traced to the lower value of  $F_0$  and the behavior shown in both Figs. 5 and 6 are dominated by the width of the Gaussian force distribution. For both the plastic and elastic distribution, agreement with the experimentally measured activation energy occurs for  $\sigma \sim 0.14$  nN/molecule. MD simulations predict that  $D$  should be  $\sim 7$  (Table 2) and is consistent with a plastically deforming contact (Fig. 8). Note that the value of  $F_0$  predicted by MD simulations under conditions similar to the ones used in the experiment (0.08 nN) is very close to the value measured assuming a plastically deforming contact ( $0.07 \pm 0.01$  nN). An AFM image of the wear track (Fig. 7) reveals marks along the sliding direction with a root-mean square roughness of  $\sim 5$  nm so that the sliding interface is by no means atomically smooth. Experiments to correlate the nature of the contact with various metals to their plasticity indices<sup>36</sup>,<sup>58</sup> indicate that copper does deform plastically in the contact.<sup>57</sup>

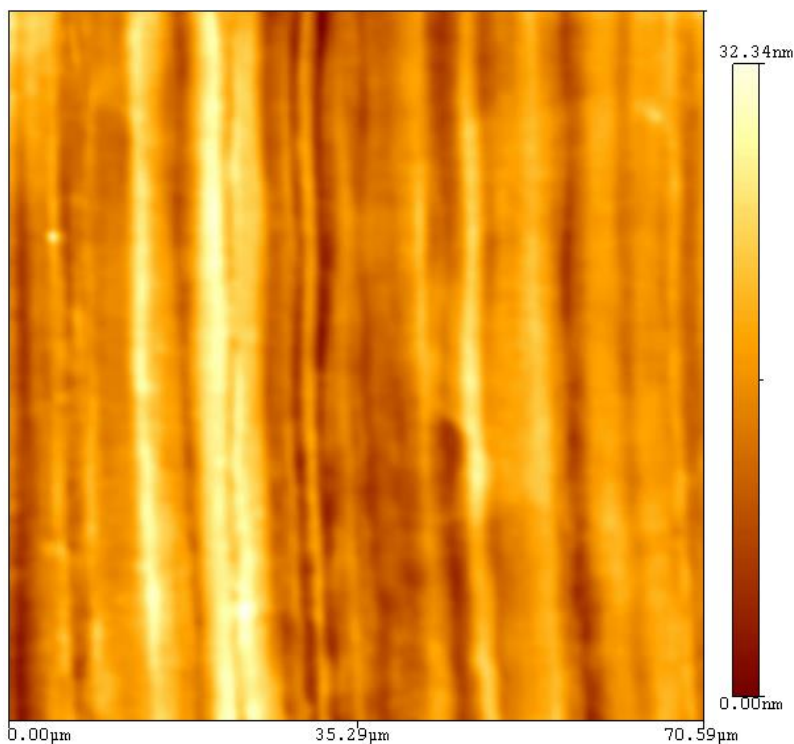


***Figure 4-9 Atomic force microscope image of a 70 μm × 70 μm region of the wear track region after completion of the run-in period.***

## ***4.6 Conclusions***

We have thus demonstrated that the mechano- and tribochemical processes occurring at sliding interfaces can be analyzed by considering the distribution of forces present at the sliding interface; only in the highest forces in the tail of the distribution are capable of reducing the activation energy sufficiently to lead to measurable reaction rates at room temperature. The broad distribution results in lateral forces that are both along and opposite to the direction of motion, the average of these forces being the measured frictional force. This arises because of the wide range of interactions between the methyl thiolate species at the contacting interface, which will depend in detail on their relative positions as they come into contact under the influence of the normal load

and the results indicate that significant mechanochemical rates can be obtained under mild sliding conditions. These results may help rationalize the intriguing discovery of graphitic tribological layers on the surface of metal-on-metal hip replacements,<sup>59-60</sup> which are unlikely to attain the temperatures required to thermally form such films. The *in-situ* kinetic methods developed in this work will provide a general strategy for understanding shear-induced mechanochemical reaction rates of surfaces and well-defined adsorbate layers, and can easily be extended to studying systems for which the reaction coordinate for the lowest-energy pathway is not oriented parallel to the surface to selectively induce non-thermal reactions. Combining this with the ability to use conventional surface analysis techniques to determine the composition of the surface formed after a mechanochemical reaction will provide a complete picture of the shear-induced surface chemistry.

## 4.7 References

1. Beyer, M. K.; Clausen-Schaumann, H., Mechanochemistry: The Mechanical Activation of Covalent Bonds. *Chem. Rev.* **2005**, *105*, 2921-2948.
2. Bowmaker, G. A., Solvent-Assisted Mechanochemistry. *Chem. Commun.* **2013**, *49*, 334-348.
3. Huang, Z.; Boulatov, R., Chemomechanics: Chemical Kinetics for Multiscale Phenomena. *Chem. Soc. Rev.* **2011**, *40*, 2359-2384.
4. Boulatov, R., Mechanochemistry: Demonstrated Leverage. *Nat Chem* **2013**, *5*, 84-86.
5. James, S. L., et al., Mechanochemistry: Opportunities for New and Cleaner Synthesis. *Chem. Soc. Rev.* **2012**, *41*, 413-447.
6. Eddleston, M. D.; Arhangelskis, M.; Friscic, T.; Jones, W., Solid State Grinding as a Tool to Aid Enantiomeric Resolution by Cocrystallisation. *Chem. Commun.* **2012**, *48*, 11340-11342.
7. Rief, M.; Oesterhelt, F.; Heymann, B.; Gaub, H. E., Single Molecule Force Spectroscopy on Polysaccharides by Atomic Force Microscopy. *Science* **1997**, *275*, 1295-1297.
8. Zlatanova, J.; Lindsay, S. M.; Leuba, S. H., Single Molecule Force Spectroscopy in Biology Using the Atomic Force Microscope. *Prog. Biophys. Mol. Biol.* **2000**, *74*, 37-61.
9. Hummer, G.; Szabo, A., Free Energy Surfaces from Single-Molecule Force Spectroscopy. *Acc. Chem. Res.* **2005**, *38*, 504-513.
10. Seema, P.; Behler, J.; Marx, D., Force-Induced Mechanical Response of Molecule-Metal Interfaces: Molecular Nanomechanics of Propanethiolate Self-Assembled Monolayers on Au(111). *PCCP* **2013**, *15*, 16001-16011.

11. Konôpka, M.; Turanský, R.; Dubecký, M.; Marx, D.; Štich, I., Molecular Mechanochemistry Understood at the Nanoscale: Thiolate Interfaces and Junctions with Copper Surfaces and Clusters. *J. Phys. Chem. C* **2009**, *113*, 8878-8887.
12. Xiao, X.-D.; Liu, G.-y.; Charych, D. H.; Salmeron, M., Preparation, Structure, and Mechanical Stability of Alkylsilane Monolayers on Mica. *Langmuir* **1995**, *11*, 1600-1604.
13. Lio, A.; Morant, C.; Ogletree, D. F.; Salmeron, M., Atomic Force Microscopy Study of the Pressure-Dependent Structural and Frictional Properties of N-Alkanethiols on Gold. *J. Phys. Chem. B* **1997**, *101*, 4767-4773.
14. Boscoboinik, J. A.; Kohlmeyer, R. R.; Chen, J.; Tysoe, W. T., Efficient Transport of Gold Atoms with a Scanning Tunneling Microscopy Tip and a Linker Molecule. *Langmuir* **2011**, *27*, 9337-9344.
15. Fraenkel, R.; Butterworth, G. E.; Bain, C. D., In Situ Vibrational Spectroscopy of an Organic Monolayer at the Sapphire–Quartz Interface. *J. Am. Chem. Soc.* **1998**, *120*, 203-204.
16. Frišćić, T.; Halasz, I.; Beldon, P. J.; Belenguer, A. M.; Adams, F.; Kimber, S. A. J.; Honkimäki, V.; Dinnebier, R. E., Real-Time and in Situ Monitoring of Mechanochemical Milling Reactions. *Nat Chem* **2013**, *5*, 66-73.
17. Kalin, M.; Vižintin, J., Comparison of Different Theoretical Models for Flash Temperature Calculation under Fretting Conditions. *Tribol. Int.* **2001**, *34*, 831-839.
18. Mazyar, O. A.; Xie, H.; Hase, W. L., Nonequilibrium Energy Dissipation at the Interface of Sliding Model Hydroxylated Alpha-Alumina Surfaces. *J. Chem. Phys.* **2005**, *122*, 094713-12.
19. Furlong, O. J.; Miller, B. P.; Tysoe, W. T., Shear-Induced Surface-to-Bulk Transport at Room Temperature in a Sliding Metal-Metal Interface. *Tribol. Lett.* **2011**, *41*, 257-261.

20. Furlong, O. J.; Miller, B. P.; Kotvis, P.; Tysoe, W. T., Low-Temperature, Shear-Induced Tribofilm Formation from Dimethyl Disulfide on Copper. *ACS Appl. Mater. Interfaces* **2011**, *3*, 795-800.
21. Furlong, O. J.; Miller, B. P.; Li, Z.; Walker, J.; Burkholder, L.; Tysoe, W. T., The Surface Chemistry of Dimethyl Disulfide on Copper. *Langmuir* **2010**, *26*, 16375-16380.
22. Kresse, G.; Joubert, D., From Ultrasoft Pseudopotentials to the Projector Augmented-Wave Method. *Phys. Rev. B* **1999**, *59*, 1758-1775.
23. Blöchl, P. E., Projector Augmented-Wave Method. *Phys. Rev B* **1994**, *50*, 17953-17979.
24. Kresse, G.; Hafner, J., Ab Initio Molecular Dynamics for Liquid Metals. *Phys. Rev B* **1993**, *47*, 558-561.
25. Kresse, G.; Furthmüller, J., Efficient Iterative Schemes for Ab Initio Total-Energy Calculations Using a Plane-Wave Basis Set. *Phys. Rev B* **1996**, *54*, 11169-11186.
26. Kresse, G.; Furthmüller, J., Efficiency of Ab-Initio Total Energy Calculations for Metals and Semiconductors Using a Plane-Wave Basis Set. *Comput. Mater. Sci.* **1996**, *6*, 15-50.
27. Perdew, J. P.; Burke, K.; Ernzerhof, M., Generalized Gradient Approximation Made Simple. *Phys. Rev. Lett.* **1996**, *77*, 3865.
28. Monkhorst, H. J.; Pack, J. D., Special Points for Brillouin-Zone Integrations. *Phys. Rev B* **1976**, *13*, 5188-5192.
29. Henkelman, G.; Uberuaga, B. P.; Jonsson, H., A Climbing Image Nudged Elastic Band Method for Finding Saddle Points and Minimum Energy Paths. *J. Chem. Phys.* **2000**, *113*, 9901-9904.

30. Henkelman, G.; Jónsson, H., Improved Tangent Estimate in the Nudged Elastic Band Method for Finding Minimum Energy Paths and Saddle Points. *J. Chem. Phys.* **2000**, *113*, 9978-9985.
31. Plimpton, S., Fast Parallel Algorithms for Short-Range Molecular Dynamics. *J. Comput. Phys.* **1995**, *117*, 1-19.
32. Nosé, S., A Unified Formulation of the Constant Temperature Molecular Dynamics Methods. *J. Chem. Phys.* **1984**, *81*, 511-519.
33. Hoover, W. G., Canonical Dynamics: Equilibrium Phase-Space Distributions. *Phys. Rev A* **1985**, *31*, 1695-1697.
34. Redhead, P. A., Thermal Desorption of Gases. *Vacuum* **1962**, *12*, 203-211.
35. Kauzmann, W.; Eyring, H., The Viscous Flow of Large Molecules. *J. Am. Chem. Soc.* **1940**, *62*, 3113-3125.
36. Johnson, K. L. Contact Mechanics. Cambridge University Press, Cambridge, 1985.
37. Miller, B.; Furlong, O.; Tysoe, W., Tribological Properties of 1-Alkenes on Copper Foils: Effect of Low-Coordination Surface Sites. *Tribol. Lett.* **2013**, *51*, 357-363.
38. Bell, G., Models for the Specific Adhesion of Cells to Cells. *Science* **1978**, *200*, 618-627.
39. Ribas-Arino, J.; Marx, D., Covalent Mechanochemistry: Theoretical Concepts and Computational Tools with Applications to Molecular Nanomechanics. *Chem. Rev.* **2012**, *112*, 5412-5487.
40. Jacobs, T. D. B.; Carpick, R. W., Nanoscale Wear as a Stress-Assisted Chemical Reaction. *Nat. Nano.* **2013**, *8*, 108-112.
41. Gotsmann, B.; Lantz, M. A., Atomistic Wear in a Single Asperity Sliding Contact. *Phys. Rev. Lett.* **2008**, *101*, 125501.

42. Dudko, O. K.; Hummer, G.; Szabo, A., Intrinsic Rates and Activation Free Energies from Single-Molecule Pulling Experiments. *Phys. Rev. Lett.* **2006**, *96*, 108101.
43. Konda, S. S. M.; Brantley, J. N.; Bielawski, C. W.; Makarov, D. E., Chemical Reactions Modulated by Mechanical Stress: Extended Bell Theory. *J. Chem. Phys.* **2011**, *135*, 164103-8.
44. Ribas-Arino, J.; Shiga, M.; Marx, D., Understanding Covalent Mechanochemistry. *Angew. Chem. Int. Ed.* **2009**, *48*, 4190-4193.
45. Prandtl, L., Ein Gedankenmodell Zur Kinetischen Theorie Der Festen Körper. *Z. Angew. Math. Mech.* **1928**, *8*, 85.
46. Furlong, O. J.; Manzi, S. J.; Pereyra, V. D.; Bustos, V.; Tysoe, W. T., Monte Carlo Simulations for Tomlinson Sliding Models for Non-Sinusoidal Periodic Potentials. *Tribol. Lett.* **2010**, *39*, 177-180.
47. Furlong, O. J.; Manzi, S. J.; Pereyra, V. D.; Bustos, V.; Tysoe, W. T., Kinetic Monte Carlo Theory of Sliding Friction. *Phys. Rev B* **2009**, *80*.
48. Fusco, C.; Fasolino, A., Velocity Dependence of Atomic-Scale Friction: A Comparative Study of the One- and Two-Dimensional Tomlinson Model. *Phys. Rev B* **2005**, *71*, 045413.
49. Gnecco, E.; Bennewitz, R.; Socoliuc, A.; Meyer, E., Friction and Wear on the Atomic Scale. *Wear* **2003**, *254*, 859-862.
50. Sasaki, N.; Tsukada, M.; Fujisawa, S.; Sugawara, Y.; Morita, S., Theoretical Analysis of Atomic-Scale Friction in Frictional-Force Microscopy. *Tribol. Lett.* **1998**, *4*, 125-128.
51. Tomlinson, G. A., A Molecular Theory of Friction. *Phil. Mag.* **1929**, *7*, 905.
52. Kariapper, M. S.; Fisher, C.; Woodruff, D. P.; Cowie, B. C. C.; Jones, R. G., A Structural Study of Methanethiolate Adsorbed on Cu(100). *J. Phys.: Condens. Matter* **2000**, *12*, 2153.

53. Driver, S. M.; Woodruff, D. P., Methanethiolate Structural Phases on Cu(100) and Cu(41;0). *Surf. Sci.* **2001**, *488*, 207-218.
54. Ferral, A.; Patrito, E. M.; Paredes-Olivera, P., Structure and Bonding of Alkanethiols on Cu(111) and Cu(100). *J. Phys. Chem. B* **2006**, *110*, 17050-17062.
55. Mikulski, P. T.; Gao, G.; Chateaneuf, G. M.; Harrison, J. A., Contact Forces at the Sliding Interface: Mixed Versus Pure Model Alkane Monolayers. *J. Chem. Phys.* **2005**, *122*, 024701-9.
56. Judith, A. H.; Schall, J. D.; Knippenberg, M. T.; Guangtu, G.; Paul, T. M., Elucidating Atomic-Scale Friction Using Molecular Dynamics and Specialized Analysis Techniques. *J. Phys.: Condens. Matter* **2008**, *20*, 354009.
57. Gao, F.; Furlong, O.; Kotvis, P. V.; Tysoe, W. T., Pressure Dependence of Shear Strengths of Thin Films on Metal Surfaces Measured in Ultrahigh Vacuum. *Tribol. Lett.* **2008**, *31*, 99-106.
58. Greenwood, J. A.; Williamson, J. B. P., Contact of Nominally Flat Surfaces. *Proc. R. Soc. London, Ser. A* **1966**, *295*, 300-319.
59. Liao, Y.; Hoffman, E.; Wimmer, M.; Fischer, A.; Jacobs, J.; Marks, L., CoCrMo Metal-on-Metal Hip Replacements. *PCCP* **2013**, *15*, 746-756.
60. Liao, Y.; Pourzal, R.; Wimmer, M. A.; Jacobs, J. J.; Fischer, A.; Marks, L. D., Graphitic Tribological Layers in Metal-on-Metal Hip Replacements. *Science* **2011**, *334*, 1687-1690.

# Chapter 5

## Analysis of Diethyl and Dimethyl Dithiol Decomposition Pathways

### *5.1 Introduction*

Tribochemical reactions occur at a buried solid-solid interface so that obtaining information on the elementary steps in the reaction pathway and their rates becomes a particular challenge due to the lack of surface-sensitive techniques available for analyzing the nature of such a buried interface. In some cases, the sliding interface can be analyzed using optical techniques as long as the material of one of the counter faces is transparent<sup>1-5</sup>. However, because the thermal reactions of a lubricant or lubricant additive, and perhaps the tribochemistry are influenced by the nature of the contacting surfaces, such strategies are not generally applicable, in particular for understanding the role of the surface itself in the reaction. While direct, in-situ analyses, defined as the analysis of the sliding interface *during* rubbing, are the most valuable for determining reaction pathways and their kinetics, such techniques are sparse, and must be supplemented by ex-situ analyses. The latter is the most common approach to analyze tribofilms. Ex-situ analyses are most often carried out by removing the sample from the tribometer. This has the advantage that a number of different techniques can be used to analyze the same region to obtain a full picture of the nature and structure of the boundary film. However, this type of ex-situ analysis potentially

suffers from two problems. First, the surface may change either with time or due to atmospheric exposure; second, the evolution of the nature of the boundary film as a function of time, or the number of scans cannot be obtained using such ex-situ analyses since it is essentially impossible to replace the sample into the tribometer at exactly the same location. Thus, more revealing ex-situ analyses are those that are performed in the same location as a function of the number of scans with the sample always inside the tribometer. The rubbed regions in the majority of tribometers are narrow, since they usually involve a ball sliding on a flat sample, and therefore such analytical techniques should have reasonably good spatial resolution and be surface sensitive. Issues of atmospheric contamination are also important in such experiments and are addressed in this work by using an ultrahigh vacuum (UHV) tribometer to minimize and hopefully eliminate such effects.

Because of the lack of access of spectroscopic probes (for example, photons or electrons) to a non-transparent solid-solid interface, there are, as far as we are aware, only three in-situ techniques available for studying chemical reactions and their rates at such interfaces. The first is to measure the change in friction force as a surface reaction proceeds. By arguing that the different intermediates and products have different characteristic frictional properties, the time dependence of the friction force (or friction coefficient) reflects the kinetics of the surface reaction. Thus, if there are several reactants, intermediates and products on the surface, and if the  $i^{\text{th}}$  component has a relative, pass-dependent coverage  $\Theta_i(p)$ , with an associated friction coefficient  $\mu_i$ , then the time evolution of the friction coefficient  $\mu(t)$  can be written as:

$$\mu(t) = \sum_i \mu_i \Theta_i(p) \quad (1).$$

This approach is particularly useful in the case of a simple, first-order reaction,  $A_{(ads)} \rightarrow B_{(ads)}$  since,  $\mu_A$  and  $\mu_B$  can be measured before and after reaction to obtain the pass-dependent coverages and has recently been used to follow shear-induced reactions in an atomic force microscope (AFM) <sup>6</sup>.

The second approach is to measure the electrical contact resistance while sliding <sup>7-10</sup>. This technique tends to be more useful for thicker films, but is often difficult to interpret unless the film structure and its conductivity are known. The final approach is to measure the gas-phase products evolved during rubbing using a mass spectrometer. Since the amount of product formed from such a small contact is relatively low, these experiments are carried out under high <sup>11,12</sup> or ultrahigh vacuum <sup>13</sup>. This approach allows both the reaction kinetics to be measured and the nature of the gas-phase products to be monitored.

Since the information available from the in-situ techniques described above is sparse, it must be supplemented with ex-situ analyses as a function of the number of times that the surface is rubbed (referred to in the following as “the number of scans”) within the wear track. This approach requires surface-sensitive (electron-based) spectroscopic techniques with reasonable spatial resolution to allow the nature of the worn and unworn regions to be compared. X-ray photoelectron spectroscopy is perhaps the most chemically sensitive surface analysis technique <sup>14</sup> but is often difficult to incorporate directly into the UHV chamber and is usually included in a separate analytical chamber. Techniques based on excitation by high-energy electron beams are experimentally easier since the electron source is more compact than an X-ray source and does not need to be too close to the sample. There are several electron-based spectroscopic techniques that can be used, notably Auger spectroscopy <sup>14</sup>, which provides elemental information, and electron energy loss spectroscopy, which can be chemically specific <sup>15,16</sup>.

The approach is illustrated in this work by using shear-induced boundary layer formation from the reaction of dialkyl disulfides on copper in ultrahigh vacuum <sup>17</sup>.

## ***5.2 Experimental***

Tribological measurements were carried out in a stainless-steel, UHV chamber operating at a base pressure of  $\sim 2 \times 10^{-10}$  Torr following bake out, which has been described in detail elsewhere <sup>18</sup>. Briefly, the chamber was equipped with a UHV-compatible tribometer, which simultaneously measures the normal load, lateral force and contact resistance between the tip and substrate and the experimental conditions and the data collection were controlled by a LabView program. Previous work has demonstrated that the maximum interfacial temperature rise for a copper sample under the experimental conditions used ( $4 \times 10^{-3}$  m/s sliding speed, 0.44 N normal load) is much less than 1 K. All experiments were carried out by initially rubbing the tribopin (made of tungsten carbide covered by a copper transfer film of  $1.27 \times 10^{-2}$  m in diameter) against the clean copper sample until a constant friction coefficient was obtained, a process that usually required  $\sim 50$  scans. The reactants were dosed through a leak valve connected to a dosing tube (with an internal diameter of  $4 \times 10^{-3}$  m) directed towards the sample so that the pressure at the sample surface is enhanced compared to the measured background pressure. The chamber was also equipped with a single-pass cylindrical-mirror analyzer (CMA) for Auger analysis, and an argon ion bombardment source for sample cleaning and depth profiling. A high-resolution electron gun with a beam energy of 5 keV, and a channeltron secondary electron detector, were also incorporated into the system. This allowed scanning electron microscopy (SEM) images and Auger profiles of the wear scars to be collected. Finally, the chamber also included a quadrupole

mass spectrometer for leak checking, detecting gas-phase products formed during rubbing and for gauging reactant purity.

The copper samples (Alfa Aesar, 99.99% pure, 1 mm thick) were polished to a mirror finish using 1  $\mu\text{m}$  diamond paste and then rinsed with deionized water and ultrasonically degreased in acetone. Once in UHV, the copper foils were cleaned using a standard procedure, which consisted of argon ion bombardment ( $\sim 1$  kV,  $\sim 2$   $\mu\text{A}/\text{cm}^2$ ) and annealing cycles up to  $\sim 850$  K. The cleanliness of the samples was monitored using Auger spectroscopy, where only Auger peaks due to copper were detected after cleaning.

The dimethyl disulfide (DMDS, Aldrich, 99.0% purity) and diethyl disulfide (DEDS, Aldrich, 99.0% purity) were transferred to glass bottles and attached to the gas-handling systems of the vacuum chamber, where they were subjected to several freeze-pump-thaw cycles. The purity of the compounds was monitored using mass spectroscopy.

### **5.3 Results**

The shear-induced reaction pathways of DMDS and DEDS were explored on clean copper foils in UHV<sup>19</sup>. A substantial amount of previous work has been carried out on DMDS, where it was shown that methane is the predominant reaction product, although some ethylene and ethane are formed so that all carbonaceous species are removed from the surface<sup>13,17</sup>, similar to the thermally formed products at higher temperatures<sup>20</sup>. Repeated rubbing creates a clean surface by removing the outermost layers<sup>17</sup>, and it has been shown that shear causes the resulting adsorbed sulfur to penetrate the bulk of the sample<sup>21</sup>, in a mechanism proposed to occur by the formation of Kelvin-Helmholtz instabilities at the sliding surface<sup>22-28</sup>.

Experiments were also carried out to detect the desorption products from a surface exposed to DEDS using a mass spectrometer placed in-line-of-sight of the sample, and a typical plot of the mass spectrometer signal at 26 amu is shown in Figure 1, plotted as a function of the number of scans after saturating the surface (by exposure to 0.7 L of DEDS) that had been previously rubbed 50 times to create a wear track. The experiment was carried out as follows. The pin was brought into contact at a preset load of 0.44 N, where the load was controlled by the LabView software. The sample was rubbed once while continually monitoring the mass spectrometer signal, and gas-phase species were detected only during rubbing, giving rise to the pulses seen in Figure 1. After the surface had been rubbed, the pin was brought out of contact, and then brought into contact once again to ensure that the loads were identical for each pass over the substrate. This procedure was repeated until no more gas-phase products were detected. The lack of signal when the surface was not being rubbed indicates that the gas-phase products are formed by rubbing, not by thermal decomposition of the adsorbate. Finally, since the time for the pin to approach the surface varies somewhat for each pass, the time interval between the pulses is not uniform. The data were collected using a sliding speed of 4 mm/s at a normal load of 0.44 N for a distance of 1 cm. The background pressure in the chamber remained constant during these experiments because of the small amount of gas-phase products formed during sliding. The plot shows distinct gas pulses that decrease in intensity as the surface becomes depleted of ethyl thiolate species<sup>29</sup> due to rubbing. Since reaction occurs in the contact between the pin and the copper substrate, the total amount of gas-phase products detected will depend on sliding distance, but the decay in the signal as a function of the number of scans will be independent of sliding distance. Furthermore, since the sliding distance is much larger than the size of the contact between the pin and substrate, the contribution to the signal from the surface of the pin is negligible.

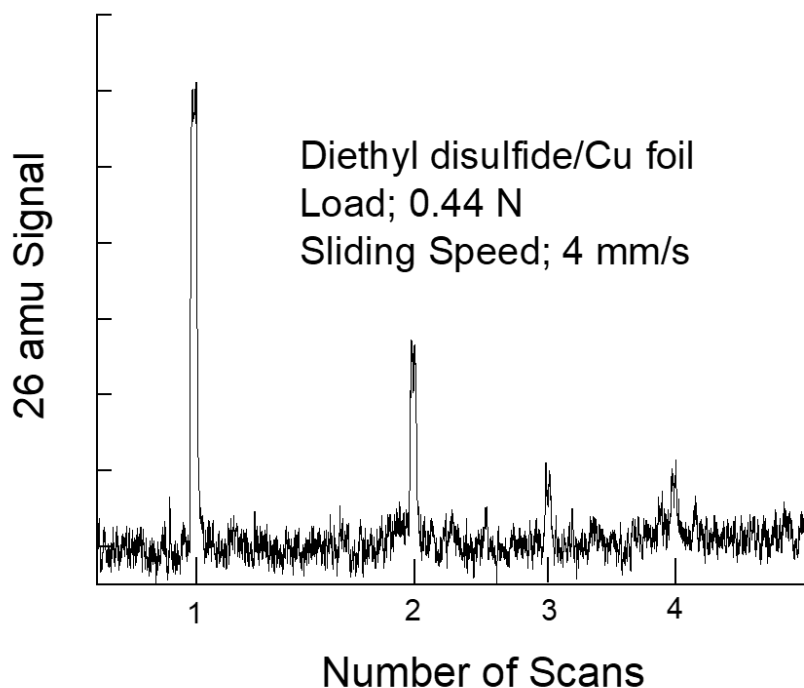


***Figure 5-1 Plot of the 26 amu signal as a function of the number of scans at a load of 0.44 N at a sliding speed of 4 mm/s, after exposing the copper foil to 0.7 L of DEES. Note that the unequal intervals between scans arises from the different times between scans***

Similar results have been previously found when rubbing a methyl-thiolate-covered surface formed by dosing DMDS, to form methyl thiolate species on the surface, under the same sliding conditions <sup>13</sup>, and show a similar exponential decay in the intensity of the methane desorption pulses as a function of the number of scans,  $p$ . Experiments carried out by rubbing while continually dosing the surface showed only sulfur, but essentially no carbon on the surface and in the subsurface region of the sample indicating that carbon is completely removed as gas-phase products [17]. Assuming that the exponential decay of signal is time-dependent then the reaction time during sliding  $t(p)$  is proportional to the number of scans, so that  $t(p) = t_c p$ , where  $t_c$  is the time that a chemical species on the surface spends in the contact. An exponential decay in signal

intensity indicates that the methyl thiolate species decomposes via a first-order process <sup>13</sup> with a rate constant  $k_1$ , so that the thiolate coverage  $\Theta_{th}$  is given by:

$$\Theta_{th}(p) = \exp(-k_1 t_c p) \quad (2)$$

Note that the coverage  $\Theta$  is taken to be the relative coverage, that is, the number of adsorbates per surface copper atom ratioed to the maximum number of adsorbates that can be accommodated per surface atom, so that  $0 \leq \Theta \leq 1$ . A fit to the experimental data for methyl thiolate decomposition gives  $k_1 t_c = 0.63 \pm 0.03$  <sup>13</sup>.

Auger analyses of the sulfur coverage in the worn region show that the amount of sulfur decreases as a function of the number of scans (Figure 2). Here the clean copper was rubbed 50 times to create an initial wear track. The sample was then exposed to DMDS to create a saturated methyl thiolate over layer, and rubbed under a load of 0.44 N at a sliding speed of 4 mm/s; Auger spectra were collected in the same position at various intervals. In addition, it was found that redosing the surface with DMDS after rubbing a saturated thiolate-covered surface ~8 times, until the methane desorption had decreased to zero, leads to the evolution of an identical amount of methane as found after the first dose <sup>13</sup>. This indicates that a clean surface is formed after ~ 8 scans due to the shear-induced transport of practically all of the absorbed sulfur into the copper substrate <sup>17,21</sup>.

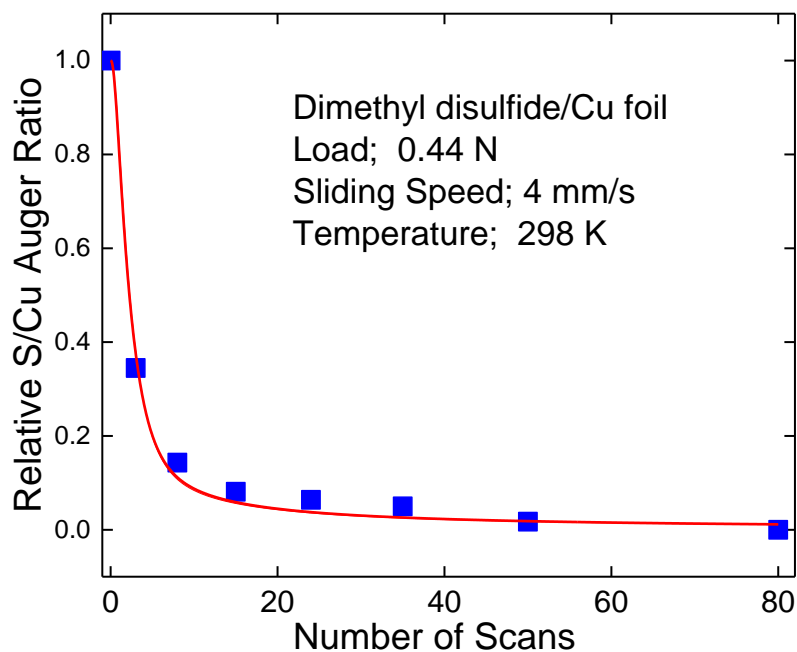


***Figure 5-2 Plot of relative coverage of the sulfur in the wear track measured by small-spot-size Auger spectroscopy as a function of the number of scans for a methyl thiolate over layer on the surface, where the sulfur peak-to-peak intensity is normalized to that of the copper substrate. The normal load was 0.44 N, the sliding speed was 4 mm/s and the surface was pre-covered with thiolate species after a wear track had been created by rubbing the clean copper surface 50 times. The line through the data is a fit to the kinetic model***

As discussed above, the variation in friction coefficient can be used to monitor the change in the nature of the surface due to shear-induced reactions. The resulting plot of friction coefficient as a function of the number of scans is shown in Figure 3 for a methyl thiolate-covered surface rubbed at a sliding speed of 4 mm/s under a load of 0.44 N. Here the friction coefficient increases from an initial value of  $\sim 0.25$  up to a final value of  $\sim 0.5$ , similar to the value previously found for clean copper<sup>17</sup>. The line in the figure is a fit to the data, discussed in greater detail below.

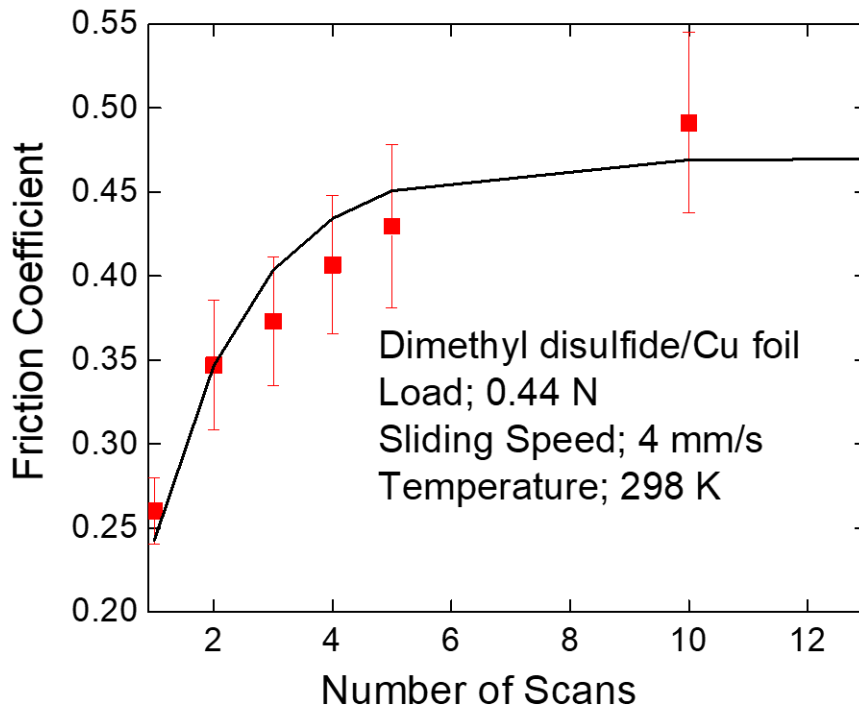


**Figure 5-24** Plot of the friction coefficient as a function of the number of scans while rubbing a methyl thiolate covered copper surface at a normal load of 0.44 N and a sliding speed of 4 mm/s. The line shows a fit to the data (see Discussion section).

Similar kinetic experiments were carried out for copper dosed with DEDS, which forms ethyl thiolate species on the surface <sup>29</sup>. These experiments also yielded pulses of gas-phase products during sliding as shown in Figure 1 measured while monitoring 26 amu. In order to establish how the amount of evolved gas from ethyl thiolate species on the surface depends on DEDS exposure, the integrated area of the mass spectrometer signal during the first pass at 26 amu was measured as a function of DEDS exposure in Langmuirs (1 Langmuir (L) =  $1 \times 10^{-6}$  Torr s). The results are displayed in Figure 4 and a line is plotted through the data as a guide to the eye. It is observed that the yield of gas-phase products increases with DEDS exposure, but saturates at an exposure of  $\sim 0.2$  L. Note, however, that exposures were measured from the background pressure

in the vacuum chamber, while the local pressure at the sample is higher. Exposures of 0.7 L were used for subsequent experiments to ensure that the surface was saturated.

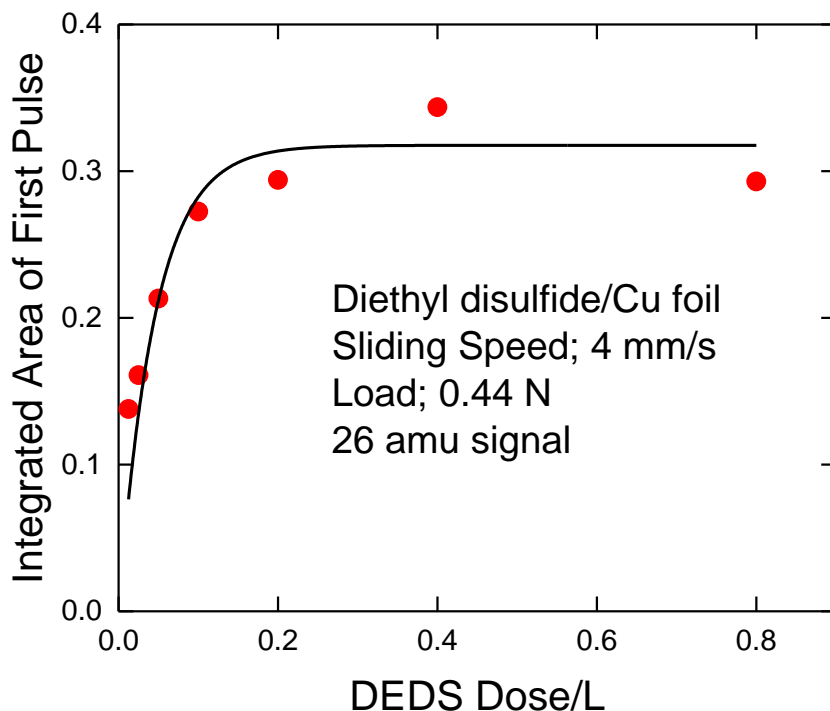


**Figure 5-25** Plot of integrated areas of the first desorption pulse collected at 26 amu as a function of DEDS exposure in Langmuir ( $1 \text{ Langmuir (L)} = 1 \times 10^{-6} \text{ Torr s}$ ) from a dosing tube directed at the sample (●). A line is drawn through the data as a guide to the eye.

Experiments were carried out to monitor the gas-phase products formed during sliding for an ethyl thiolate-saturated sample obtained by dosing with DEDS, similar to the results displayed in Figure 1, by monitoring mass spectrometer signals at 2, 15, 16, 26, 29, 30 and 58 amu; no signals were detected at 2, 16 and 58 amu indicating that no hydrogen, methane or C<sub>4</sub> hydrocarbons were produced at the sliding interface. The 28 amu signal was not measured because of the large intensity at this mass due to residual carbon monoxide in the vacuum chamber; these results are

displayed in Figure 5, which plots the integrated peak areas for each desorption pulse at various masses as a function of the number of scans. This shows that the yield at all masses decreases in a similar manner as each other as a function of the number of scans. The signals at 30, 29 and 15 amu are due to ethane, and their relative intensities, along with others, are in good agreement with the mass spectrometer ionizer fragmentation pattern of ethane, measured in the same mass spectrometer used to collect the data in Figure 5. The 26 amu signal is mainly due to ethylene formation, but also contains contributions from the fragmentation of ethane in the mass spectrometer ionizer. The amount of ethylene produced during rubbing is calculated by subtracting the mass spectrometer contribution at 26 amu due to ethane using its fragmentation pattern. The ethane and ethylene yields as a function of the number of scans are shown as an inset into Figure 5. Plots of  $\ln(\text{Yield})$  versus  $p - 1$  were linear and yielded essentially identical values of  $k_1 t_c$  ( $0.60 \pm 0.14$  for ethane formation and  $0.74 \pm 0.04$  for ethylene formation). This suggests a common rate-limiting step for both reactions which, based on density functional theory calculations for methyl thiolate species on copper, is proposed to be due to shear-induced C-S bond scission to form alkyl species and sulfur on the surface<sup>13</sup>.

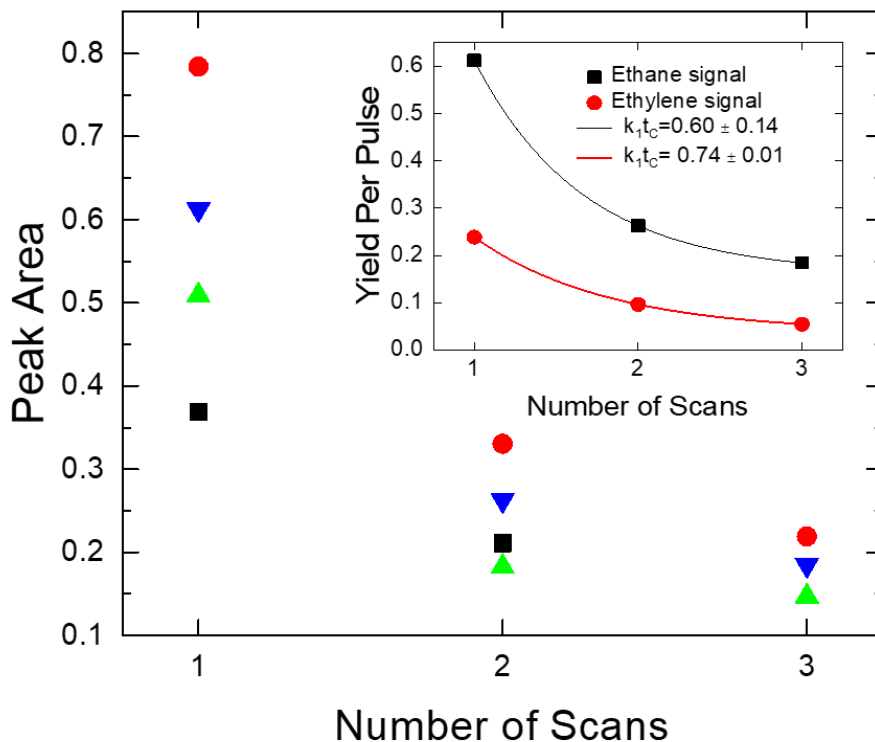


**Figure 5-5** Plot of the variation in integrated intensities of the 15 (■), 26 (●), 29 (▲) and 30 (▼) amu signals as a function of the number of scans, after saturating a copper surface, that had previously been rubbed 50 times, with an exposure of 0.8 L of DEDES; a sliding speed of 4 mm/s and a normal load of 0.44 N, were used. Shown as an inset is a plot of the integrated area per pulse for ethane (■) and ethylene (●) formation. The ethane signal is calculated by subtracting the contribution due to ethane fragmentation using the fragmentation pattern for ethane measured using the same mass spectrometer as used to collect the shear-induced desorption data.

Finally, a plot of friction coefficient as a function of the number of scans for an ethyl thiolate-covered surface is shown in Figure 6, at a sliding speed of 4 mm/s at a load of 0.44 N. The line is a fit to the data, discussed in greater detail below.

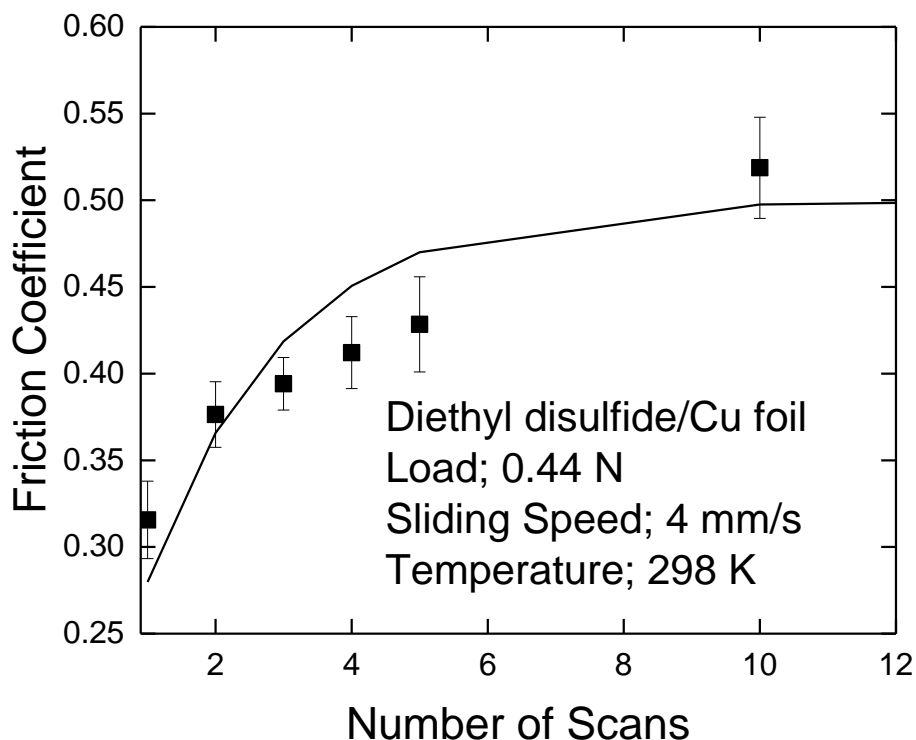


**Figure 5-26** Plot of the friction coefficient as a function of the number of scans while rubbing an ethyl thiolate covered copper surface at a normal load of 0.44 N at a sliding speed of 4 mm/s. The line shows a fit to the data (see Discussion section).

## 5.4 Discussion

At room temperature, both DMDS and DEDS react on copper by S–S bond scission to form alkyl thiolate species on the surface<sup>20,29</sup>. They decompose at ~300 K under the influence of shear via a first-order reaction, with rate constant  $k_1$  to produce hydrocarbons, predominantly methane with some C<sub>2</sub> hydrocarbons in the case of methyl thiolate species, and ethylene and ethane in the case of ethyl thiolate, along with adsorbed sulfur. The adsorbed sulfur is then transported into the bulk under the influence of shear<sup>17,21,30</sup> to form a sulfur-containing boundary film. This

reforms a clean copper surface that allows the reaction cycle to proceed once again. The reaction pathway consists of a sequence of two shear-induced reactions:  $RS_{(ads)} \rightarrow S_{(ads)} \rightarrow S_{(subsurface)}$ , where the rate constant for the first reaction is  $k_1$  and for the second is denoted as  $k_2$ . The first-order decomposition of the alkyl thiolates yields a coverage as a function of the number of scans  $p$  given by Eqn. 2. If the coverage of adsorbed sulfur,  $S_{(ads)}$  formed by this reaction is denoted  $\Theta_S$  then, from the sequential reaction, adsorbed sulfur is formed by alkyl thiolate decomposition and removed by surface-to-bulk transport:

$$\frac{d\Theta_S}{dt} = k_1\Theta_{th} - k_2\Theta_S \quad (3),$$

assuming that surface-to-bulk transport occurs via a first-order process and this will be discussed in greater detail below. The time variation in alkyl thiolate coverage  $\Theta_{th}$  is given by Eqn. (2) so that substituting into Eqn. 3 gives:

$$\frac{d\Theta_S}{dt} = k_1e^{-k_1t} - k_2\Theta_S \quad (4).$$

This can be solved analytically to give:

$$\Theta_S = \frac{k_1}{k_2 - k_1} (e^{-k_1t} - e^{-k_2t}) \quad (5).$$

Writing this as a function of the number of scans  $p$ , gives:

$$\Theta_S(p) = \frac{k_1}{k_2 - k_1} (e^{-k_1tcp} - e^{-k_2tcp}) \quad (6).$$

Since the Auger analyses (Figure 2) measure the sulfur from both adsorbed sulfur species and alkyl thiolate species, the coverage of all sulfur-containing species is calculated as  $\Theta_S(tot) = \Theta_S + \Theta_{th}$ , and this gives:

$$\Theta_S(tot) = \frac{k_2}{k_2 - k_1} e^{-k_1 t c p} - \frac{k_1}{k_2 - k_1} e^{-k_2 t c p} \quad (7).$$

However, it should be noted that the sampling depth in Auger spectroscopy depends on the electron escape depth and will thus also detect signals from subsurface sulfur,  $S_{(subsurface)}$ ; strategies for addressing this issue are discussed below. Finally, the coverage of the clean surface,  $\Theta_{clean}$  is calculated from:

$$\Theta_{clean} = 1 - \Theta_S - \Theta_{th} \quad (8).$$

Surface-to-bulk transport kinetics have previously been analyzed<sup>17,21,30</sup> following a model proposed by Rigney<sup>22-25,27,28,31,32</sup> in which Kelvin-Helmholtz instabilities cause the atoms at the surface to move into the subsurface region. The film penetrates a distance  $d(p)$  into the subsurface region as a function of the number of scans as:  $d(p) = d_p p^x$ , where  $d_p$  is the distance that the sulfur penetrates the subsurface region per pass. The exponent  $x$  depends on the strain-rate sensitivity of the substrate which is expected to be approximately zero for a metal. While the value of the strain-rate sensitivity is likely to evolve as the mechanical properties change during sliding, the sulfur depth distribution and the variation in the Auger signal as a function of number of scans have been found previously to be consistent with  $x \sim 1$ <sup>30</sup>. If the initial film thickness at  $t = 0$  is  $d_0$  (corresponding to the thickness of the original saturated sulfur over layer), then during shear for a time in the contact  $\delta t$ , the width of the shear-induced region increases by  $\delta z$ . A value of  $x = 1$  implies that  $\delta z \propto \delta t$  so that:  $\frac{dz}{dt} = k$  where  $k$  is a constant to be determined. If the initial (sulfur) coverage is  $\Theta_0$  with a thickness of  $d_0$  and, since the number of atoms is conserved, when sulfur is transported into the substrate, the sulfur coverage is reduced such that  $\Theta_S d = constant = \Theta_0 d_0$ . Thus, during a time  $\delta t$  the coverage changes by  $\delta \Theta$  where:

$$\Theta_0 d_0 = (d_0 + k\delta t)(\Theta_0 + \delta\Theta) \quad (9),$$

to give  $\frac{d\Theta_S}{dt} = -\frac{k\Theta_S}{d_0}$ . If the number of scans over the surface is  $p$ , and the contact time is  $t_C$ , then over  $p$  scans the total contact time is  $pt_C$  and, from the above equation, the film will spread a distance  $d_p p$ . Integrating  $\frac{dz}{dt} = k$  shows that  $k = \frac{d_p}{t_C}$ . Thus, the surface-to-bulk transport rate equation is:

$$\frac{d\Theta_S}{dt} = -\frac{d_p \Theta_S}{d_0 t_C} \quad (8),$$

which is a first-order reaction with respect to  $\Theta_S$ , as assumed in the above analysis. Writing  $k'_1 = k_1 t_C$  yields the following equation for the sulfur coverage, modified from Eqn. 6 as:

$$\Theta_S = \frac{k'_1}{\frac{d_p}{d_0} - k'_1} \left( e^{-k'_1 p} - e^{-\frac{d_p}{d_0} p} \right) \quad (10).$$

However, surface spectroscopies, including Auger spectroscopy, are sensitive not only to adsorbates but also include signals from the sub-surface region<sup>14,33</sup>. It has been previously shown that the Auger signal due to subsurface sulfur varies as  $1/p^{30}$  so that the Auger signal contribution arising from subsurface sulfur is taken to be  $\propto \frac{\Theta_{subsurface}}{p+1}$  where  $\Theta_{subsurface}$  is the subsurface sulfur coverage and  $p + 1$  is used to avoid a singularity at  $p = 0$ . Therefore, the sulfur Auger signal  $I_{Auger}(p)$  is given by:

$$I_{Auger}(p) \propto I_{Auger}(S) + I_{Auger}(th) + \frac{\alpha \Theta_{subsurface}}{p+1} \quad (11),$$

where  $\alpha$  is a constant. Since  $\Theta_{subsurface} = 1 - \Theta_{th} - \Theta_S$ , this yields:

$$I_{Auger}(p) = \left( \frac{\frac{d_p}{d_0}}{\frac{d_p}{d_0} - k'_1} e^{-k'_1 p} - \frac{k'_1}{\frac{d_p}{d_0} - k'_1} e^{-\frac{d_p}{d_0} p} \right) \left( 1 - \frac{\alpha}{p+1} \right) + \left( \frac{\alpha}{p+1} \right) \quad (12),$$

which is normalized to the initial Auger signal of the clean surface.

## Analysis of Methyl Thiolate Kinetics

The above kinetic equations allow the rates of the shear-induced elementary reaction steps of alkyl thiolates on copper to be analyzed. We start with the decomposition of methyl thiolate species for which  $k_1 t_C = k'_1 = 0.63 \pm 0.03$  as obtained above. In order to obtain  $d_p/d_0$ , the sulfur Auger data (Figure 2) are fit to Eqn. 12 to yield values of  $\alpha = 0.9 \pm 0.1$  and  $d_p/d_0 = 2.5 \pm 0.5$ . The results are verified by fitting to the friction data in Figure 3 by rewriting Eqn. 1 as:

$$\mu(p) = \mu_{th} \Theta_{th}(p) + \mu_S \Theta_S(p) + \mu_{clean} (1 - \Theta_{th}(p) - \Theta_S(p)) \quad (13),$$

where  $\mu_{th}$ ,  $\mu_S$  and  $\mu_{clean}$  are the characteristic friction coefficients of the thiolate-covered, sulfur-covered and clean surfaces, respectively. Here, the rate constants were constrained to be in the range determined above and  $\mu_{clean}$  was allowed to vary between 0.45 and 0.55 found for sliding on clean copper. The fit to the data is shown as a solid line in Figure 3 and yields  $\mu_{th} = 0.07 \pm 0.02$ ,  $\mu_S = 0.39 \pm 0.06$ , and  $\mu_{clean} = 0.47 \pm 0.05$ . The resulting plot of the adsorbate coverages as a function of the number of scans for an initially methyl thiolate-saturated surface, at a load of 0.44 N and a sliding speed of 4 mm/s, is shown in Figure 7. This shows that a clean surface is indeed produced after  $\sim 8$  scans, since the clean surface coverage ( $\blacktriangle$ ) becomes almost unity after this number of scans, thereby allowing the tribochemical cycle to be repeated to eventually form a sulfur-containing boundary film. In addition, as a consequence of  $d_p/d_0$  being much larger than

$k'_1$ , the sulfur is transported into the subsurface region almost as quickly as it is formed on the surface resulting in the adsorbed sulfur coverage always remaining less than 0.2 monolayers (●).

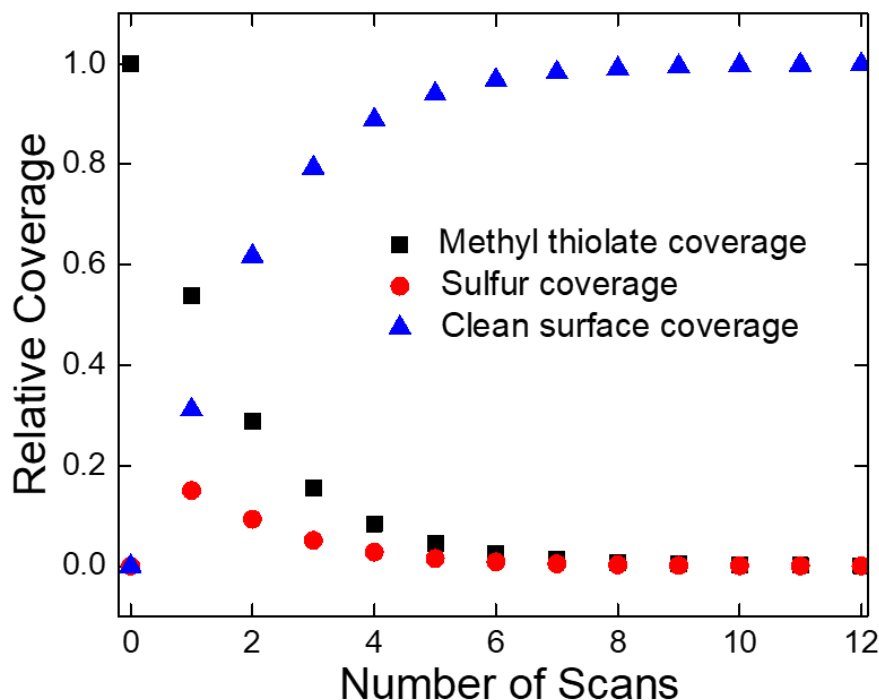


*Figure 5-7 Plot of the calculated coverages of adsorbed methyl thiolate species (■), adsorbed sulfur (●) and the clean copper (▲) surface as a function of the number of scans over a methyl-thiolate covered surface with a normal load of 0.44 N and a sliding speed of 4 mm/s.*

### Analysis of Ethyl Thiolate Kinetics

A similar analysis was carried out for the shear-induced decomposition of ethyl thiolate species formed from DEDS on copper. The values of  $k_1 t_c (k'_1)$  are  $0.60 \pm 0.14$  for ethane formation and  $0.74 \pm 0.04$  for ethylene production (Figure 5), and therefore are similar to the values found for methyl thiolate species, consistent with the rate-limiting steps for both reactions being similar. These kinetic parameters are used to fit to the variation in friction coefficient as a function

of the number of scans to verify that the kinetic measurements are consistent with in-situ measurements of the shear-induced chemistry (Figure 6). The fit to the data yields a value of  $d_p/d_0 = 2.5 \pm 0.5$ , identical to that found for methyl thiolate decomposition, and yields an optimum value of  $k_1 t_C (k'_1) = 0.50 \pm 0.05$ , slightly lower than the corresponding value for methyl thiolate species on copper. The best fit to the experimental data (shown as a line in Figure 6) is obtained with characteristic friction coefficients of  $\mu_{th} = 0.15 \pm 0.04$ ,  $\mu_S = 0.43 \pm 0.06$ , and  $\mu_{clean} = 0.50 \pm 0.05$ . As expected, the last two values,  $\mu_S$  and  $\mu_{clean}$ , are in good agreement with those for a methyl thiolate covered surface. However, the friction coefficient for a saturated layer of ethyl thiolate species on copper is somewhat larger ( $\sim 0.15$ ) than that found for methyl thiolate species ( $\sim 0.07$ ).

The resulting plot of adsorbate coverages for shear-induced ethyl thiolate decomposition as a function of the number of scans is displayed in Figure 8 which, because of the similar rate constants for the various shear-induced processes is similar to that found for methyl thiolate species (Figure 7). In particular, a clean surface is formed after  $\sim 8$  scans since the clean surface coverage approaches unity ( $\blacktriangle$ ), and the sulfur coverage remains low because of the relatively larger value of  $d_p/d_0$  than  $k'_1$  ( $\bullet$ ).

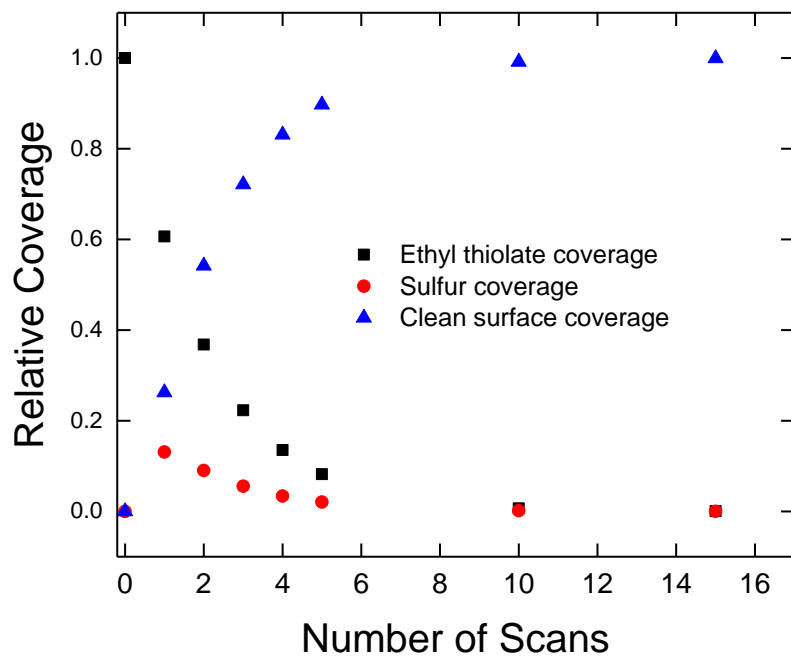


*Figure 5-8 Plot of the calculated coverages of adsorbed ethyl thiolate species (■), adsorbed sulfur (●) and the clean copper (▲) surface as a function of the number of scans over an ethyl-thiolate covered surface with a normal load of 0.44 N and a sliding speed of 4 mm/s.*

## 5.5 Conclusions

The shear-induced reaction pathways and the elementary step kinetics for sliding-induced decomposition of alkyl thiolate species on copper are explored using in-situ and ex-situ techniques. The shear-induced reaction pathways are preceded by a thermal reaction that involves S–S bond scission to deposit alkyl thiolate species on the copper surface. Shear induces thiolate decomposition to evolve gas-phase hydrocarbons, followed by rapid shear-induced surface-to-bulk transport of adsorbed sulfur to produce subsurface sulfur. This process recreates a clean surface that allows the cycle to be repeated so that the dialkyl disulfides act as gas-phase lubricants. While ex-situ experiments, by definition, do not necessarily reflect the nature of the contacting interface

during rubbing, carrying out such experiments in ultrahigh vacuum minimizes the possibility of atmospheric reactions with the surface. In addition, the results can be validated by comparing the results of ex-situ measurements with in-situ measurements of friction force. It is thus expected that such an approach will be generally useful for determining shear-induced reaction pathways and their kinetics.

Since, in the case of the shear-induced alkyl thiolate reactions, the rate of surface-to-bulk transport is higher than the rate of thiolate decomposition, it is essentially a single rate-limiting-step reaction,  $RS_{(ads)} \rightarrow S_{(subsurface)}$ . This offers the possibility of following the shear-induced reaction kinetics for a well-defined reaction pathway, in this case, alkyl thiolate decomposition, just by measuring the evolution in friction force using an AFM.

## ***5.6 References***

1. Fraenkel, R., Butterworth, G.E., Bain, C.D.: In Situ Vibrational Spectroscopy of an Organic Monolayer at the Sapphire–Quartz Interface. *Journal of the American Chemical Society* **120**(1), 203-204 (1998).
2. Piras, F.M., Rossi, A., Spencer, N.D.: Growth of Tribological Films: In Situ Characterization Based on Attenuated Total Reflection Infrared Spectroscopy. *Langmuir* **18**(17), 6606-6613 (2002).
3. Scharf, T.W., Singer, I.L.: Monitoring Transfer Films and Friction Instabilities with In Situ Raman Tribometry. *Tribology Letters* **14**(1), 3-8 (2003).

4. Dvorak, S., Wahl, K., Singer, I.: In Situ Analysis of Third Body Contributions to Sliding Friction of a Pb–Mo–S Coating in Dry and Humid Air. *Tribology Letters* **28**(3), 263-274 (2007).
5. Sawyer, W.G., Wahl, K.J.: Accessing Inaccessible Interfaces: In Situ Approaches to Materials Tribology. *MRS Bulletin* **33**(12), 1145-1150 (2008).
6. Felts, J.R., Oyer, A.J., Hernández, S.C., Whitener Jr, K.E., Robinson, J.T., Walton, S.G., Sheehan, P.E.: Direct mechanochemical cleavage of functional groups from graphene. *Nat Commun* **6**, 6467 (2015).
7. Tonck, A., Martin, J.M., Kapsa, P., Georges, J.M.: Boundary lubrication with anti-wear additives: study of interface film formation by electrical contact resistance. *Tribol. Int.* **12**(5), 209-213 (1979).
8. Jiang, J., Stott, F.H., Stack, M.M.: Some frictional features associated with the sliding wear of the nickel-base alloy N80A at temperatures to 250 °C. *Wear* **176**(2), 185-194 (1994).
9. Wahl, K.J., Belin, M., Singer, I.L.: A triboscopic investigation of the wear and friction of MoS<sub>2</sub> in a reciprocating sliding contact. *Wear* **214**(2), 212-220 (1998).
10. Miller, B., Kotvis, P., Furlong, O., Tysoe, W.: Relating Molecular Structure to Tribological Chemistry: Borate Esters on Copper. *Tribology Letters* **49**(1), 21-29 (2013).
11. Mori, S., Morales, W.: Tribological reactions of perfluoroalkyl polyether oils with stainless steel under ultrahigh vacuum conditions at room temperature. *Wear* **132**(1), 111-121 (1989).
12. Minami, I., Kubo, T., Fujiwara, S., Ogasawara, Y., Nanao, H., Mori, S.: Investigation of Tribology chemistry by means of Stable Isotopic Tracers: TOF-SIMS Analysis of Langmuir–Blodgett

- Films and Examination of their Tribological Properties. *Tribology Letters* **20**(3-4), 287-297 (2005).
13. Adams, H.L., Garvey, M.T., Ramasamy, U.S., Ye, Z., Martini, A., Tysoe, W.T.: Shear-Induced Mechanochemistry: Pushing Molecules Around. *The Journal of Physical Chemistry C* **119**(13), 7115-7123 (2015).
  14. Briggs, B., Seah, M.P.: *Practical Surface Analysis: Auger and X-ray Photoelectron Spectroscopy*. John Wiley and Sons, New York (1996)
  15. Reihl, B., Baer, Y., Crescenzi, M.D., Diociaiuti, M., Lozzi, L., Picozzi, P., Santucci, S.: Local structure of graphite by EELFS spectroscopy: Influence of multiple plasmons and orientational dependence. *Surface Science* **189**, 628-635 (1987).
  16. De Crescenzi, M., Piancastelli, M.N.: *Electron scattering and related spectroscopies*. World Scientific, Singapore; River Edge, NJ (1996)
  17. Furlong, O.J., Miller, B.P., Kotvis, P., Tysoe, W.T.: Low-Temperature, Shear-Induced Tribofilm Formation from Dimethyl Disulfide on Copper. *ACS Applied Materials & Interfaces* **3**(3), 795-800 (2011).
  18. Gao, F., Kotvis, P.V., Tysoe, W.T.: The friction, mobility and transfer of tribological films: potassium chloride and ferrous chloride on iron. *Wear* **256**(11-12), 1005-1017 (2004).
  19. Furlong, O., Miller, B., Tysoe, W.T.: Shear-induced boundary film formation from dialkyl sulfides on copper. *Wear* **274–275**(0), 183-187 (2012).
  20. Furlong, O.J., Miller, B.P., Li, Z., Walker, J., Burkholder, L., Tysoe, W.T.: The Surface Chemistry of Dimethyl Disulfide on Copper. *Langmuir* **26**(21), 16375-16380 (2010).

21. Furlong, O.J., Miller, B.P., Tysoe, W.T.: Shear-Induced Surface-to-Bulk Transport at Room Temperature in a Sliding Metal-Metal Interface. *Tribology Letters* **41**(1), 257-261 (2011).
22. Rigney, D.A.: Transfer, mixing and associated chemical and mechanical processes during the sliding of ductile materials. *Wear* **245**(1–2), 1-9 (2000).
23. Karthikeyan, S., Kim, H.J., Rigney, D.A.: Velocity and Strain-Rate Profiles in Materials Subjected to Unlubricated Sliding. *Physical Review Letters* **95**(10), 106001 (2005).
24. Emge, A., Karthikeyan, S., Kim, H.J., Rigney, D.A.: The effect of sliding velocity on the tribological behavior of copper. *Wear* **263**(1–6), 614-618 (2007).
25. Kim, H., Kim, W., Falk, M., Rigney, D.: MD Simulations of Microstructure Evolution during High-Velocity Sliding between Crystalline Materials. *Tribology Letters* **28**(3), 299-306 (2007).
26. Emge, A., Karthikeyan, S., Rigney, D.A.: The effects of sliding velocity and sliding time on nanocrystalline tribolayer development and properties in copper. *Wear* **267**(1–4), 562-567 (2009).
27. Karthikeyan, S., Agrawal, A., Rigney, D.A.: Molecular dynamics simulations of sliding in an Fe–Cu tribopair system. *Wear* **267**(5–8), 1166-1176 (2009).
28. Rigney, D., Karthikeyan, S.: The Evolution of Tribomaterial During Sliding: A Brief Introduction. *Tribology Letters* **39**(1), 3-7 (2010).
29. Furlong, O., Miller, B., Li, Z., Tysoe, W.T.: The surface chemistry of diethyl disulfide on copper. *Surface Science* **605**(5–6), 606-611 (2011).

30. Miller, B., Furlong, O., Tysoe, W.: The Kinetics of Shear-Induced Boundary Film Formation from Dimethyl Disulfide on Copper. *Tribology Letters* **49**(1), 39-46 (2013).
31. Fu, X.-Y., Rigney, D.A., Falk, M.L.: Sliding and deformation of metallic glass: experiments and MD simulations. *Journal of Non-Crystalline Solids* **317**(1–2), 206-214 (2003).
32. Kim, H.J., Karthikeyan, S., Rigney, D.: A simulation study of the mixing, atomic flow and velocity profiles of crystalline materials during sliding. *Wear* **267**(5–8), 1130-1136
33. Cumpson, P.J.: Angle-resolved XPS and AES: Depth-resolution limits and a general comparison of properties of depth-profile reconstruction methods. *Journal of Electron Spectroscopy and Related Phenomena* **73**(1), 25-52 (1995).

# Chapter 6

## In-Situ and Ex-Situ Analysis of a Multi-Step Tribochemical Reaction

### ***6.1 Introduction***

While the notion that mechanical forces can induce chemical reactions has been known for millennia,<sup>1</sup> mechanochemical synthetic strategies have undergone a renaissance over the past decades.<sup>2-15</sup> The majority of the fundamental studies of the way in which an external force can induce or accelerate the rates of chemical reactions have predominantly come from using the exquisite force sensitivity of atomic force microscopy (AFM) to pull single molecules.<sup>16-24</sup> However, most mechanochemical reactions are induced at a sliding interface. Indeed, perhaps the most economically and technologically important mechanochemistry involves the sliding-induced or “tribochemical” reactions of additives in lubricating oils to form a film that reduces friction and/or wear; it has been suggested that about a third of the fuel in automobile engines is wasted in overcoming friction.<sup>25</sup> It has recently become clear that the chemistry of such lubricant additives is often mechanochemically induced.<sup>26-29</sup> Consequently, the work reported here focuses on sliding-induced reactions of adsorbates on planar substrates monitored in ultrahigh vacuum (UHV).<sup>29-34</sup>

This approach has the advantage of being able to study the tribo- or mechanochemistry of well-defined mechanophores under well-controlled conditions, thereby allowing the elementary steps in the mechanochemical reaction to be identified. This strategy is used to study the mechanically induced reaction between dimethyl disulfide (DMDS) and copper to yield gas-phase hydrocarbons to form a copper sulfide film. This can be viewed either as a tribochemical reaction that produces a friction-reducing film, or a model mechano-catalytic reaction in which surface chemistry and mechanical forces combine to induce a catalytic reaction that would not occur in the absence of the external force. While DMDS is not a commercial lubricant, it does have the essential ingredients of these additives since DMDS contains S–S linkages that are commonly found in commercial, sulfur-containing lubricants. The simplicity of the model system enables the elementary steps in the reaction pathway, in particular those that are mechanochemically induced, to be identified. The first of these is the mechanochemically induced decomposition of methyl thiolate ( $\text{CH}_3\text{-S}_{(\text{ads})}$ ) species, that form rapidly from DMDS on copper,<sup>35</sup> to evolve gas-phase hydrocarbons (methane, ethylene and ethane) and deposit sulfur on the surface.<sup>34,36</sup> The second is the transport of adsorbed sulfur into the subsurface region of the copper that regenerates a clean surface.<sup>30</sup>

These steps were established using a combination of in-situ and ex-situ surface analytical techniques, which also allowed the rate constants for the elementary reaction steps to be measured.<sup>30,33,34,36,37</sup> Continually repeating this mechanochemical reaction cycle by pressurizing the sample while rubbing should result in the accumulation of a layer of sulfur in the subsurface region of the copper which provides a friction-reducing tribofilm. It is likely that this model includes, perhaps with some modifications, the essential ingredients of mechanochemical reaction processes in general. However, the connection between the elementary-step reactions described

above and the steady-state behavior has yet to be made; this is the goal of the work described below.

## ***6.2 Experimental Methods***

### **Vacuum System**

Mechanochemical measurements were carried out in a stainless-steel UHV chamber operating at a base pressure of  $\sim 2 \times 10^{-10}$  Torr following bake out, which has been described in detail elsewhere.<sup>60</sup> Briefly, the chamber was equipped with a UHV-compatible tribometer, which simultaneously measures the normal load, lateral force and contact resistance between the tip and substrate. Previous work has demonstrated that the maximum interfacial temperature rise for a copper sample under the experimental conditions used ( $4 \times 10^{-3}$  m/s sliding speed, 0.5 N normal load) is much less than 1 K.<sup>29</sup>

All experiments were carried out by initially rubbing the tribopin (made of tungsten carbide covered by a copper transfer film) of  $1.27 \times 10^{-2}$  m in diameter against the clean copper sample until a constant friction coefficient was obtained, a process that usually required  $\sim 50$  scans. The samples were dosed with DMDS through a leak valve connected to a dosing tube (with an internal diameter of  $4 \times 10^{-3}$  m) directed towards the sample so that the pressure at the sample surface is enhanced compared to the measured background pressure. The chamber was also equipped with a single-pass cylindrical-mirror analyzer (CMA) for Auger analysis, and an argon ion bombardment source for sample cleaning and depth profiling. A high-resolution electron gun with a beam energy of 5 keV, and a channeltron secondary electron detector, were also incorporated into the system. This allowed scanning electron microscopy (SEM) images and Auger profiles of the wear scars to be collected. Finally, the chamber also included a quadrupole mass spectrometer for leak checking, detecting gas-phase products formed during rubbing and for gauging reactant

purity. Detailed measurement procedures are described in greater detail in the Supplemental Information section.

### **XPS Measurements.**

XPS measurements were made by removing the sample from the UHV chamber in a nitrogen-filled glove bag and storing them in a sealed container under nitrogen. Further experimental details are given in the Supplemental Information section.

**Materials.** The copper samples (Alfa Aesar, 99.99% pure, 1 mm thick) were polished to a mirror finish using 1  $\mu\text{m}$  diamond paste and then rinsed with deionized water and ultrasonically degreased in acetone. Once in UHV, the copper foils were cleaned using a standard procedure, which consisted of argon ion bombardment ( $\sim 1$  kV,  $\sim 2$   $\mu\text{A}/\text{cm}^2$ ) and annealing cycles up to  $\sim 600$  K. The cleanliness of the samples was monitored using Auger spectroscopy.

The dimethyl disulfide (DMDS, Aldrich, 99.0% purity) and diethyl disulfide (DEDS, Aldrich, 99.0% purity) were transferred to glass bottles and attached to the gas-handling systems of the vacuum chamber, where they were subjected to several freeze-pump-thaw cycles. The purity of the compounds was monitored using mass spectroscopy.

## 6.3 Results

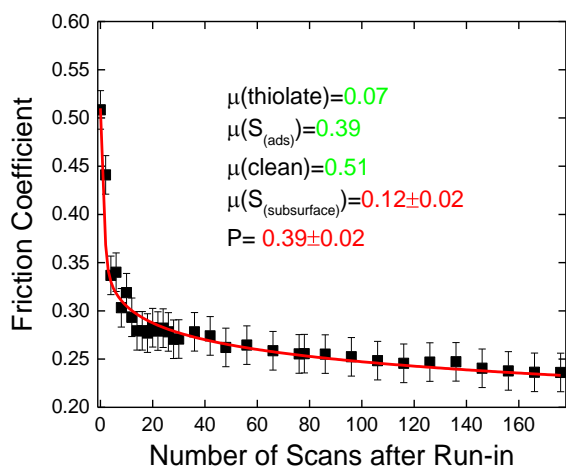


**Figure 6-1 Plot of friction coefficient as a function of the number of passes for the sliding of a copper-covered tungsten carbide ball sliding against copper after the completion of a run-in period (for ~70 scans) and then exposing the surface to a background pressure of  $5 \times 10^{-8}$  Torr of dimethyl disulfide using a normal load of 0.44 N with a sliding speed of 4 mm/s.**

resulting in the generation of vacant sites on the surface. It is proposed that the formation of new sites will allow the mechanochemical reaction cycle to proceed. The ideas are tested in the following to explore whether the elementary reaction steps and their kinetics measured for the monolayer can completely reproduce the steady-state mechanochemical reaction kinetics. This is investigated by performing a mechanochemical reaction between DMDS and copper in UHV by pressurizing the UHV chamber with DMDS while repeatedly rubbing the sample. The reaction is monitored in situ by measuring the evolution in friction force. The experiments are supplemented by in-situ Auger spectroscopy measurements of the total amount of accumulated subsurface sulfur. Angle-resolved X-ray photoelectron spectroscopy (XPS) provides chemical information on sulfur and copper in the tribofilm and allows measurements of the sulfur in-depth distribution.

The elementary steps in the mechanochemical reaction between DMDS and copper and their kinetics have been measured using surface science experiments on adsorbed over layers in UHV.<sup>32</sup> Sliding induces the decomposition of adsorbed methyl thiolate species at room temperature,<sup>29,31</sup> similar to the thermal reaction occurring at higher temperatures ( $\sim 450$  K).<sup>35</sup>

Shear also causes the resulting adsorbed sulfur to penetrate the bulk of the sample,<sup>30,31</sup> in a mechanism proposed to occur by the formation of Kelvin-Helmholtz instabilities,<sup>38-44</sup> thus

The experiment was carried out as follows. First the clean copper sample was rubbed until the friction coefficient ( $\mu$ , the ratio of the lateral force to the normal force) reached a constant value. The experiment was performed by bringing the pin out of contact, moving to the starting position, and by bringing the tip into contact once again between each scan. This protocol was adopted to ensure that identical normal forces were used for each scan and each approach-scan-retract cycle took approximately 15-20 s. Once a steady-state friction coefficient had been obtained after ~50 to 70 scans to create an initial wear track ~100  $\mu\text{m}$  wide, the chamber was pressurized with  $5 \times 10^{-8}$  Torr of DMDS (where the chamber pressure was not corrected for the ionization gauge sensitivity) while rubbing was continued and the friction coefficient continually monitored using the same protocol as described above. The resulting evolution in friction coefficient as a function of the number of scans, after completion of the run-in period on the clean surface, following which the sample was exposed to DMDS, is shown in Figure 1. Note that the friction variation during the initial run-in period is not shown in this figure, and the first scan corresponds to the time at which the chamber was pressurized. Here the friction coefficient initially decreases rapidly for ~10 scans and then shows a much slower decrease as rubbing continues. The line is a fit to the experimental data that will be discussed in greater detail below.

## Measurement of Total Subsurface Sulfur.

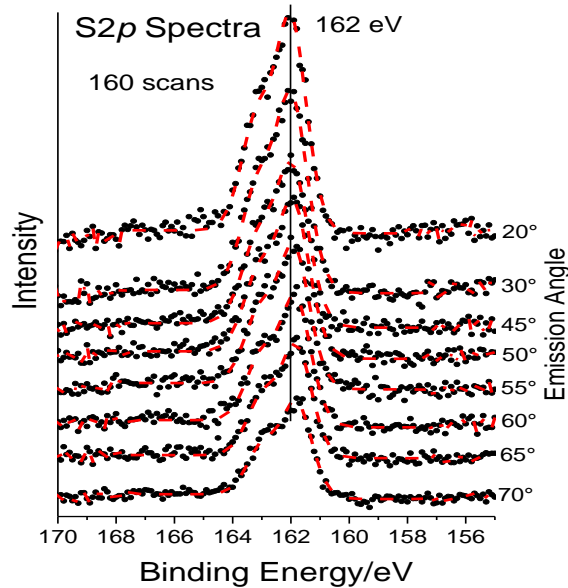


*Figure 6-3 A series of small-spot-size S 2p angle-resolved XPS spectra inside the wear track after rubbing a clean copper sample after the completion of a run-in period in the presence of a background pressure of  $5 \times 10^{-8}$  Torr of dimethyl disulfide for 160 scans at a load of 0.44 N and a sliding speed of 4 mm/s. The spectra were collected at various take-of angles, indicated adjacent to the corresponding spectrum.*

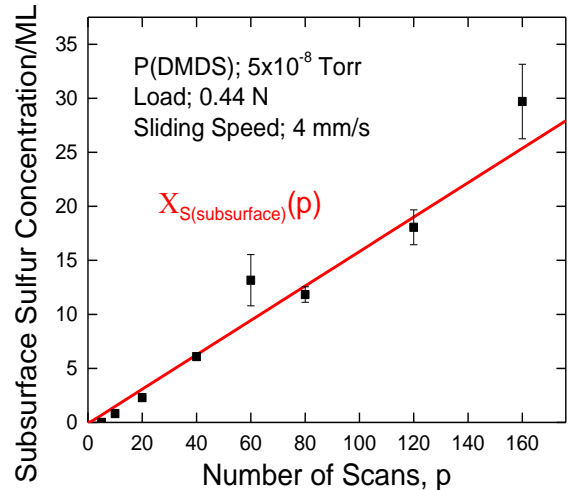


*Figure 6-2 A series of small-spot-size S 2p angle-resolved XPS spectra inside the wear track after rubbing a clean copper sample after the completion of a run-in period in the presence of a background pressure of  $5 \times 10^{-8}$  Torr of dimethyl disulfide for 160 scans at a load of 0.44 N and a sliding speed of 4 mm/s. The spectra were collected at various take-of angles, indicated adjacent to the corresponding spectrum.*

The elementary reaction steps proposed above include the transport of adsorbed sulfur into the subsurface region of the copper. Accordingly, continuously rubbing the copper sample in the presence of a background pressure of DMDS should result in the accumulation of sulfur in of the copper substrate. The total amount of sulfur that has penetrated the bulk can be measured by taking advantage of the observation that subsurface sulfur is thermodynamically less stable than sulfur adsorbed on the copper surface so that heating the sample will cause bulk sulfur to segregate to the surface.<sup>37</sup> However, since the surface is also covered by sulfur and methyl thiolate species, it is carefully titrated by Argon ion

bombardment ( $\sim 120$  s with a beam energy of 3 keV,  $1 \mu\text{A}/\text{cm}^2$ ), where the point at which the surface sulfur had been completely removed was monitored using Auger spectroscopy.<sup>37</sup>

The sample was then heated to  $\sim 600$  K to cause the subsurface sulfur to diffuse to the surface once again and the total amount of segregated surface sulfur was measured using Auger spectroscopy. The experimental results are shown in Figure 2 (■), where the line is a theoretical prediction based on a kinetic model described in the Discussion section.

### Angle-Resolved Electron Spectroscopy Analyses of Subsurface Sulfur.

In order to identify the chemical state of the subsurface sulfur, the rubbed region (the wear track) was analyzed by angle-resolved XPS after transfer ring the sample from the

UHV chamber in a glove bag to the XPS chamber, and then by removing any contaminant layer by Argon ion bombardment (Beam energy, 1 keV, Area,  $3 \times 3 \text{ mm}^2$ ; 42 s). The resulting S 2p XPS spectra as a function of emission-angle, measured with respect to the surface, are shown in Figure 3 for a region of a sample that had been rubbed 160 times in a background of  $5 \times 10^{-8}$  Torr of

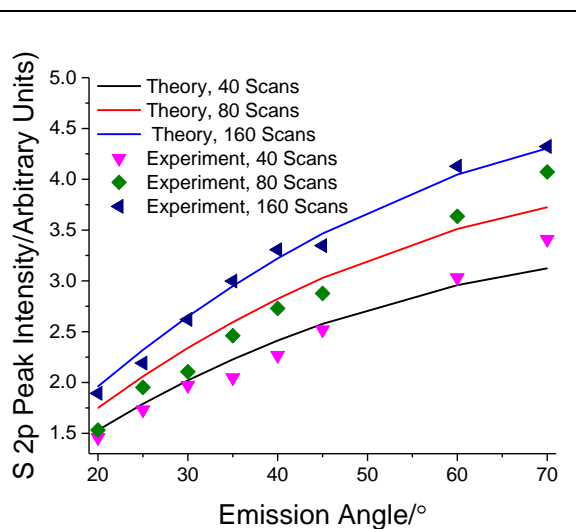


*Figure 6-4 Plot of the integrated area of the S 2p XPS feature, taken from the data shown in Figure 3 as a function of emission angle measured with respect to the surface for a sample that had been rubbed 40 (▼), 80 (◆) and 160 (▲) times in  $5 \times 10^{-8}$  Torr of DMDS with a load on 0.44 N at 4 mm/s. The lines represent calculated variations in S 2p intensity as a function of detection angle after rubbing as discussed in the text.*

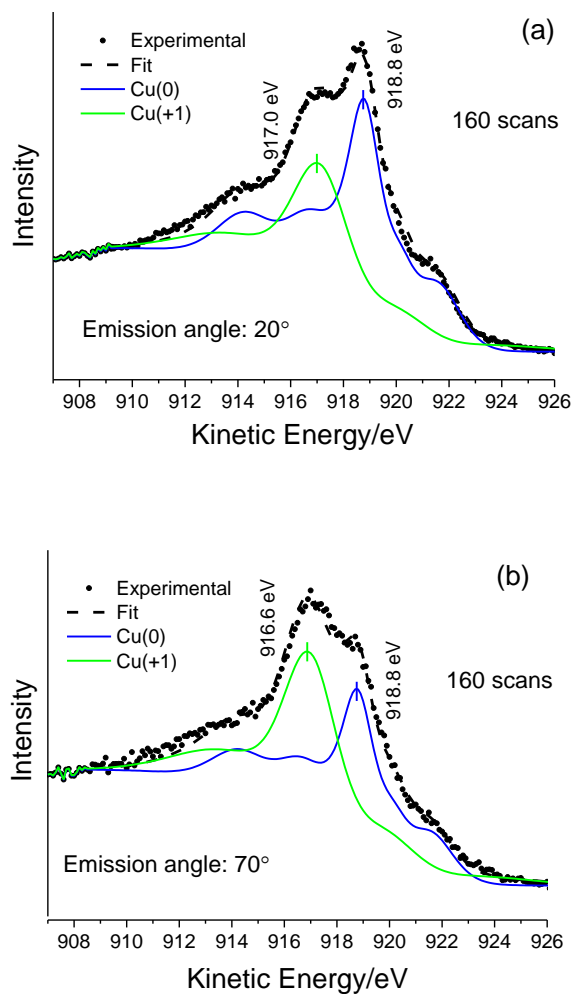


**Figure 6-5** *Cu KLL Auger spectra obtained within the rubbed region for a sample that had been rubbed for 160 scans in  $5 \times 10^{-8}$  Torr of DMDS and then ion bombarded for 42 s to remove the contaminant layer, collected at detection angles of (a)  $20^\circ$  and (b)  $70^\circ$  with respect to the surface. Shown also are fitted Auger profiles.*

DMDS. Corresponding spectra for samples that had been rubbed 40 and 80 were similarly analyzed. While the integrated intensities of the S  $2p$  features vary as a function of take-off angle, the peak position remains constant with a S  $2p_{3/2}$  binding energy of  $162.0 \pm 0.1$  eV, indicating that the chemical state of the sulfur does not vary as a function of depth into the sample. The depth distribution can be obtained from the variation in intensity of the XPS signals as a function of angle using the maximum entropy method.<sup>45</sup> The variation in integrated intensities of the S  $2p$  features are plotted in Figure 4 as a function of detection angle. Note that the lines shown in Figure 4 are the results of predictions from the theoretical model discussed below.

The Cu  $2p_{3/2}$  signal is detected at  $\sim 932.6$  eV but it is not possible to distinguish between metallic Cu and  $\text{Cu}_2\text{S}$ , since the binding energies for copper are not sufficiently different to

distinguish them. The use of the Cu LMM Auger signal has been exploited to distinguish the various chemical states.<sup>46-48</sup> Figure 5 displays an example of the Cu LMM Auger signals after a

curve fitting procedure showing contributions to the Auger signal collected at 20° (Figure 5(a)) and 70° (Figure 5(b)) obtained after 160 rubbing cycles.

Metallic copper is in blue: its intensity decreases with detection angle in agreement with the expected trend since the higher the emission angle, the lower is the sampling depth. An additional profile is fitted using the components of cuprous sulfide but by allowing the peak positions to vary slightly. The most intense peak for the metallic copper component ( $\text{CuL}_3\text{M}_{45}\text{M}_{45} \text{ }^1\text{G}$ ) is found at 918.6 eV, (<sup>48</sup> and references therein) while the additional signal has the most intense peak at  $917.1 \pm 0.1$  eV kinetic energy. For reference, the main Auger feature for  $\text{Cu}_2\text{O}$  is found at  $916.8 \pm 0.1$  eV, <sup>48</sup>  $\text{Cu}_2\text{S}$  at 917.4,<sup>49</sup> and  $\text{CuO}$  at  $917.8 \pm 0.1$  eV <sup>48</sup> kinetic energies.

## ***6.4 Discussion***

**Kinetic Analysis of Mechanochemical Reaction using first-order processes.** The elementary steps and their rate constants for the mechanochemical reaction of DMDS with copper have been obtained from studies of adsorbed monolayers of methyl thiolate species on copper.<sup>34</sup> The reaction sequence is depicted in the Graphical Abstract. Sliding causes the methyl thiolate species to decompose by S–C bond cleavage to desorb small  $\text{C}_1$  and  $\text{C}_2$  hydrocarbons to remove essentially all the carbon and deposit sulfur on the surface.<sup>31-33,37</sup> Shear causes the resulting adsorbed sulfur to penetrate the bulk of the sample,<sup>30</sup> in a mechanism proposed to occur by the formation of Kelvin-Helmholtz instabilities at the sliding surface.<sup>38-44</sup> This produces a clean copper surface that can be repopulated with methyl thiolate species once again, resulting in a mechanochemical reaction cycle to form a sulfur-containing tribofilm. Figure 1 shows that this film can effectively lower friction,<sup>31</sup> where the changes that occur over a large number of passes indicate that a continuous reaction is taking place. The key goal is therefore to establish whether

these elementary-step reactions and their rates measured by surface-science techniques can be used to model the overall mechanochemical reaction process.

The load (0.44 N) and sliding speed (4 mm/s) for the experiments were selected to be identical to those used to measure rate constants,  $k_1$  and  $k_2$ , for thiolate decomposition and shear-induced surface-to-bulk transport. Note that, in the absence of sliding, the rate constants for both processes are negligible; their rates are both mechanochemically accelerated. For a first-order reaction, a time dependence for the mechanochemical acceleration of the reaction the time per pass over a point on the surface is must be defined,  $t_c$ . The kinetic equations can then be written as a function of the number of passes over the surface  $p$  where the reaction time  $t$  is given by  $t = t_c p$ . Since both the normal load and the sliding speed were kept constant,  $t_c$  remains constant for each experiment.

The rate constant for methyl thiolate decomposition,  $k_1 t_c = k'_1 = 0.63 \pm 0.03$ ,<sup>29</sup> and the first-order rate constant for the surface-to-bulk-transport of sulfur  $k_2 t_c = k'_2 = 2.5 \pm 0.5$ .<sup>34</sup> As a consequence of  $k_2 > k_1$ , the sulfur formed by thiolate decomposition is quite rapidly transported into the bulk.

In order to perform this analysis, it is assumed that, if there are several reactants, intermediates and products on the surface, and if the  $i^{\text{th}}$  component has a relative, time-dependent coverage  $\Theta_i(t)$ , with an associated characteristic friction coefficient  $\mu_i$ , then the time evolution of the friction coefficient  $\mu(t)$  can be written as<sup>34</sup>:

$$\mu(t) = \sum_i \mu_i \Theta_i(t) \quad (1).$$

The resulting characteristic friction coefficients for a methyl thiolate-covered ( $\mu_{th}$ ), sulfur-covered ( $\mu_S$ ) and a clean surface ( $\mu_{clean}$ ), were  $\mu_{th} = 0.07 \pm 0.02$ ,  $\mu_S = 0.39 \pm 0.06$ , and  $\mu_{clean} = 0.51 \pm 0.05$ . Consequently, most of the parameters needed to model the mechanochemical reaction

between copper and DMDS have already been determined, except for the characteristic friction coefficient of copper containing subsurface sulfur,  $\mu_{S(subsurface)}$ , which will be used as an adjustable parameter.

To model the continuous mechanochemical reaction, it is assumed that DMDS initially reacts with copper to produce a methyl thiolate coverage,  $\Theta_{th}^0$ , where coverages are defined as the number of adsorbates per surface copper atom ratioed to the maximum number of adsorbates that can be accommodated per surface copper atom, so that  $0 \leq \Theta \leq 1$ . To calculate the coverage of methyl thiolate species that adsorb on the surface between each pass, the thiolate coverage in a previously rubbed portion of a copper sample was measured as a function of DMDS exposure measured in Langmuirs (1 Langmuir (L) =  $1 \times 10^{-6}$  Torr s), using the peak-to-peak intensity of the S LMM Auger signal.

The mechanochemical reaction in a background of DMDS is modelled as follows. For the first pass over the surface, following adsorption of an initial methyl thiolate coverage  $\Theta_{th}^0$ , then (i) the proportion of thiolate species that decomposes to give adsorbed sulfur and evolve gas-phase hydrocarbons is calculated to give  $\Theta_{th}(p)$  for  $p = 1$  using the previously measured value of  $k'_1$ , (ii) the resulting sulfur coverage  $\Theta_S(p)$  is calculated by assuming that each decomposing methyl thiolate species gives an adsorbed sulfur atom and, finally (iii) the amount of sulfur that is transported into the subsurface region  $\Theta_{S(subsurface)}(p)$  is obtained. In the mechanochemical reaction, the pins slides for  $\sim 1$ s. The tip then comes out of contact, moves to the beginning of the rubbed region, and approaches the surface once again. This process typically takes  $\sim 15$  to 20 seconds. During this period, a proportion  $P$  of the remaining clean copper surface (with coverage  $\Theta_{clean}$ ) becomes covered by methyl thiolate species due to reaction with gas-phase DMDS, thus adding to any methyl thiolate species already on the

surface.  $P$  should be in the range of  $\sim 0.4$  to  $\sim 0.5$ . This defines the initial conditions for the second pass ( $p = 2$ ), and the extent of reaction of the various adsorbates is calculated once again. The cycle is again repeated by occupying a proportion  $P$  of the vacant sites and recalculating the extent to which each of the surface components has reacted as a function of the number of passes  $p$ , to yield values of

$\Theta_{S(subsurface)}(p)$ ,  $\Theta_{th}(p)$ ,  $\Theta_S(p)$  and  $\Theta_{clean}(p)$ . Note that, because of the definition of coverage above,  $\Theta_{th}(p) + \Theta_S(p) + \Theta_{clean}(p) + \Theta_{S(subsurface)}(p) = 1$ , which is used to obtain the clean surface coverage (or proportion or vacant sites).

The friction coefficient  $\mu(p)$  is calculated from Eqn. 1 as:

$$\mu(p) = \mu_{th}\Theta_{th}(p) + \mu_S\Theta_S(p) + \mu_{clean}\Theta_{clean}(p) + \mu_{S(subsurface)}\Theta_{S(subsurface)}(p) \quad (2).$$

The results are compared with the experimental measurements to obtain best-fit values of  $\Theta_{th}^0$ ,  $P$  and  $\mu_{S(subsurface)}$ . It is expected that surface composition will evolve to some steady-state condition in which the mechanochemical reduction in thiolate coverage is balanced by the amount of methyl thiolate species formed by DMDS reaction with the copper surface between each pass. The kinetics model is described in greater detail in the Supporting Information section.

Since the rate constant  $k'_1$  and  $k'_2$  have been determined previously,<sup>34</sup> the only two unknown kinetic parameters that determine the surface composition are  $\Theta_{th}^0$  and  $P$ . Changes in the value of

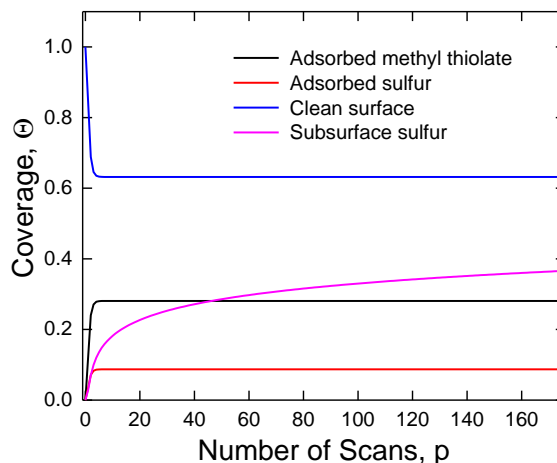


**Figure 6-6** Plots of the calculated coverages of adsorbed methyl thiolate, sulfur, the clean surface and subsurface sulfur as a function of the number of passes using parameters that gave the best fit to the friction data (Figure 1).

$\Theta_{th}^0$  will predominantly influence the behavior during the first few scans and the subsequent evolution of the surface depends only on the value of  $P$ .

The kinetic model is tested by calculating the friction coefficient as a function of the number of passes  $\mu(p)$  by varying  $\Theta_{th}^0$  and  $P$  and fitting to the experimental results in Figure 1 using previously determined values of  $\mu_{th}$ ,  $\mu_S$  and  $\mu_{clean}$ ,<sup>34</sup> so that only the value of  $\mu_{S(subsurface)}$  is adjusted. The resulting fit is shown as a solid line plotted with the experimental data in Figure 1, where the agreement between theory and experiment is excellent. The values used to obtain the best fit were  $P = 0.39 \pm 0.02$ ,  $\Theta_{th}^0 = 0.23 \pm 0.021$  and  $\mu_{S(sub)} = 0.12 \pm 0.02$ , where the value of  $P$  is within the expected range.

The evolution in the composition of the interface as a function of number of passes during gas-phase lubrication by DMDS is shown in Figure 6. This reveals that the surface composition varies during the first few scans but rapidly reaches a steady state. At the same time, the subsurface sulfur coverage increases. As sliding continues, shear causes the subsurface sulfur to penetrate further into the bulk of the sample so that sulfur continues to accumulate in the copper. These observations rationalize the evolution in friction coefficient with the number of passes (Figure 1). Here the rapid initial decrease in friction coefficient is associated with the adsorption of methyl thiolate species on the copper surface. Subsurface sulfur then starts to accumulate, giving rise to the continued steady decrease in friction coefficient.

**Subsurface Sulfur Concentration and Distribution.** A direct test of the validity of the kinetic model comes from measuring the total amount of subsurface sulfur that builds up as scanning proceeds. The results are plotted in Figure 2 (■). The experimental results are

compared with the prediction of the model and are shown as a solid line in Figure 2, where the agreement is excellent, providing additional validation of the model.

To further test the model, the theoretically predicted subsurface sulfur distribution is compared with the angle-resolved XPS results.

Based on analyses of the kinetics of the mechanically induced removal of an adsorbed sulfur over layer<sup>30</sup> using a model proposed by Rigney,<sup>39</sup> it is assumed that the sulfur is transported a distance  $d_p$  into the bulk for each pass of the tribopin over the surface so that a sulfur-covered surface that has been rubbed  $p$  times will penetrate a distance  $z = pd_p$  into the sample. If the initial sulfur overlayer thickness is  $d_0$ , then the subsurface sulfur concentration  $C_S(p, z')$ , is given

$$C_S(p, z') = \frac{\theta_s}{(d_p/d_0)} \left( \ln \left( \frac{p}{z'} \right) - \frac{1}{2} \left( \frac{1}{p} - \frac{1}{z'} \right) \right) \quad (3),$$

where  $z' = \frac{z}{d_p}$ . As shown previously,  $\frac{d_p}{d_0} = k'_2$ .<sup>34</sup> The results are plotted in Figure 7 for  $p = 40$  (■), 80 (●) and 160 (▲) passes, where the concentration is plotted in units of monolayers of sulfur (ML), and the depth,  $z$  is ratioed to the electron mean free path  $\lambda$  for S 2p electrons with a kinetic energy of ~1100 eV when using an Al K $\alpha$  source.<sup>50</sup> These results indicate that the sulfur has penetrated a considerable distance into the subsurface region of the copper and is of the order of the mean-free path of the emitted electrons so that angle-resolved XPS provides an ideal, non-destructive means for measuring the depth profile. The variation in the intensity of the S 2p peak was calculated by assuming that the signal originating from some distance  $d$  in the sample at a detection angle  $\Theta$  with respect to the surfaces varies as  $\exp\left(-\frac{d}{\lambda \sin\Theta}\right)$ , where  $\lambda$  is the electron mean-free path. The resulting calculated concentration profiles are shown in Figure 4 after rubbing 40(—), 80 (—) and 160 (—) times. Shown also plotted on this figure are the experimental

data obtained from the spectra shown in Figure 4 for a sample that had been rubbed 40 (▼), 80 (◆) and 160 (▲) times in  $5 \times 10^{-8}$  Torr of DMDS. The agreement between the theory and experiment is excellent.

**Nature of the Subsurface Sulfur.** The S  $2p$  XPS (Figure 3) indicate that the chemical shift, and thus the sulfur oxidation state corresponds to a sulfide ( $S^{2-}$ ) for all detection angles. This implies that the sulfur has the same oxidation state even though the Cu:S stoichiometry varies as a function of depth and the number of times that the surface has been rubbed (Figure 7).

The X-ray-stimulated Auger data (Figure 5) provide some additional information on the

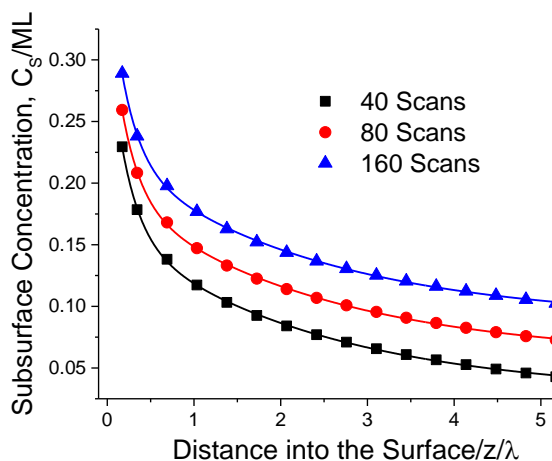


**Figure 6-7** Plot of the subsurface sulfur concentration as a function of the total number of passes, 40 (■), 80 (●) and 160 (▲), where the concentration is plotted in units of monolayers of sulfur (ML), and the depth,  $z$  is ratioed to the electron mean free path  $\lambda$  for S  $2p$  electrons with a kinetic energy of  $\sim 1100$  eV when using an Al  $K\alpha$  source

chemical state of the copper. Metallic copper is clearly evident from the position of the major peak at 918.6 eV KE, and the lower relative intensity of this profile for grazing detection (Figure 5(a)) is in accord with the larger sulfur content near the sample surface (Figure 7). The additional intensity in the Auger spectra gives the best fit to a profile with the main peak centered at  $917 \pm 0.1$  eV KE. Unfortunately, unlike XPS chemical shifts, the position of the main Auger feature does not vary monotonically with copper oxidation state so that, for example, the main peak for  $Cu_2O$  is

found at 916.7 eV,<sup>48</sup>  $Cu_2S$  at 917.4,<sup>49</sup> and  $CuO$  at 918.7 eV KE. This does indicate that a portion

of the copper is oxidized, but has not yet formed a stoichiometric sulfide during the experiments carried out in UHV suggesting the sulphide ions are uniformly distributed throughout the surface region of the copper rather than agglomerating to form regions of stoichiometric sulphides.

The specific friction coefficient of the sample with subsurface sulfur is  $\sim 0.12$ , somewhat higher than the value of friction coefficient for copper lubricated by DMDS dissolved in a poly  $\alpha$ -olefin, where the friction coefficient was  $\sim 0.05$ <sup>31</sup>. In this case, the conditions were more severe than those for the UHV experiments and many result in the formation of a complete cuprous sulfide film. However, the friction coefficient of cuprous sulfide has been found to depend on load and sliding velocity<sup>51</sup>, which may also account for differences between the two experiments.

## ***6.5 Conclusion***

The foregoing analysis demonstrates that the elementary reaction steps in the mechanochemical reaction between DMDS and copper identified by experiments carried out on a methyl thiolate monolayer on copper effectively reproduce the steady-state reaction. This indicates that the two mechanochemical processes, sliding-induced methyl thiolate decomposition and the surface-to-bulk transport of sulfur completely account for the mechanochemical reaction pathway. It is not yet clear if these are all the processes that can occur in mechanochemical reactions. However, they are likely to dominate the mechanochemical effects in tribochemical reactions. However, it should also be pointed out that surface temperature increases due to frictional heating can also accelerate rates of chemical reaction and indeed have been found to dominate film formation processes for lubricants that operate under severe conditions.<sup>52-55</sup>

Such studies will allow the physical origins of these elementary-step mechanochemical processes to be understood. For example, mechanochemical reactions induced by an AFM tip have shown that the reaction rate increases approximately exponentially with shear-stress<sup>26</sup> or

contact pressure.<sup>28</sup> Such an effect is described in the mechanochemistry community by the Bell equation.<sup>56</sup> However, the general physical concepts that describe the way in which an external force accelerates the rate of transition over an energy barrier were first presented at the beginning of the last century by Prandtl<sup>57</sup> and also used by Eyring to model fluid viscosity<sup>58</sup> as well as other mechanically induced processes.<sup>59</sup>

While some sliding-induced tribochemical processes result in a film forming on top of the substrate,<sup>27</sup> the film is formed on copper by a surface-to-bulk transport process. The total amount of sulfur in the bulk as a function of the number of passes (Figure 2) as well as the depth distribution (Figure 4) are reproduced by a model that indicates that the distance that adsorbed sulfur moves into the subsurface region is proportional to the number of passes.<sup>39</sup> This suggests that this mimics processes that cause substrate oxidation and depends primarily on the strain-rate sensitivity of the material.

## 6.6 References

- (1) Theophrastus, H. J. *Theophrastus's history of stones : with an English version, and critical and philosophical notes, including the modern history of the gems, &c., described by that author, and of many other of the native fossils*: London, 1774.
- (2) Sohma, J. Mechanochemistry of polymers. *Progress in Polymer Science* **1989**, *14* (4), 451.
- (3) Boldyrev, V. V.; Tkáčová, K. Mechanochemistry of Solids: Past, Present, and Prospects. *Journal of Materials Synthesis and Processing* **2000**, *8* (3), 121.
- (4) Levitas, V. I. High-pressure mechanochemistry: Conceptual multiscale theory and interpretation of experiments. *Physical Review B* **2004**, *70* (18), 184118.

- (5) Beyer, M. K.; Clausen-Schaumann, H. Mechanochemistry: The Mechanical Activation of Covalent Bonds. *Chemical Reviews* **2005**, *105* (8), 2921.
- (6) Kipp, S.; Šepelák, V.; Becker, K. D. Mechanochemie: Chemie mit dem Hammer. *Chemie in unserer Zeit* **2005**, *39* (6), 384.
- (7) Todres, Z. V. *Organic mechanochemistry and its practical applications*; Taylor&Francis: Boca Raton, FL, 2006.
- (8) Rosen, B. M.; Percec, V. Mechanochemistry: A reaction to stress. *Nature* **2007**, *446* (7134), 381.
- (9) Varma, R. S. “Greener” chemical syntheses using mechanochemical mixing or microwave and ultrasound irradiation. *Green Chemistry Letters and Reviews* **2007**, *1* (1), 37.
- (10) Mitchenko, S. A. Mechanochemistry in heterogeneous catalysis. *Theor Exp Chem* **2007**, *43* (4), 211.
- (11) Ribas-Arino, J.; Shiga, M.; Marx, D. Understanding Covalent Mechanochemistry. *Angewandte Chemie International Edition* **2009**, *48* (23), 4190.
- (12) Craig, S. L. Mechanochemistry: A tour of force. *Nature* **2012**, *487* (7406), 176.
- (13) Bowmaker, G. A. Solvent-assisted mechanochemistry. *Chemical Communications* **2013**, *49* (4), 334.
- (14) Groote, R.; Jakobs, R. T. M.; Sijbesma, R. P. Mechanocatalysis: forcing latent catalysts into action. *Polymer Chemistry* **2013**, *4* (18), 4846.
- (15) Makarov, D. E. Perspective: Mechanochemistry of biological and synthetic molecules. *The Journal of Chemical Physics* **2016**, *144* (3), 030901.
- (16) Urakaev, F. K.; Boldyrev, V. V. Mechanism and kinetics of mechanochemical processes in comminuting devices: 1. Theory. *Powder Technology* **2000**, *107* (1–2), 93.

- (17) Urakaev, F. K.; Boldyrev, V. V. Mechanism and kinetics of mechanochemical processes in comminuting devices: 2. Applications of the theory. Experiment. *Powder Technology* **2000**, *107* (3), 197.
- (18) Duwez, A.-S.; Cuenot, S.; Jerome, C.; Gabriel, S.; Jerome, R.; Rapino, S.; Zerbetto, F. Mechanochemistry: targeted delivery of single molecules. *Nat Nano* **2006**, *1* (2), 122.
- (19) Liang, J.; Fernandez, J. M. Mechanochemistry: One Bond at a Time. *ACS Nano* **2009**, *3* (7), 1628.
- (20) Konôpka, M.; Turanský, R.; Dubecký, M.; Marx, D.; Štich, I. Molecular Mechanochemistry Understood at the Nanoscale: Thiolate Interfaces and Junctions with Copper Surfaces and Clusters. *The Journal of Physical Chemistry C* **2009**, *113* (20), 8878.
- (21) Ribas-Arino, J.; Marx, D. Covalent Mechanochemistry: Theoretical Concepts and Computational Tools with Applications to Molecular Nanomechanics. *Chemical Reviews* **2012**, *112* (10), 5412.
- (22) Klukovich, H. M.; Kouznetsova, T. B.; Kean, Z. S.; Lenhardt, J. M.; Craig, S. L. A backbone lever-arm effect enhances polymer mechanochemistry. *Nat Chem* **2013**, *5* (2), 110.
- (23) Seema, P.; Behler, J.; Marx, D. Force-induced mechanical response of molecule-metal interfaces: molecular nanomechanics of propanethiolate self-assembled monolayers on Au(111). *Physical Chemistry Chemical Physics* **2013**, *15* (38), 16001.
- (24) Konda, S. S. M.; Brantley, J. N.; Varghese, B. T.; Wiggins, K. M.; Bielawski, C. W.; Makarov, D. E. Molecular Catch Bonds and the Anti-Hammond Effect in Polymer Mechanochemistry. *Journal of the American Chemical Society* **2013**, *135* (34), 12722.
- (25) Holmberg, K.; Andersson, P.; Erdemir, A. Global energy consumption due to friction in passenger cars. *Tribol. Int.* **2012**, *47* (0), 221.

- (26) Felts, J. R.; Oyer, A. J.; Hernández, S. C.; Whitener Jr, K. E.; Robinson, J. T.; Walton, S. G.; Sheehan, P. E. Direct mechanochemical cleavage of functional groups from graphene. *Nat Commun* **2015**, *6*.
- (27) Zhang, J.; Spikes, H. On the Mechanism of ZDDP Antiwear Film Formation. *Tribology Letters* **2016**, *63* (2), 1.
- (28) Gosvami, N. N.; Bares, J. A.; Mangolini, F.; Konicek, A. R.; Yablon, D. G.; Carpick, R. W. Mechanisms of antiwear tribofilm growth revealed in situ by single-asperity sliding contacts. *Science* **2015**.
- (29) Adams, H. L.; Garvey, M. T.; Ramasamy, U. S.; Ye, Z.; Martini, A.; Tysoe, W. T. Shear-Induced Mechanochemistry: Pushing Molecules Around. *The Journal of Physical Chemistry C* **2015**, *119* (13), 7115.
- (30) Furlong, O. J.; Miller, B. P.; Tysoe, W. T. Shear-Induced Surface-to-Bulk Transport at Room Temperature in a Sliding Metal-Metal Interface. *Tribology Letters* **2011**, *41* (1), 257.
- (31) Furlong, O. J.; Miller, B. P.; Kotvis, P.; Tysoe, W. T. Low-Temperature, Shear-Induced Tribofilm Formation from Dimethyl Disulfide on Copper. *ACS Applied Materials & Interfaces* **2011**, *3* (3), 795.
- (32) Furlong, O.; Miller, B.; Tysoe, W. T. Shear-induced boundary film formation from dialkyl sulfides on copper. *Wear* **2012**, *274–275* (0), 183.
- (33) Miller, B. P.; Furlong, O. J.; Tysoe, W. T. The Kinetics of Shear-Induced Boundary Film Formation from Dimethyl Disulfide on Copper. *Tribology Letters* **2012**, *Submitted*.
- (34) Adams, H.; Miller, B. P.; Kotvis, P. V.; Furlong, O. J.; Martini, A.; Tysoe, W. T. In Situ Measurements of Boundary Film Formation Pathways and Kinetics: Dimethyl and Diethyl Disulfide on Copper. *Tribology Letters* **2016**, *62* (1), 1.

- (35) Furlong, O. J.; Miller, B. P.; Li, Z.; Walker, J.; Burkholder, L.; Tysoe, W. T. The Surface Chemistry of Dimethyl Disulfide on Copper†. *Langmuir* **2010**, *26* (21), 16375.
- (36) Miller, B.; Furlong, O.; Tysoe, W. The Kinetics of Shear-Induced Boundary Film Formation from Dimethyl Disulfide on Copper. *Tribology Letters* **2013**, *49* (1), 39.
- (37) Furlong, O.; Miller, B.; Tysoe, W. Shear-Induced Surface-to-Bulk Transport at Room Temperature in a Sliding Metal–Metal Interface. *Tribology Letters* **2011**, *41* (1), 257.
- (38) Rigney, D. A. Transfer, mixing and associated chemical and mechanical processes during the sliding of ductile materials. *Wear* **2000**, *245* (1–2), 1.
- (39) Karthikeyan, S.; Kim, H. J.; Rigney, D. A. Velocity and Strain-Rate Profiles in Materials Subjected to Unlubricated Sliding. *Physical Review Letters* **2005**, *95* (10), 106001.
- (40) Emge, A.; Karthikeyan, S.; Kim, H. J.; Rigney, D. A. The effect of sliding velocity on the tribological behavior of copper. *Wear* **2007**, *263* (1–6), 614.
- (41) Kim, H.; Kim, W.; Falk, M.; Rigney, D. MD Simulations of Microstructure Evolution during High-Velocity Sliding between Crystalline Materials. *Tribology Letters* **2007**, *28* (3), 299.
- (42) Emge, A.; Karthikeyan, S.; Rigney, D. A. The effects of sliding velocity and sliding time on nanocrystalline tribolayer development and properties in copper. *Wear* **2009**, *267* (1–4), 562.
- (43) Karthikeyan, S.; Agrawal, A.; Rigney, D. A. Molecular dynamics simulations of sliding in an Fe–Cu tribopair system. *Wear* **2009**, *267* (5–8), 1166.
- (44) Rigney, D.; Karthikeyan, S. The Evolution of Tribomaterial During Sliding: A Brief Introduction. *Tribology Letters* **2010**, *39* (1), 3.
- (45) Scorciapino, M. A.; Navarra, G.; Elsener, B.; Rossi, A. Nondestructive Surface Depth Profiles from Angle-Resolved X-ray Photoelectron Spectroscopy Data Using the Maximum Entropy Method. I. A New Protocol. *The Journal of Physical Chemistry C* **2009**, *113* (51), 21328.

- (46) Castle, J. E. Auger Electron Spectroscopy. *CORROSION TECHNOLOGY -NEW YORK AND BASEL-* **2006**, 22, 39.
- (47) Wagner, C. D.; Muilenberg, G. E. *Handbook of x-ray photoelectron spectroscopy : a reference book of standard data for use in x-ray photoelectron spectroscopy*; Physical Electronics Division, Perkin-Elmer Corp.: Eden Prairie, Minn., 1979.
- (48) Cocco, F.; Elsener, B.; Fantauzzi, M.; Atzei, D.; Rossi, A. Nanosized surface films on brass alloys by XPS and XAES. *RSC Advances* **2016**, 6 (37), 31277.
- (49) Fantauzzi, M.; Atzei, D.; Elsener, B.; Lattanzi, P.; Rossi, A. XPS and XAES analysis of copper, arsenic and sulfur chemical state in enargites. *Surface and Interface Analysis* **2006**, 38 (5), 922.
- (50) Seah, M. P.; Dench, W. A. Quantitative electron spectroscopy of surfaces: A standard data base for electron inelastic mean free paths in solids. *Surface and Interface Analysis* **1979**, 1 (1), 2.
- (51) Varenberg, M.; Ryk, G.; Yakhnis, A.; Kligerman, Y.; Kondekar, N.; McDowell, M. T. Mechano-Chemical Surface Modification with Cu<sub>2</sub>S: Inducing Superior Lubricity. *Tribology Letters* **2016**, 64 (2), 28.
- (52) Kotvis, P. V.; Huezo, L. A.; Tysoe, W. T. Surface Chemistry of Methylene Chloride on Iron - A Model for Chlorinated Hydrocarbon Lubricant Additives. *Langmuir* **1993**, 9 (2), 467.
- (53) Kotvis, P. V.; Tysoe, W. T. Surface chemistry of chlorinated hydrocarbon lubricant additives - Part I: Extreme-pressure tribology. *Tribol. Trans.* **1998**, 41 (1), 117.
- (54) Blunt, T. J.; Kotvis, P. V.; Tysoe, W. T. Surface chemistry of chlorinated hydrocarbon lubricant additives - Part II: Modeling the tribological interface. *Tribol. Trans.* **1998**, 41 (1), 129.
- (55) Blunt, T. J.; Kotvis, P. V.; Tysoe, W. T. Determination of interfacial temperatures under extreme pressure conditions. *Tribology Letters* **1996**, 2 (3), 221.

- (56) Bell, G. Models for the specific adhesion of cells to cells. *Science* **1978**, *200* (4342), 618.
- (57) Prandtl, L. Ein Gedankenmodell zur kinetischen Theorie der festen Körper. *Z. Angew. Math. Mech.* **1928**, *8*, 85.
- (58) Eyring, H. Viscosity, Plasticity, and Diffusion as Examples of Absolute Reaction Rates. *The Journal of Chemical Physics* **1936**, *4* (4), 283.
- (59) Spikes, H.; Tysoe, W. On the Commonality Between Theoretical Models for Fluid and Solid Friction, Wear and Tribochemistry. *Tribology Letters* **2015**, *59* (1), 1.
- (60) Gao, F.; Kotvis, P. V.; Tysoe, W. T. The friction, mobility and transfer of tribological films: potassium chloride and ferrous chloride on iron. *Wear* **2004**, *256* (11-12), 1005.

# Chapter 7

## Ab-Initio Simulations of Change in Activation Energy of Decomposition of Methyl Thiolate with Normal and Shear Force

### *7.1 Introduction*

Metallic friction causes huge energy losses in energy in large vehicles and cars; 28% of the energy used to run large machinery and cars goes to overcoming friction in transmissions and engines or loss from wear.<sup>1-3</sup> The potential to reduce this by developing materials and coatings with low friction and wear is enormous, and a significant amount of work has gone into elucidating the principles of metal-on-metal friction to that end.<sup>4-8,9,10</sup>

Chapter 5 showed that the friction coefficient of methyl thiolate on a copper foil can be described by the specific friction coefficients of the individual components and their relative abundance. It follows that any model for predicting the friction coefficient of a lubricated metal will depend on the specific friction coefficient and abundance of each surface species. It was also observed that the composition of the surface changes with friction-induced mechanochemistry. Therefore, to accurately model friction of lubricants on metals, the rates of reaction need to be accounted for. As of now the rate of reactions induced by sliding, particularly metallic sliding, are not understood on an atomic scale.<sup>6,11-13,14</sup>

Atomistic friction modeling, including bond breaking, has been achieved using molecular dynamics (MD) simulations<sup>15,16 17,18</sup>, but these require very small time-steps to replicate molecular vibrations, and the speeds needed to move several atomic spacings in the simulation time are  $\sim$  m/s, and much larger than to the sliding speeds in the experiment in this dissertation  $4 \times 10^{-3}$  m/s.<sup>7</sup>

In this chapter a quasi-static approach was used to simulate the effect of normal and lateral force on the decomposition of methyl thiolate on Cu (100). Atoms are moved step-wise through a range of positions and the structures are allowed to relax at each position to replicate the slow experimental sliding experiment speeds,  $\sim 10^{-7}$  Å/s. Comparing this to the time scale of atomic vibrations, which are  $\sim 10^{-12}$ /s, the methyl thiolate molecules in the experiments in chapters 4-7 have time to respond to applied force to find the lowest-energy configuration and quasi-static calculations present a reasonable approximation. Climbing Nudged Elastic Band (cNEB) calculations were carried out using a top slab of copper lowered toward a methyl-thiolate covered copper surface. The change in activation energy is found as a function of normal force and the resulting activation barrier are compared to the prediction from extended Bell model theory of mechanical activation. To find the effect of shear on bond strength the methyl thiolate was pulled across a Cu (100) at various changes in angle from the surface normal in directions along and diagonal to the lattice vector.

## ***7.2 Theoretical Methods***

Density functional theory (DFT) calculations were performed with the projector augmented wave method as implemented in the Vienna *ab initio* simulation package, VASP. The exchange-correlation potential was described using the generalized gradient approximation of Perdew, Burke and Ernzerhof.<sup>19</sup> A cutoff of 400 eV was used for the planewave basis set, and the

wavefunctions and electron density were converged to within  $1 \times 10^{-6}$  eV. Geometric relaxations were considered to be converged when the force was less than  $0.03$  eV/Å on all unrestricted atoms.

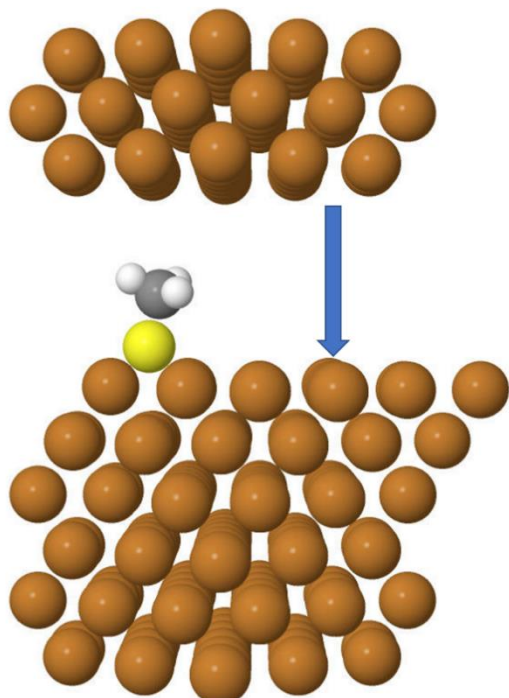


**Figure 7-1 Methyl thiolate on Cu (100) with a top slab of Cu (100) at 8 Å, lowered in 0.2 Angstrom steps**

was sampled with a  $4 \times 4 \times 1$  Monkhorst-Pack grid. The upper slab was lowered in increments of  $0.2$  Å and the system was allowed to relax before moving the slab another step. Incremental lowering was necessary to get reproducible data for each level of compression.

Activation energies were calculated using the climbing nudged elastic band (cNEB) method for the compressed system. The initial and final states from step-wise compression calculations were found and a linear interpolation of the atomic positions was used to determine the initial positions of the cNEB images for the decomposition of methyl thiolate with the top slab eight angstroms above the lower slab. Subsequent NEB calculations performed at distances less

Compression of the cell and climbing nudged elastic band (cNEB) calculations were performed on a  $3 \times 3 \times 6$  Cu slab with the top three layers free to relax and the bottom three layers frozen to mimic the influence of the bulk crystal. A  $3 \times 3 \times 3$  slab of Cu atoms with fixed positions to replicate a thin layer of Cu bound to a WC pin  $8$  Å was added above the bottom slab with a vacuum layer above the upper slab, shown in Figure 1. The k-point mesh and vacuum layer were varied to find a reproducible energy. The first Brillouin zone

than eight angstrom used the positions of the sulfur, carbon, and hydrogen atoms from a converged path as the initial positions for the band images of the next cNEB performed.

Shear and tilt calculations of the methyl thiolate on Cu (100) were performed on a  $4 \times 4 \times 6$  slab of Cu (100) surface which was minimized in energy with respect to lattice constants and vacuum layer. Then a methyl thiolate species was added to the surface in the a four-fold hollow site and relaxed. Finally, the k-point mesh and vacuum layer were varied to find the minimum mesh and gap with reproducible energy. The first Brillouin zone was sampled with a  $2 \times 2 \times 1$  Monkhorst-Pack grid.<sup>20</sup>

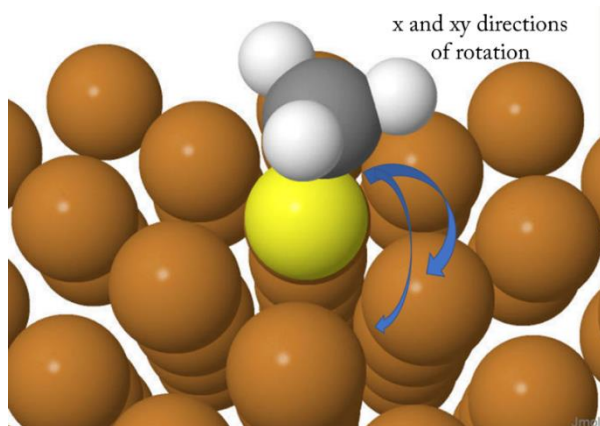


**Figure 7-2** A low ( $\sim 0.125$  ML) coverage methyl thiolate Cu (100) surface. During calculations methyl group is tilted steps of 10 degrees in the direction of and diagonal to the lattice. Directions of tilt are indicated by arrows.

Tilts in the directions along and diagonal to the lattice direction, shown in Figure 1, were performed by tilting the methyl group step-wise around an axis through the sulfur atom in 10-degree increments. Simulations of shear force along and diagonal to the lattice directions were performed step-wise in increments of 0.05 and 0.072 Å respectively. The carbon atom was frozen in the direction of movement and

allowed to relax in other directions. Hydrogen and sulfur atoms were free to relax.

## 7.3 Results and discussion

### Change in Activation Energy with Applied Load

To understand the context of this work it is important to discuss the extended-Bell model for the mechanical activation of bonds, which has been successful in explaining AFM friction<sup>21</sup> and pulling experiments.<sup>22,23</sup> A short explanation is given below.

The Arrhenius equation describes the probability of atoms or molecules overcoming some barrier to react at a given temperature and is given in equation 1:

$$\text{rate constant} = Ae^{-E_a/kT} \quad (1)$$

where the rate constant for the reaction depends on  $A$ , the pre-exponential factor,  $E_a$ , the activation energy,  $k$ , the Boltzmann constant and  $T$ , the absolute temperature.

The Bell model adds a work term to the energy input to account for force moving the reactant toward the transition state, so that when the reactant has moved to the transition state the activation energy goes to zero. This is accomplished by adding a force term,  $F$  and change in position,  $\Delta x$ , to the activation energy to make an effective activation energy,  $E_{eff}$ .

$$E_{eff} = E_a - F\Delta x \quad (2)$$

A second term is added to  $E_{eff}$  to account for the change in the shape of the potential energy of the system under load in the extended Bell model:

$$E_{eff} = E_a - F\Delta x + 1/2\Delta\chi F^2 \quad (3)$$

where  $\Delta x = x_I - x_T$ , where  $x_I$  and  $x_T$  are the curvature of the initial and transition states.

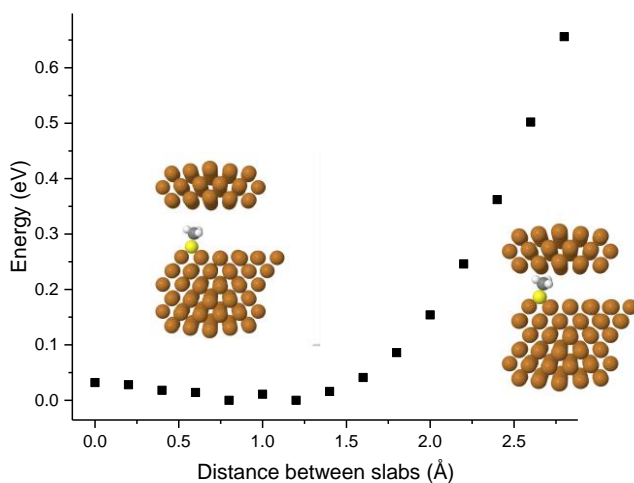


**Figure 7-3 Energy to lower the top copper slab toward the methyl thiolate species on the surface. Insets are beginning and end state of the compression.**

Change in activation energy with normal force was calculated by lowering a top slab to apply force and then performing cNEB calculations. The change in reactant energy is plotted as a function of the distance that the top slab moved, with the zero point being at a separation of eight Å, figure 3, with insets

showing the beginning and end points of compression.

A small attractive force was found between the top slab and the methyl group, giving an interaction energy of ~5 kJ/mol, typical of van der Waals interaction. The force versus distance interaction is dominated by a large repulsive copper-methyl group interaction which supports the normal load, and the rest of the work will concentrate on the repulsive part of the curve.

The evolution in energy profile for the decomposition reaction with reaction coordinate is shown in figure 4, where the legend gives the distances moved by the slab. The activation energy drops with normal load due to an increase in the reactant energy from the repulsive force between the copper and methyl group as mentioned above and a decrease in the energy of the transition state.

The energy to compress the reactant versus the change in slab height from the lowest energy position is shown in figure 5, taken from the data in figure 3. Since the force exerted on

the methyl thiolate species represents the force applied to the system, this energy versus displacement curve can be used to calculate the normal force. From figure 3, there is an initial

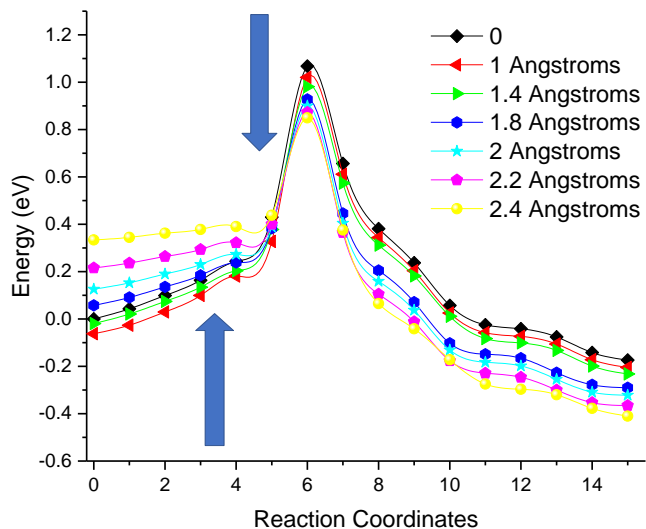


**Figure 7-4** Change in activation energy as the top Cu (100) slab moves toward the bottom Cu (100) slab from the non-interacting distance, were the slab separation is indicated by the color of the line. Arrows highlight the change in energy of reactant and transition state.

attractive interaction, which then becomes repulsive when the distance between the slabs is  $\sim 1.2 \text{ \AA}$ . with only a small variation in the form of a linear term. Accordingly, the data in figure 3 is shifted by  $1.2 \text{ \AA}$  to give zero energy at this position. The line shown through the data is a fit to a harmonic potential,  $E(x) = E_0 + \frac{1}{2} kx^2$ . The fit to the data is good, indicating that the interface deforms elastically and the elastic modulus for compressing the methyl thiolate species by the copper slab is found to be  $0.51 \pm 0.01 \text{ eV/\AA}^2$ . This allows the initial-state energy and the energy at the transition state to be calculated as a function of the normal force acting on a methyl thiolate species.

The evolution in the transition-state structure is shown in figure 6. The structure of the transition state showed changes with proximity of the top slab, increasing the copper-methyl bond length and moving the copper atom below it toward the top slab. The carbon-hydrogen bond angle shifts from  $109^\circ$  to  $117^\circ$ , changing from tetrahedral to a trigonal bipyramidal geometry, indicating a highly attractive interaction. Table 1 gives the change in positions and distance between slabs,

attractive interaction, which then becomes repulsive when the distance between the slabs is  $\sim 1.2 \text{ \AA}$ . with only a small variation in the form of a linear term. Accordingly, the data in figure 3 is shifted by  $1.2 \text{ \AA}$  to give zero energy at this position. The line shown

through the data is a fit to a harmonic potential,  $E(x) = E_0 + \frac{1}{2} kx^2$ . The fit to the

and views of the transition state for slab separations of 8 and 5.6 Å are shown on the left to act as a guide.

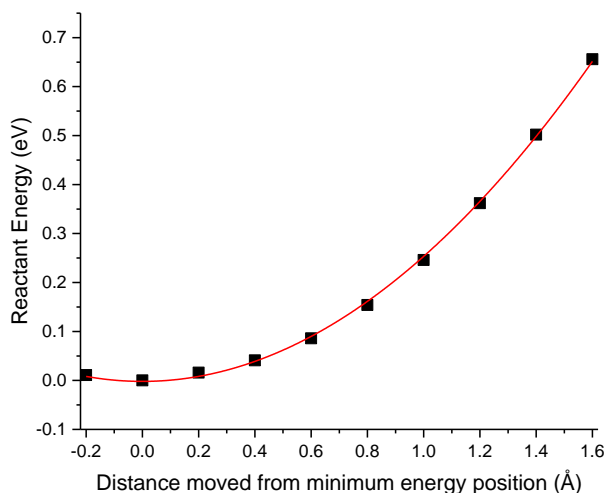
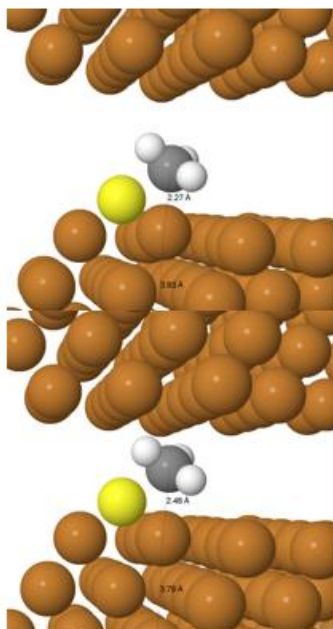


**Figure 7-5 Energy (eV) versus distance upper slab moved (Å) from the minimum energy position. Red line is a quadratic fit to the curves, the elastic modulus is 0.51 eV/Å<sup>2</sup>**

The dramatic change in interaction between the methyl group of the methyl thiolate and the methyl group in the transition state suggests that the bonds of the transition state is dramatically different from the reactant, closer to resembling a methyl radical on an atop site than the methyl thiolate.

The activation energy is calculated from the difference between the energy of the transition



Distance between copper slabs (Å)	Carbon-copper bond length (Å)	Copper movement upward (Å)
8	2.25	0.16
7	2.27	0.2
6.6	2.3	0.24
6.2	2.33	0.27
6	2.37	0.30
5.8	2.43	0.33
5.6	2.48	0.33

**Figure 7-6** Distance between top and bottom slab and change in bond length between methyl group and copper atom, and distance that copper atom moved upward from the lattice position. Transition state of the 8 and 5.6 Angstrom cNEBs are on the left as a guide.

state and the energy of the initial state as a function of normal force and the results are shown in figure 7. The red line is a fit to equation 3, where  $F_{TS}$  and  $k_r$  are the force and spring constant for the transition state and product, respectively, and shows an excellent fit. This yields values of  $\Delta x = 0.15 \pm 0.02 \text{ \AA}$  and  $\Delta\chi = -2.2 \pm 0.06 \text{ eV/\AA}^2$ . The negative value of  $\Delta\chi$  reflects the unusual curvature of the plot of activation energy versus force, which is indicative of an anti-Hammond effect and arises because, in the case of compression, the change in energy of the initial state is larger than the change in energy of the transitions state. This result indicates that a normal force alone acting on a methyl thiolate species should lower the activation energy sufficiently to induce methyl thiolate decomposition at room temperature. The value of  $\Delta x$  implies that the methyl group moves by  $\sim 0.15 \text{ \AA}$  vertically in going from the initial to the transition state structure.

The change in activation energy with distance from the top slab is due to the response of a

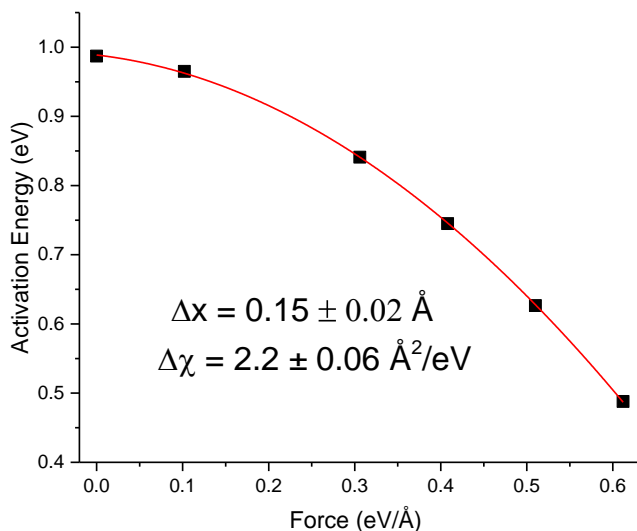


**Figure 7-7** Activation energy in eV versus force,  $F$ , in eV/Å acting on the top slab. The red line is the equation 3 fit and shows good agreement to the data.

mechanically activated reaction that is catalyzed by the proximity of a reactive counter face. A change from a reactant that has a repulsive interaction with the counter face to a transition state that has an attractive interaction means that the force on the reactant cannot

be used to find the change in activation energy with load, as predicted by the extended Bell

model. In this case the change in activation energy with external load is not a function of work being done on the reactant to move it to the transition state but instead arises from the methyl radical of the transition state moving toward a lower energy state by the attraction to the copper of the top slab. This is another difference from the extended Bell model shown in equation 3, and not comparable.

## Response to shear force by translation of the molecule

The friction experiments in the previous chapters have applied both shear and normal force to the surface, and while the effect of normal load applied by a copper slab in the last section has provided some important insights in to the mechanical activation by normal force, the effect of shear force needs to be investigated. To this end, shear on the system via high symmetry paths was

investigated by moving the methyl group of the methyl thiolate in a step-wise fashion along and diagonal to the lattice direction of the Cu (100) surface.

The structures after moving 0.05, 0.1, 0.20, 0.25, 0.4 and 0.5 Å are shown in Figure 9 A-F. The initial response to shear is a tilt of the methyl group around the sulfur atom, then a translation towards and finally over the copper bridge site.

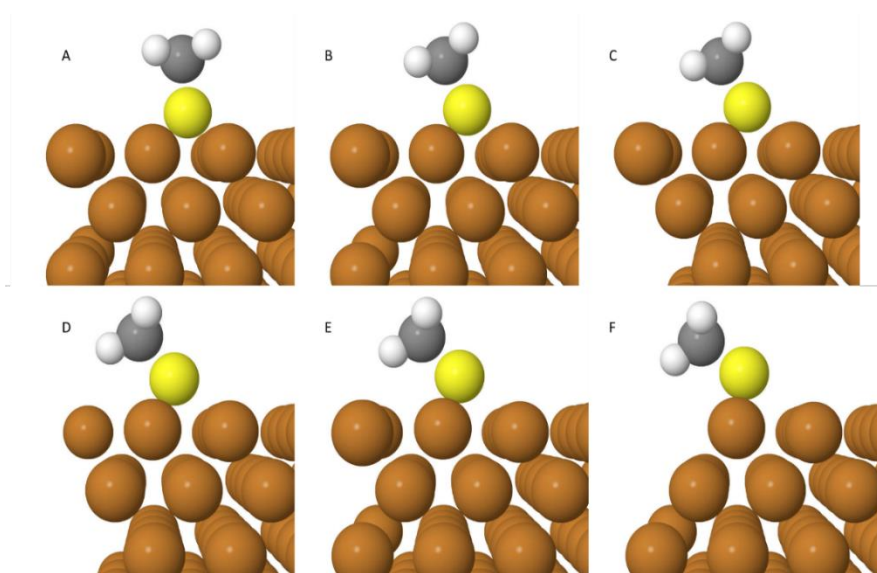


**Figure 7-8 A-F** moving the methyl group 0.05, 0.15, 0.20, 0.25, 0.4, and 0.50 angstroms along the lattice direction. A-C show the copper atoms moving with the sulfur atom and then relaxing back to lattice positions in D. D-F show the methyl thiolate moving over the bridge site.

The movement of the methyl group pulls the copper atoms bonded to the sulfur in the direction of sliding until 0.25 Å when the copper-sulfur bonds break and the copper falls back to lattice positions, visible in figures 8 A-C. Small changes in the carbon-sulfur

sulfur bond length are observed, from 1.85 Å before moving to 1.87 Å in figure 8 C, just before the copper-sulfur bond breaks, then decreasing to 1.83 Å in figure 8 D.

Similar results were found for translating the methyl group diagonal to the lattice direction, with separate bond-breaking events for the first copper-sulfur bond and the subsequent scission of two more copper-sulfur bonds as the methyl thiolate approaches an atop site. Proceeding the step of two copper-sulfur bonds breaking, the carbon-sulfur bond lengthens slightly to 1.88 Å, then

shortens to 1.83 Å thereafter. The relatively small changes in the sulfur-carbon bond with translation of the carbon are likely due to  $\pi^*$  back-bonding interactions between the sulfur and copper, seen by Ohta.<sup>24</sup> Back-donation of charge to the anti-bonding orbitals of the methyl thiolate would result in stronger carbon-sulfur bonds as the sulfur-copper bonds break. This agrees with the work of Konôpka<sup>25,26</sup> in which mechanical bond breaking of the carbon-sulfur bond in methyl thiolate depended on the size of the copper cluster substrate and number of copper-sulfur bonds. As copper atoms were added to the cluster the carbon-sulfur bond became weaker and eventually C-S bond breaking was less energetic than simultaneously breaking three copper-sulfur bonds on Cu (111).

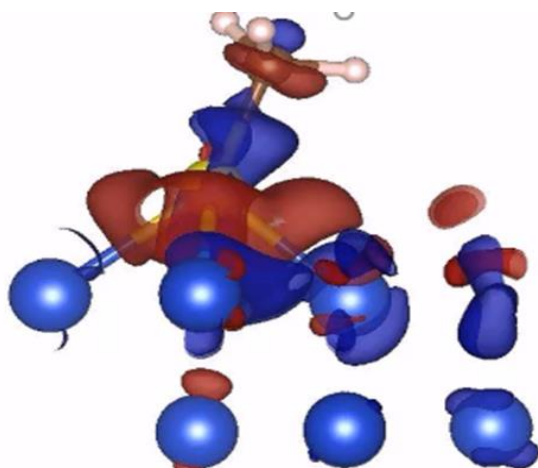


**Figure 7-9** Charge-density difference calculation between the methyl thiolate and copper calculated separately and together. Blue regions indicate a decrease in charge density, red indicates a decrease. The carbon-sulfur bond shows a decrease in charge-density, indicating  $\pi^*$  back bonding, as discussed in the text.

A charge-density difference calculation was done to compare the change in charge when the methyl thiolate was added to the Cu (100) surface, shown in figure 9. Blue regions indicate a decrease in electron density, red ones show an increase. After bonding to the copper surface, the methyl thiolate shows a decrease in charge density between the carbon and sulfur atoms, indicating that the bond is weakened by

the interaction with copper.

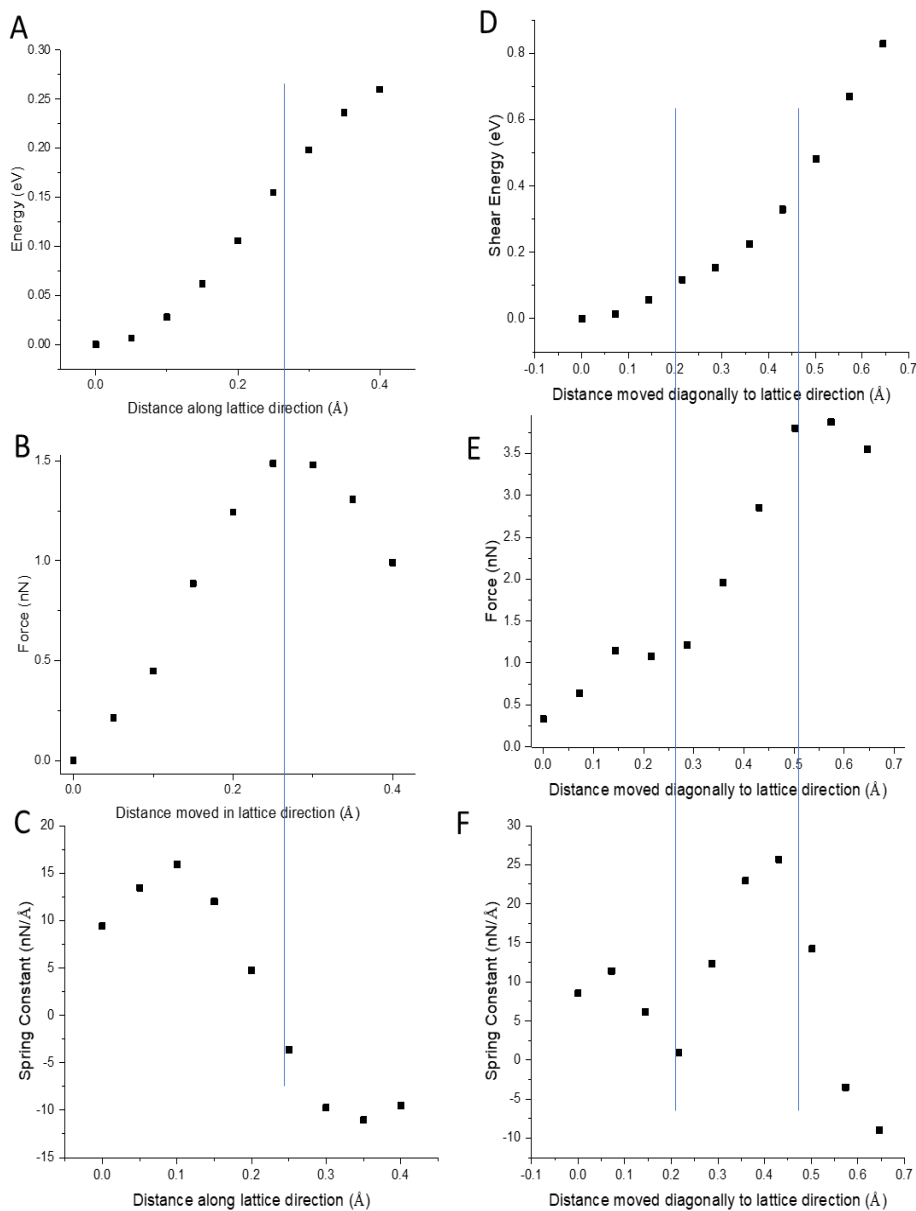


**Figure 7-10** A – C Energy, force, and spring constant for moving the methyl group along the lattice. D-F Energy, force, and spring constant for moving the methyl group diagonally to the lattice. Steps in which one or more copper-sulfur bonds break are marked with a blue line. The inflection points of the energy with distance show bond breaking events.

The inflection points in the energy occur in conjunction with bond-breaking events.

Figure 10 shows the energy, force, and spring constant of translation along and diagonal to the principle lattice direction; blue lines guide the eye to the point where the bond breaks. The mechanically activated bond-breaking of the sulfur-copper bonds has a positive force.

## Tilting methylate – response to load and shear

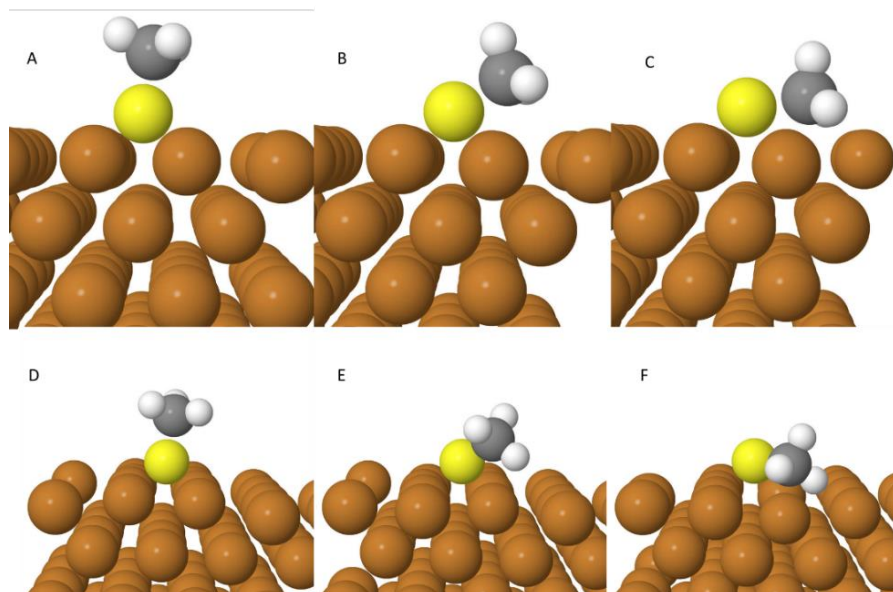


**Figure 7-11 Methyl thiolate tilting by 10, 60, and 90 degrees in the lattice direction and D-F, diagonal to it. Copper atoms in the direction of the tilt are repulsed by the methyl group at higher tilts, moving from their lattice positions**

thiolate tilted toward the bridge (A-C) and atop sites (D-F), resulting in distortion of the copper surface above 60° of tilting. At 60°, a repulsive force begins to push the copper atoms into the

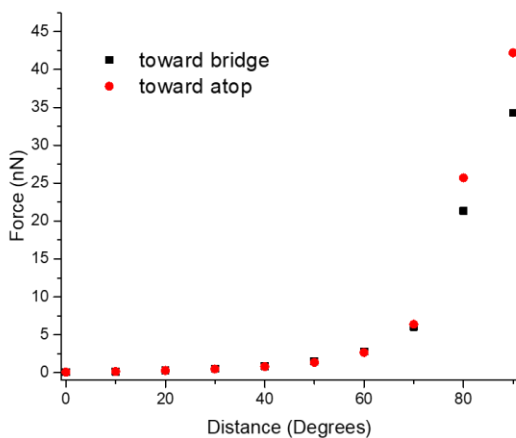


**Figure 7-12 Force to tilt the copper toward bridge (black) or atop (red). The force is low until around 60 degrees, when it increases dramatically due to repulsive force between the methyl group and copper.**

To find the response to load and shear together, first the methyl thiolate was tilted around the sulfur atom in the lattice direction and diagonal to it to find the effect of normal force. Figure 11 shows the methyl

thiolate tilted toward the bridge (A-C) and atop sites (D-F), resulting in distortion of the copper surface above 60° of tilting. At 60°, a repulsive force begins to push the copper atoms into the surface, rather than breaking the carbon-sulfur bond. The copper atoms are constrained by the bulk copper atoms, which therefore not infinitely compressible, that high force may break the carbon-sulfur bond. The force in nN to rotate the bond through various angles is shown in figure 12, and reveals that an initial low tilting force rapidly increases the energy as the methyl group approaches the

copper surface. The tilt toward the bridge and atop sites are nearly isoenergetic until 60°, when the difference in geometry of the methyl group to the copper atoms becomes important.

Next, the tilted species were translated across the surface in the same direction as the tilt. Translating methyl thiolate with low tilt angles followed the same trend as the shear force calculations above. The highly tilted species encounters a more corrugated surface due to the proximity of the methyl group to the copper. Bond-breaking events consisted of sulfur-copper scission, rather than the carbon-sulfur bond cleavage. The energies to translate the tilted species along the lattice direction and diagonal to it are shown in figure 13 A and B, respectively.

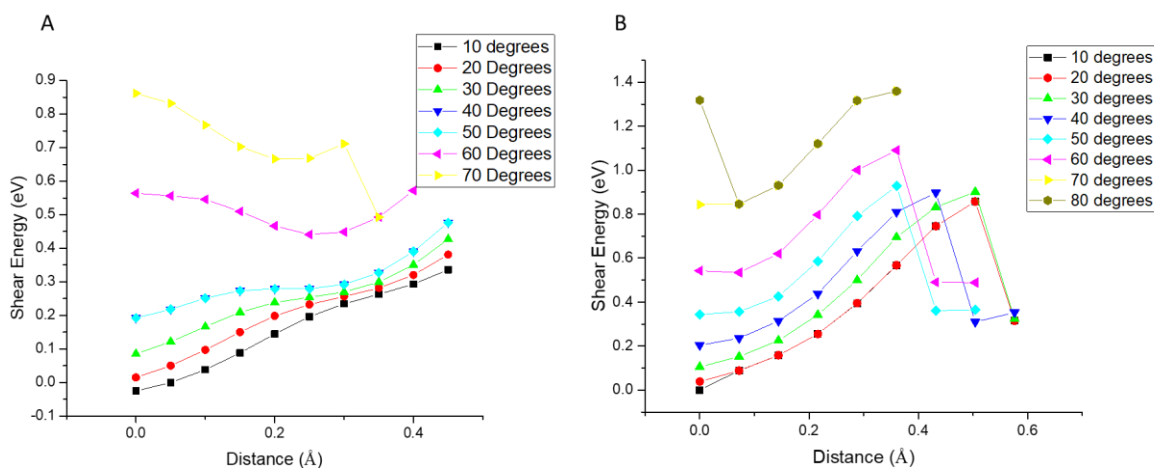


**Figure 7-13** Energy to translate a tilted methyl thiolate over the surface in A) the lattice direction and B) diagonal to it. As the tilt increases the energy of translation increases due to repulsion between the copper and methyl group.

## 7.4 Conclusion

Several important results have been shown in this work. First, an external load applied by a copper surface can lower the activation energy of decomposition, and follows the extended-Bell model if the change in the reactant and product potential energy shape with force is included.

Second, translating the methyl group across the surface to simulate shear does not break the carbon-sulfur bond, but does break the copper-sulfur bonds. The change in interaction between

copper and sulfur atoms is indicated by the change in copper atom position as it relaxes back to the original lattice positions and the change in the position of inflection points in the energy versus position, plotted in Figure 10.

Third, the sulfur-carbon bond remained nearly constant in length and did not break with force, but successive copper-sulfur bond breaking events were more energetic than the first. The carbon-sulfur bond length remained unchanged while pulling, and this may be partially due to the weakening effect of the carbon-sulfur bond by back bonding into the  $\pi^*$  orbital found by Ohta and Konôpka.<sup>24,26</sup> As the sulfur-copper bond breaks, less electron density is donated to the antibonding orbital of the carbon-sulfur bond, causing the counter-intuitive result of strengthening the bond by pulling it. This idea could be explored in greater detail by electron-density calculations to calculate the change in bond density while pulling.

Last, the methyl group is strongly repelled by the copper which causes a significant distortion of the copper lattice, but leaves the carbon-sulfur bond unchanged. This suggests that, in the decomposition of methyl thiolate on copper by sliding, the sulfur-carbon bond is not broken by the forces exerted by contact with the metal until high load.

## 7.5 References

1. Holmberg, K., Andersson, P. & Erdemir, A. Global energy consumption due to friction in passenger cars. *Tribol. Int.* **47**, 221–234 (2012).
2. Holmberg, K., Andersson, P., Nylund, N.-O., Mäkelä, K. & Erdemir, A. Global energy consumption due to friction in trucks and buses. *Tribol. Int.* **78**, 94–114 (2014).
3. Holmberg, K., Kivikytö-Reponen, P., Härkisaari, P., Valtonen, K. & Erdemir, A. Global energy consumption due to friction and wear in the mining industry. *Tribol. Int.* **115**, 116–139 (2017).
4. Ribas-Arino, J. & Marx, D. Covalent mechanochemistry: theoretical concepts and computational tools with applications to molecular nanomechanics. *Chem. Rev.* **112**, 5412–87 (2012).
5. Makkonen, L. A thermodynamic model of sliding friction. *AIP Adv.* **2**, 12179 (2012).
6. Chirmeisen, S. Principles of atomic friction : from sticking atoms to superlubric sliding. 1383–1404 (2008). doi:10.1098/rsta.2007.2164
7. Braun, O. & Naumovets, a. Nanotribology: Microscopic mechanisms of friction. *Surf. Sci. Rep.* **60**, 79–158 (2006).
8. Wimmer, M. a *et al.* Wear mechanisms in metal-on-metal bearings: the importance of tribochemical reaction layers. *J. Orthop. Res.* **28**, 436–43 (2010).
9. Sawyer, W. G., Argibay, N., Burriss, D. L. & Krick, B. A. Mechanistic Studies in Friction and Wear of Bulk Materials. *Annu. Rev. Mater. Res.* **44**, 395–427 (2014).

10. Argibay, N., Chandross, M., Cheng, S. & Michael, J. R. Linking microstructural evolution and macro-scale friction behavior in metals. *J. Mater. Sci.* **52**, 2780–2799 (2017).
11. Dong, Y., Li, Q. & Martini, A. Molecular dynamics simulation of atomic friction: A review and guide. *J. Vac. Sci. & Technol. A* **31**, 30801 (2013).
12. Vanossi, A., Manini, N., Urbakh, M., Zapperi, S. & Tosatti, E. Colloquium : Modeling friction: From nanoscale to mesoscale. *Rev. Mod. Phys.* **85**, 529–552 (2013).
13. Dienwiebel, M. & Pöhlmann, K. Nanoscale Evolution of Sliding Metal Surfaces During Running-in. *Tribol. Lett.* **27**, 255–260 (2007).
14. Beyer, M. K. & Clausen-Schaumann, H. Mechanochemistry: The Mechanical Activation of Covalent Bonds. *Chem. Rev.* **105**, 2921–2948 (2005).
15. Muser, M. H., Wenning, L. & Robbins, M. O. Simple microscopic theory of Amontons's laws for static friction. *Phys. Rev. Lett.* **86**, 1295–1298 (2001).
16. Martini, A. in *Micro- and Nanoscale Phenomena in Tribology* 189–206 (CRC Press, 2011). doi:10.1201/b11211-9
17. Ye, Z. & Martini, A. Atomic friction at exposed and buried graphite step edges: Experiments and simulations. *Appl. Phys. Lett.* **106**, 231603 (2015).
18. Ye, Z. & Martini, A. Atomistic Simulation of the Load Dependence of Nanoscale Friction on Suspended and Supported Graphene. *Langmuir* **30**, 14707–14711 (2014).
19. Perdew, J. P., Burke, K. & Ernzerhof, M. Generalized Gradient Approximation Made Simple. *Phys. Rev. Lett.* **77**, 3865–3868 (1996).

20. Monkhorst, H. J. & Pack, J. D. Special points for Brillouin-zone integrations. *Phys. Rev. B* **13**, 5188–5192 (1976).
21. Felts, J. R. *et al.* Direct mechanochemical cleavage of functional groups from graphene. *Nat Commun* **6**, (2015).
22. Maitra, A. & Arya, G. Influence of pulling handles and device stiffness in single-molecule force spectroscopy. *Phys. Chem. Chem. Phys.* **13**, 1836–1842 (2011).
23. Konda, S. S. M., Brantley, J. N., Bielawski, C. W. & Makarov, D. E. Chemical reactions modulated by mechanical stress: Extended Bell theory. *J. Chem. Phys.* **135**, 164103–164108 (2011).
24. Kondoh, H. *et al.* Structure of alkanethiolate monolayers on Cu(100): Self-assembly on the four-fold-symmetry surface. *J. Phys. Chem. B* **105**, 12870–12878 (2001).
25. Konôpka, M., Rousseau, R., Štich, I. & Marx, D. Detaching thiolates from copper and gold clusters: Which bonds to break? *J. Am. Chem. Soc.* **126**, 12103–12111 (2004).
26. Konôpka, M., Turanský, R., Dubecký, M., Marx, D. & Štich, I. Molecular mechanochemistry understood at the nanoscale: Thiolate interfaces and junctions with copper surfaces and clusters. *J. Phys. Chem. C* **113**, 8878–8887 (2009).

# Chapter 8

## Response of a Methyl Thiolate-Covered Copper Surface to Change in Normal Force and Sliding Speed

### *8.1 Introduction*

This work explores the relationship between the force, both normal and shear, on the decomposition of methyl thiolate species adsorbed on a copper foil. Interfaces are difficult to study because they are ephemeral by nature with buried, nano-scale effects occurring within macroscale objects.

Particularly, measuring the true contact area of a rough interface is of intense interest to the tribology community because sliding interfaces have been found to be composed of contacting asperities, and consequently the exact contact area is difficult to measure.<sup>1</sup> The decomposition of a marker molecule on the surface can provide useful information about the contact mechanics and surface structure of a contact during rubbing.

In this chapter the nature of the contact is explored, and an initial hypothesis is put forth and a set of experiments is presented as a proof-of-concept to support the hypothesis. A theory has not been developed, and while finding observable phenomena that demonstrate veracity of the hypothesis is possible, it is not within the scope of this project to do so.

## ***8.2 Experimental***

Experiments were carried out in a stainless-steel, UHV chamber operating at a base pressure of  $\sim 2 \times 10^{-10}$  Torr following bake out, which has been described in detail elsewhere<sup>2-4</sup>. The chamber was equipped with a UHV-compatible tribometer in which a pin can be slid against a flat substrate, which simultaneously measures the normal load and lateral force by means of strain gauges. Friction measurements were made using a range of sliding speeds from  $1 \times 10^{-4}$  to  $1 \times 10^{-2}$  m/s. Mass spectrometer measurements of the gas-phase products formed during sliding were made using sliding speeds of between 1 and  $8 \times 10^{-3}$  m/s at a normal load of 0.44 N. The spherically-tipped pin ( $\sim 1.27 \times 10^{-2}$  m diameter) was made from tungsten carbide containing some cobalt binder and could be heated by electron bombardment *in vacuo* to clean it. Adsorbed methyl thiolate species were prepared by dosing dimethyl disulfide (DMDS) through a high-precision leak valve connected to a dosing tube (with an internal diameter of  $4 \times 10^{-3}$  m) directed towards the sample so that the pressure at the sample was enhanced compared to the measured background pressure, which was set at  $2 \times 10^{-8}$  Torr during DMDS dosing (where pressures are not corrected for ionization gauge sensitivity). Experiments were performed by initially rubbing the pin against the clean copper sample ( $\sim 1$  cm  $\times$  1 cm by  $\sim 1$  mm thick) 50 times at  $4 \times 10^{-3}$  m/s and 0.44 N load until a constant friction coefficient was obtained.

The chamber also contained a single-pass, cylindrical-mirror analyzer (CMA) for Auger analysis, and an argon ion bombardment source for sample cleaning and depth profiling. Auger

spectra were collected using an electron beam energy of 3 keV. Finally, the chamber also included a quadrupole mass spectrometer (UTI model 100C) placed in line of sight of and ~10 cm away from the sliding contact. The filament of the mass spectrometer was extensively outgassed prior to any experiments being carried out to minimize the background pressure. The mass spectrometer was interfaced using a LabView program, which controlled the detected mass and monitored the mass spectrometer signal as a function of time. The mass spectrometer was also used for leak checking and for gauging reactant purity. An experiment was carried out by initially saturating the copper foil with DMDS after completion of the initial run-in period on the clean copper sample. The pin then approached the surface until reaching a preset load and was then moved across the surface at a preset sliding speed while simultaneously monitoring the normal load ( $F_N$ ), lateral force ( $F_L$ ), and in some cases the mass spectrometer signal. The normal load remained constant during the scan and the friction coefficient was calculated from  $\mu = \frac{F_L}{F_N}$ .

The copper samples (Alfa Aesar, 99.99% pure, 1 mm thick, hard rolled) were polished to a mirror finish using 1  $\mu\text{m}$  diamond paste and then rinsed with deionized water and cleaned ultrasonically in acetone. Once in UHV, the copper sample was further cleaned using a procedure that consisted of argon ion bombardment ( $\sim 1$  kV,  $\sim 2$   $\mu\text{A}/\text{cm}^2$ ) and flash annealing cycles up to  $\sim 850$  K. The cleanliness of the samples was monitored using Auger spectroscopy and it was found to exhibit rectangular low-energy electron diffraction (LEED) patterns after cleaning and annealing in UHV, indicating that the surface contained well-ordered Cu (100) regions.<sup>21</sup>

The DMDS (Aldrich, 99.0% purity) was transferred to a glass bottle and attached to the gas-handling system of the vacuum chamber, where it was subjected to several freeze-pump-thaw cycles. The purity of the DMDS was monitored using mass spectroscopy.

### 8.3 Results

The friction coefficient of a methyl thiolate covered copper foil was measured as a function of the number of passes for various normal loads. The friction coefficient of the first pass as a function of applied load displayed in Figure 1, and shows that the initial friction coefficient is constant as a function of load, suggesting a plastic contact as in Amonton's law, although it can also indicate elastic asperities. As the number of asperities increase with load, the friction force for each contact remains the same, leading to a friction force that rises linearly with normal force to give a constant friction coefficient. The average coefficient of friction of the methyl thiolate covered surface during first scan,  $0.34 \pm 0.02$ , is considerably lower than that of a surface produced

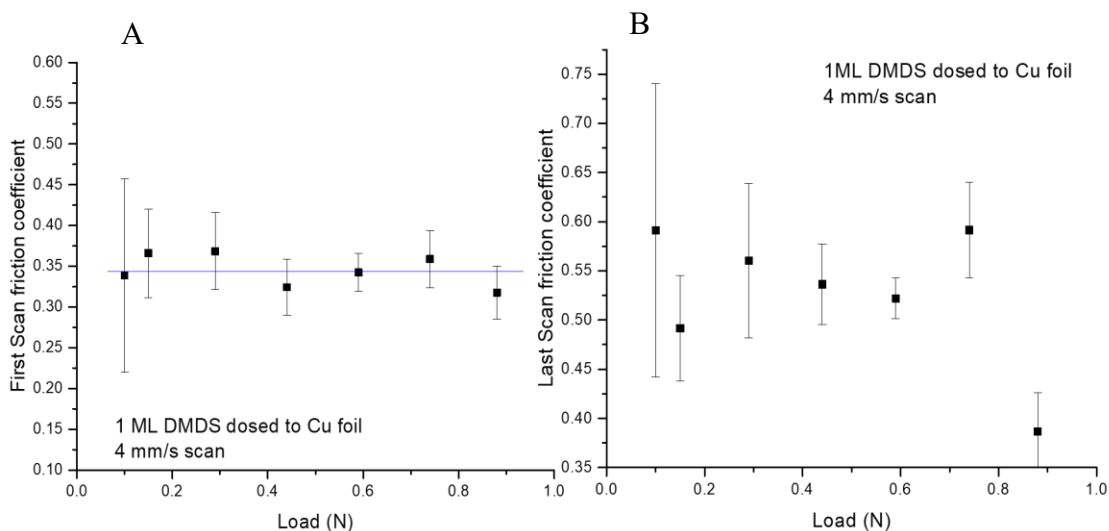


**Figure 8-1 A) Friction coefficients of the first scan of a WC pin across a methyl thiolate covered copper surfaces. Average of the friction coefficient is  $0.34 \pm 0.02$ . B) Friction coefficient of the 15<sup>th</sup> scan shows a wider range, with the 0.88N load value being significantly different from lower loads.**

after 15 scans (Figure 1B) which is  $0.53 \pm 0.3$ .

The surface analysis in Chapter 4 showed that the methyl thiolate species has completely decomposed after 15 scans due to sliding at 0.44 N load so that this represents sliding on the bare

copper surface. Interestingly, the bare copper has a constant friction coefficient over the range of loads tested until 0.88 N, after which it decreases. This indicates that there is some change in the plastic response to pressure of copper that is not present in the thiolate-covered surface.

It has been established that a sliding force can induce the decomposition of methyl thiolate on a copper foil and that the methane and methyl radical production follows an exponential decay

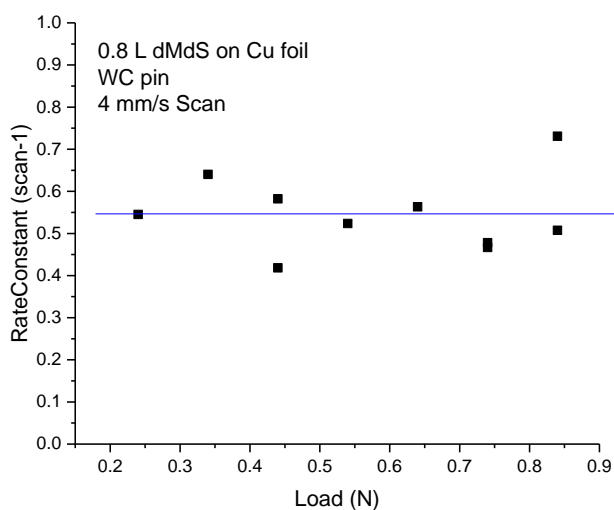


**Figure 8-2 The rate constant for sliding-induced decomposition of methyl thiolate is constant for all loads,  $0.55 \pm 0.09$**

yields an average rate of  $0.55 \pm 0.09$  pass<sup>-1</sup>.

For a force-activated reaction, a constant reaction rate as a function of load is consistent with a plastic contact, that is, one in which the substrate deforms in response to stress, as expected from the friction coefficient data seen earlier. As the force increases, the area of contact increases, and pressure on each molecule is constant, as described by Archard<sup>5</sup> shown in equation 1, where  $A$  is the area of contact,  $W$ , the load, and  $p_m$ , the hardness of the softer of the two materials.

with the number of times that the sample was rubbed, suggestive of first-order kinetics, as discussed in Chapter 4. The rate constant for methyl thiolate decomposition as a function of the number of passes measure from the methane yield, shown in Figure 1, reveals that increasing the normal load does not influence the sliding-induced decomposition rate constant and

$$A = W/p_m \quad (1)$$

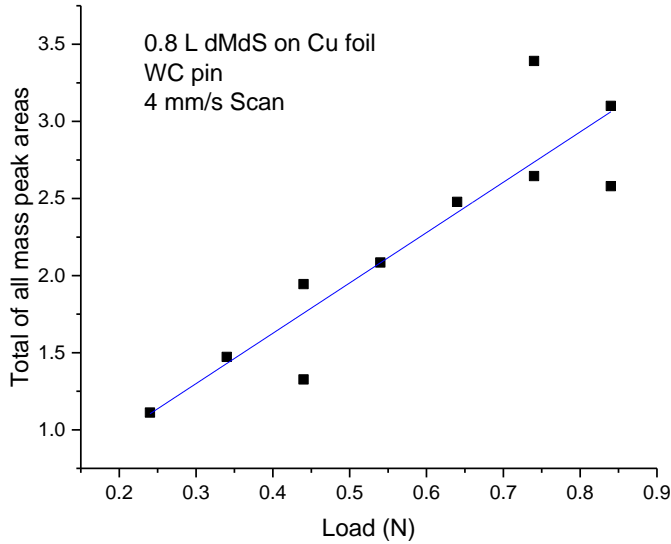


**Figure 8-3 Total of areas for masses, 15,16 ,26 and 30 AMU for first peak of decomposition of methyl thiolate on copper foil rubbed with WC pin. Rate of increase in gas-phase product with load 3.26 +/- 0.53 increase in signal/N**

This predicts a linear increase in product of the decomposition with load, and the relationship is shown in Figure 3. Mass spectrometer signals for 15 (methyl radical a fragment of methane), 16 (methane), 26 (ethyne and a fragment of ethane) and 30 (ethane) AMU were measured while

rubbing at various loads and the total amount of gas-phase product, proportionate to the moles of product by some calibration constant of the mass spectrometer, C, increases linearly by  $3.26 \pm 0.53$  C/N.

Future experiments could be done to exploit this relationship to find the hardness of the surface, which is difficult to measure directly, but necessary for predicting the change in rate with pressure.<sup>6-8</sup> For a monolayer coverage, methyl thiolate on copper has a c (2x2) structure, using the accepted radius of the copper atom as 0.128nm, this corresponds to two methyl thiolates per 1.05 nm<sup>2</sup>. Multiplying the mass spectrometer signal by the calibration constant yields the total number of moles of product. From the law of conservation of mass, moles of gas-phase carbon produced,  $Product_g$ , can be used to calculate, MeS moles, and the area of the contact,  $A_{actual}$ , will be the number of moles product divided by the constant moles per area of reactant, equation 2, this

assumes, of course, that direct contact is required between an area on the surface and the counter-surface to accelerate decomposition.

$$A_{actual} = Product_g / \left( \frac{MeS}{nm^2} \right) \quad (2)$$

This can be substituted into equation 1 to find the hardness of the contact,  $p_m$ .

The effect of sliding speed on the decomposition of adsorbed methyl thiolate species and influence on the friction coefficient was measured over the range of sliding speed from 0.1 to 10

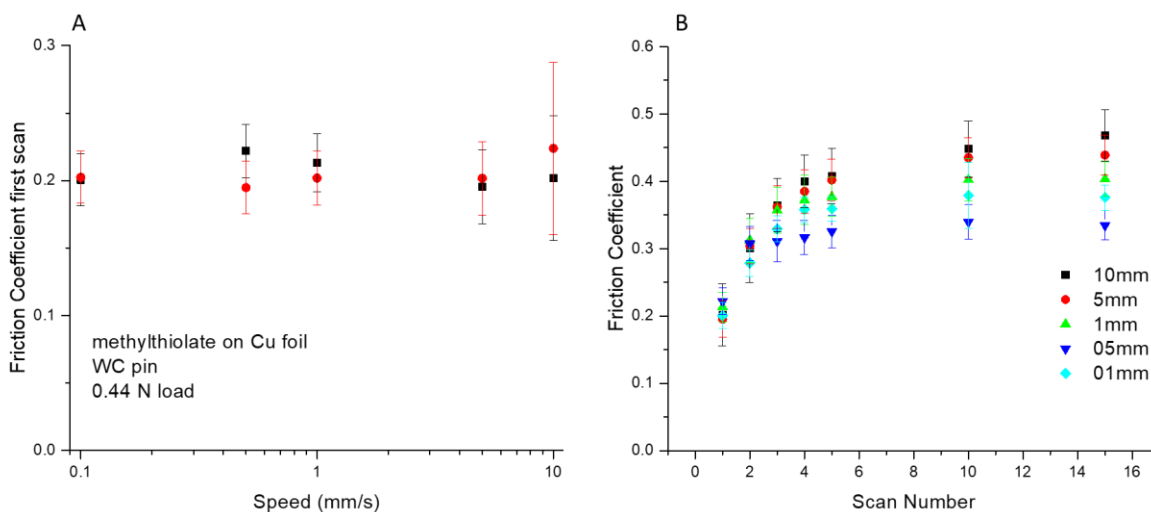


**Figure 8-4 (A) Friction coefficient of the first pass over a methyl thiolate covered surface has a constant value of  $0.2 \pm 0.02$  with speed. (B) change in friction with rubbing for all normal loads tested.**

mm/s. The coefficient of friction for the first pass over the thiolate-covered surface was constant as a function of sliding speed at  $0.2 \pm 0.02$ , as shown in Figure 4 A, indicating that the interaction between the surface and pin was unchanged with respect to speed. Since the normal force was not changed during the experiment, this means that the lateral force of sliding on the thiolate-covered surface was constant with speed. The difference between the friction coefficient on during load and velocity experiments that can be seen is due to the slightly different wear in procedure used in the two experiments, which has a large effect on the friction coefficient, but does not seem to affect

the rate of methane evolution, or the function of load and velocity on coefficient of friction. These experiments were repeated upwards of 5 times each, with the same trends present in every trial.

The bare copper produced after 15 scans shows an increase in friction coefficient with increasing speed, giving rise to an evolution of the friction coefficient dependent on rubbing speed, as shown in Figure 4 B. This indicates that there is some change in the plastic response of the either the bare copper surface, or the surface-to-bulk transport of the sulfur on the surface after decomposition of the methyl thiolate.

The rate constant for methyl thiolate decomposition was also constant as a function of sliding velocity, as shown in Figure 5, indicating that the shear force applied to the methyl thiolate was constant and above the plastic limit for the methyl thiolate-covered copper surface, as with load, or there is some catalytic enhancement of the rate that depends on contact, but not force, as discussed in the next section.

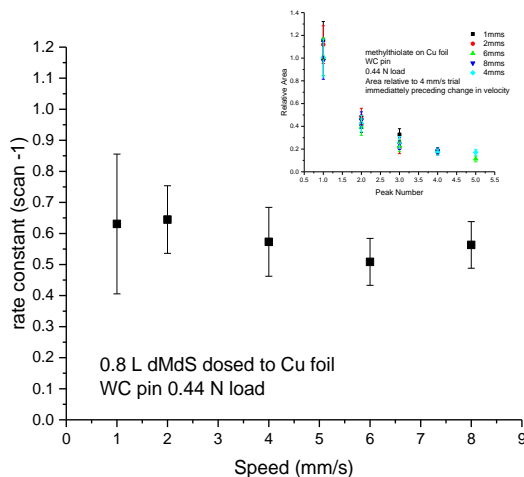


**Figure 8-5** Rate constant for methyl thiolate decomposition as a function of rubbing speed,  $0.59 \pm 0.05$ . Inset shows the peak area vs scan number for all scans.

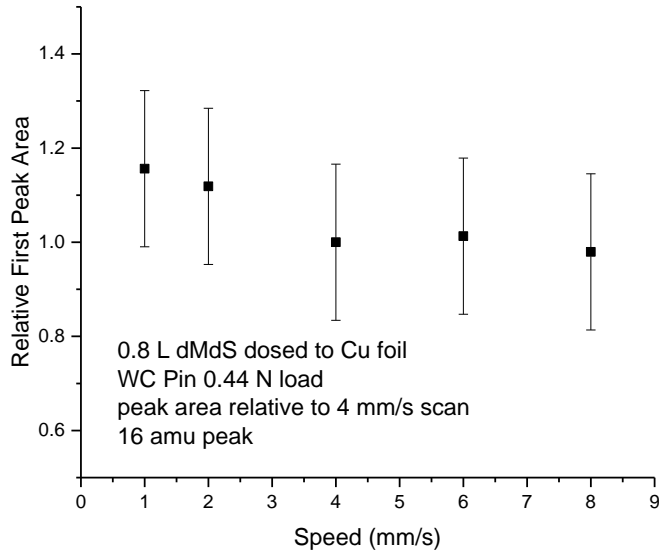


**Figure 8-6 Peak area of the 16 amu peak of first scan when sliding on a methyl thiolate covered copper foil for each velocity compared to a 4 mm/s scan done immediately after.**

In figure 6, methane peak area during first pass of the tribometer pin sliding over the methyl thiolate covered surface vs pin speed in mm/s, shows that the area of the methane peak during the first pass was relatively constant as a function of speed. This shows that the number of decomposition reactions per

pass was also relatively independent of the contact time between pin and methyl thiolate-covered surface.

## 8.5 Discussion

The exponential decay of the gas-phase products released during rubbing suggests a time dependence that is consistent with a first-order reaction rate for methyl thiolate decomposition. Interestingly, the velocity data shown in Figures 4, 5 and 6 show no contact-time dependence for the production of methane, the friction coefficient, or reaction rate, but shows dependence on number of passes (Figure 4B) and an alternative model to the Bell theory<sup>9</sup> is proposed for methyl thiolate decomposition in the following section.

The load data in Figure 1 suggests that the surface undergoes plastic deformation while rubbing, which will create a change in the surface structure. The increase in thiolate reaction rate

during sliding could be caused by an increase in the coverage of reactive, low-coordination sites during rubbing or an increase in the number of contacts with a catalytic counter-surface, also cause by plastic deformation. It has been shown that some copper single-crystal faces decompose methyl thiolate below room temperature<sup>10-12</sup> and sites similar to these structures could induce by sliding, or configurations of methyl thiolate and the counter face. If a mixture of surface structures induced by sliding is postulated, the rate of methyl thiolate decomposition will depend on the nature of these reaction sites, and the total rate constant for methyl thiolate decomposition will be the sum of contributions from these sites multiplied by that site's relative abundance, as shown in equation 3.

$$k = A_a \theta_a e^{-E_{aa}/kT} + A_b \theta_b e^{-E_{ab}/kT} + A_c \theta_c e^{-E_{ac}/kT} + \dots + A_n \theta_n e^{-E_{an}/kT} \quad (3)$$

where  $\theta_n$  is the relative coverage of sites of type,  $n$ , with a decomposition activation energy,  $E_{an}$  a pre-exponential factor,  $A_n$ . The total number of methyl thiolate sites,  $\theta_{total}$ , is equal to  $\theta_a + \theta_b + \theta_c + \dots + \theta_n$  and is normalized to unity. The rate constant,  $k$ , depends on both instantaneous and time-dependent processes, as in equation 4. It is assumed that some extremely reactive sites are formed, for example, types b and c, such that their activation to decomposing methyl thiol species at room temperature is very low i.e.,  $E_{bc}$  and  $E_{ac} \ll kT \approx 0$  such that  $e^{-E_{ab}/kT}$  and  $e^{-E_{ac}/kT} \sim 1$ . Equation 3 then becomes:

$$k = A_a \theta_a e^{-E_{aa}/kT} + A_b \theta_b + A_c \theta_c + \dots + A_n \theta_n e^{-E_{an}/kT} \quad (4)$$

The rapid decomposition of methyl thiolate on sites of those designated b and c will dominate the overall rate.  $A_n$  is the pre-exponential factor for the decomposition of methyl thiolate at all sites,  $n$ , with no thermal barrier at room temperature and is nearly constant for surface

processes,  $\vartheta_n$  is the sum of the coverage of all sites such that  $e^{-E_{an}/kT} \sim 1$ , such as sites b and c. This simplifies equation 4 to equation 5.

$$k = A_n \theta_n \quad (5)$$

The probability of finding any particular type of state on the surface during rubbing is predicted to follow the model that Eyring and Kraus developed to describe the plastic deformation of a solid.<sup>13</sup> If the formation and destruction of these reactive sites occurring on the surface is rapid compared to the movement of the pin across the surface, then the relative coverage for each site will reach some stable equilibrium value, and there will be no measurable time dependence in the rate of reactive site creation. Such “time-independent” plastic deformation in metals is well known<sup>14–17</sup> as the result of the equilibrium processes as described by the work of Eyring.<sup>18</sup> If the number of reactive sites during rubbing remains constant, then the rate of production of methane from methyl thiolate per pass,  $d[Me_g]/dp$  will be equal to the coverage of surface states with no barrier to decomposition of methyl thiolate,  $\vartheta_n$ . In the case of catalytic interaction between the methyl thiolate covered surface and the copper counter face (suggested by the DFT in Chapter 7) the explanation is even simpler, and the reactive sites are merely the product of the proximity of asperities to methyl thiolate in the interface. In either case, the rate of gas-phase methane produced per pass is a function of the coverage of methyl thiolate at reactive sites with the pre-exponential factor as shown in equation 6.

$$\frac{d[Me_g]}{dp} = -A_n [MeS_{ads}] \theta_n \quad (6)$$

Using equation 6 to solve for the methane yield per pass gives equation 7, which shows that the methane signal will decrease exponentially as a function of the number of passes,  $p$ , and the abundance of reactive sites.

$$\ln(Me_g) = -A_n \theta_n p \quad (7)$$

The exponential decay of the methane signal from methyl thiolate decomposition with load found in this dissertation agrees with this model. However, changing surface structure with loss of sulfur from the surface and work hardening could lead to more complicated variation on some surfaces.

## ***8.6 Proof of concept experiments***

Significantly more work is needed to develop a theory to model the coverage of each reactive site on material properties and sliding conditions and test it, and is not within the scope of this dissertation. However, the work of Rigney<sup>19,20</sup> suggests that nature of the surface sites is dependent on sub-surface flow processes, in which the atoms of the softer interface (in this work, copper) can be modeled as Kelvin-Helmholtz instabilities. Atoms in the sub-surface region eventually migrate to the interface, creating mixing of surface and sub-surface materials, as found in this work. This demonstrates that the nature of the surface sites is evolving with sliding, but models for this process need to be developed to correlate with the rate of decomposition. Work on the rate of surface and subsurface deformation is currently being done by Agribay<sup>21,22</sup> and Dienwiebel et. al,<sup>23,24</sup> and the rate of plastic deformation generated per pass could eventually be compared to the rate of evolution of methane caused by the decomposition of methyl thiolate on copper with sliding.

The following section is not, as stated in the introduction, meant to be a unifying theory that brings these ideas together. It is meant to serve as a proof-of-concept to show that further research in this area is a worth pursuing by indicating that the material properties of the substrate

can influence the rate of decomposition of methyl thiolate, and cannot be accounted for using a change in surface-structure that persists after contact.

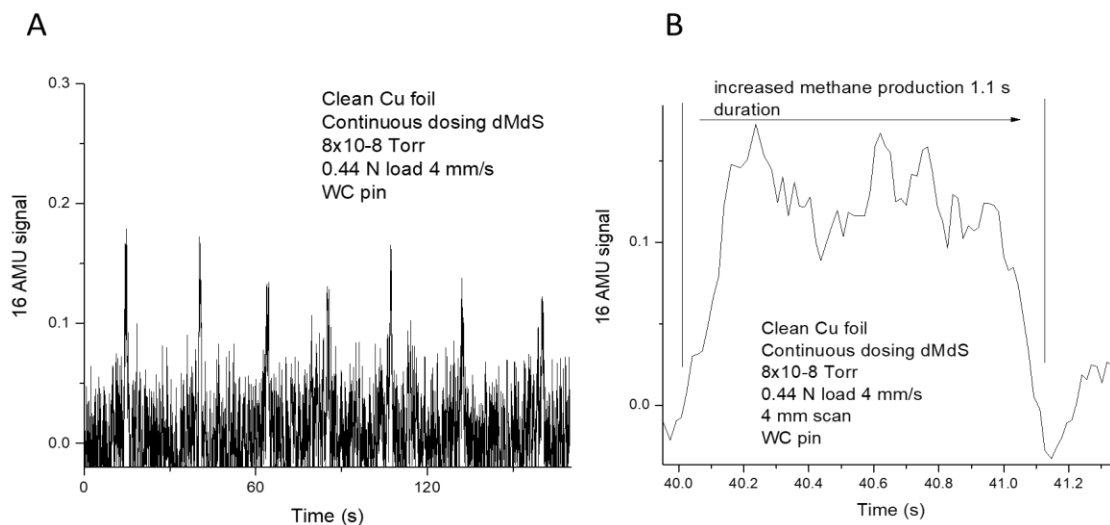


**Figure 8-7 Continuous dosing of dimethyl disulfide while rubbing. Methane production is only present during rubbing. (B) Width of the peak indicates that production of methane from the surface is dependent on contact with the pin.**

First, the time dependence of reactive surface structures within the sliding interface were investigated. It has been shown that the structural changes of the copper do not increase the coverage of residual reactive surface sites for 1-alkene decomposition<sup>25</sup> left after contact is ceased, and therefore an increase in reactive sites along the wear scar after the counter surface is removed for methyl thiolate is unlikely. To verify that this is the case, the dimethyl disulfide was constantly dosed to a wear scar and rubbed while collecting the 16 amu desorption signal and the results are shown in figure 7 A. The 16 amu signal while rubbing is clearly seen, even though the coverage of methyl thiolate was low due to the small time-interval for dosing between scans. An expanded view of one of the peaks is shown in 7 B, showing that the duration of methane production from the surface is 1.1s, roughly the length of the time it takes to scan the surface and then remove the pin. This indicates that reaction is not occurring on a more reactive surface in the rubbed region,

but rather the act of rubbing the surface is inducing methyl thiolate decomposition a methane formation.

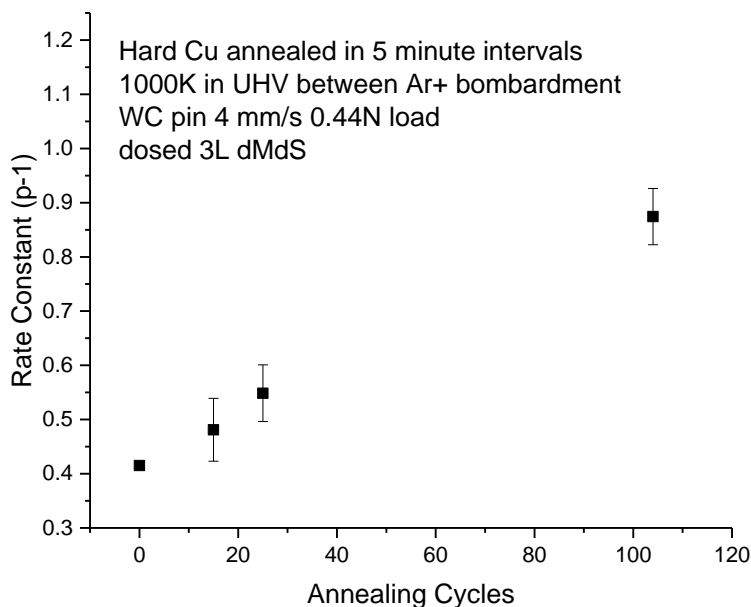


**Figure 8-8 Rate constant for the release of the methane per pass from a methyl thiolate covered copper surface vs the number of cycles of annealing and bombardment performed at 1000K.**

in UHV for different times. Annealing at 1000 K has a substantial effect on the grain size and therefore hardness, which is expected to decrease in copper with increasing annealing time and temperature. Softer samples are expected to undergo more deformation under load, and since it is hypothesized that the rate of the reaction depends on the rate of deformation of the sample, a softer sample should be more reactive. In this experiment the sample was annealed at 1000 K for five minutes, then cooled to 525 K and cleaned by argon bombardment to remove any sulfur that had been brought to the surface, and then heated again. Many cycles of annealing and bombardment were performed, and the methyl thiolate decomposition rate was measured as a function of number of cycles, shown in Figure 8. As the sample is annealed more times, the rate of the decomposition

Next, to confirm that the rate constant for methyl thiolate decomposition on the surface during sliding depends on the material properties of the copper substrate, the sample was softened by annealing

more than doubles, indicating a likely dependence of the decomposition kinetics of methyl thiolate on copper with mechanical properties.

The increase in reactivity with change in mechanical properties gives an opportunity to study the deformation of the surface during sliding with the copper structure. This could be due to a softer interface allowing more points of contact per unit area, (see equation 1) and increasing catalysis sites in the interface, or it could be an increase in the reactive sites on the surface created by the sliding interfaces. In this case, decomposition of methyl thiolate species can be used as a probe of the surface and near-surface structure during sliding and can be correlated with hardness from nano-indenter tests to measure the change in proportion of reactive states during rubbing as a function of grain size and sub-surface sulfur content within the wear scar. This information will allow more accurate models for predicting the wear of metals and tribo-film formation to be developed. Nudged-elastic-band calculations such as those presented in Chapter can be used to investigate the reactivity of various surface sites, and the relative coverage and activation energetics could be used in Monte-Carlo simulations to calculate the overall reaction rate to compare with experiment.

## ***8.7 Conclusion***

The rate of decomposition of methyl thiolate species on copper foil as a function of the number of passes appears to be controlled by the mechanical properties of the substrate. Plastic deformation of the copper is consistent with the lack of load or velocity dependence of the reaction kinetics, and the rate per pass of methyl thiolate decomposition does not depend on the length of time that force has been applied, but it does depend on the hardness of the copper sample,

indicating that the rate is likely controlled by a time-independent plastic deformation processes. These processes are present only during sliding because the continual roughening and smoothing of the surface during sliding is not present in the unrubbed system. This mechano-chemical reaction could likely be used as a probe to quantify these ephemeral, highly localized reaction structures at sliding interfaces that control the mechanism of wear and tribo-film formation.

## 8.8 References

1. Müser, M. H. *et al.* Meeting the Contact-Mechanics Challenge. *Tribol. Lett.* **65**, 118 (2017).
2. Furlong, O. J., Miller, B. P., Kotvis, P. & Tysoe, W. T. Low-Temperature, Shear-Induced Tribofilm Formation from Dimethyl Disulfide on Copper. *ACS Appl. Mater. Interfaces* **3**, 795–800 (2011).
3. Furlong, O., Miller, B. & Tysoe, W. T. Shear-induced boundary film formation from dialkyl sulfides on copper. *Wear* **274–275**, 183–187 (2012).
4. Miller, B. P., Kotvis, P. V., Furlong, O. J. & Tysoe, W. T. Relating Molecular Structure to Tribological Chemistry: Borate Esters on Copper. *Tribol. Lett.* **49**, 21–29 (2012).
5. Archard, J. F. Elastic Deformation and the Laws of Friction. *Proc. R. Soc. A Math. Phys. Eng. Sci.* **243**, 190–205 (1957).
6. Greiner, C., Felts, J. R., Dai, Z., King, W. P. & Carpick, R. W. Temperature Dependence of Nanoscale Friction Investigated with Thermal AFM Probes. *MRS Proc.* **1226**, 1226-NaN-2 (2009).
7. Jacobs, T. B., Gotsmann, B., Lantz, M. & Carpick, R. On the Application of Transition State Theory to Atomic-Scale Wear. *Tribol. Lett.* **39**, 257–271 (2010).
8. Liang, J. & Fernandez, J. M. Mechanochemistry: One Bond at a Time. *ACS Nano* **3**, 1628–1645 (2009).
9. Bell, G. I. Models for the specific adhesion of cells to cells. *Science (80-. )*. **200**, 618–627 (1978).

10. Zhai, R. S. *et al.* Chemisorption and reaction characteristics of methyl radicals on Cu(110). *Langmuir* **20**, 3623–3631 (2004).
11. Driver, S.M., Woodruff, D. P. Methanethiolate structural phases on Cu(100) and Cu(410). *Surf. Sci.* **488**, 207–218 (2001).
12. Lee, J. & Yates, J. T. Methanethiol Chemisorption on Cu(110): Chemical and Geometrical Issues Related to Self-Assembly. *J. Phys. Chem. B* **107**, 10540–10545 (2003).
13. Krausz, A. S. & Eyring, H. Chemical kinetics of plastic deformation. *J. Appl. Phys.* **42**, 2382–???? (1971).
14. Rice, J. R. Inelastic constitutive relations for solids: An internal variables theory and its application to metal plasticity. *J. Mech. Phys. Solids* **19**, 433–455 (1971).
15. Chaboche, J. L. Time-independent constitutive theories for cyclic plasticity. *Int. J. Plast.* **2**, 149–188 (1986).
16. Petryk, H. in (ed. Nguyen, Q. S.) 95–152 (Springer Vienna, 1993). doi:10.1007/978-3-7091-2712-4\_3
17. Ohno, N. & Wang, J.-D. Kinematic hardening rules with critical state of dynamic recovery, part I: formulation and basic features for ratchetting behavior. *Int. J. Plast.* **9**, 375–390 (1993).
18. Eyring, H. Viscosity, Plasticity, and Diffusion as Examples of Absolute Reaction Rates. *J. Chem. Phys.* **4**, 283–291 (1936).
19. Kim, H., Kim, W., Falk, M. & Rigney, D. MD Simulations of Microstructure Evolution

- during High-Velocity Sliding between Crystalline Materials. *Tribol. Lett.* **28**, 299–306 (2007).
20. Rigney, D. A. Transfer, mixing and associated chemical and mechanical processes during the sliding of ductile materials. *Wear* **245**, 1–9 (2000).
  21. Sawyer, W. G., Argibay, N., Burris, D. L. & Krick, B. A. Mechanistic Studies in Friction and Wear of Bulk Materials. *Annu. Rev. Mater. Res.* **44**, 395–427 (2014).
  22. Argibay, N., Chandross, M., Cheng, S. & Michael, J. R. Linking microstructural evolution and macro-scale friction behavior in metals. *J. Mater. Sci.* **52**, 2780–2799 (2017).
  23. Dienwiebel, M. & Pöhlmann, K. Nanoscale Evolution of Sliding Metal Surfaces During Running-in. *Tribol. Lett.* **27**, 255–260 (2007).
  24. Stoyanov, P. *et al.* Experimental and Numerical Atomistic Investigation of the Third Body Formation Process in Dry Tungsten/Tungsten-Carbide Tribo Couples. *Tribol. Lett.* **50**, 67–80 (2013).
  25. Miller, B. P., Furlong, O. J. & Tysoe, W. T. Tribological properties of 1-alkenes on copper foils: Effect of low-coordination surface sites. *Tribol. Lett.* **51**, 357–363 (2013).

# Chapter 9

## Conclusion

This experiments in this dissertation have provided several methods for investigating the acceleration of decomposition of methyl thiolate on a copper foil by normal and shear force.

The gas-phase products from the sliding-induced or “tribochemical” reaction of methyl thiolate on a copper foil decomposing to form gas-phase hydrocarbons and surface-sulfur were measured by mass spectrometry in ultrahigh vacuum (UHV) and found to follow first-order kinetics as a function of pass number. The extended-Bell model was applied to the analysis of the energy profile of a climbing nudged elastic band calculation (cNEB) of the reaction pathway to find the minimum force needed to produce the rate of the decomposition seen in the experiment. The change in the rate constant for the decomposition of methyl thiolate under shear was compared to the distribution of shear forces applied per thiolate molecule as predicted by the molecular dynamics (MD) simulations and matched the experimental rate.

The tribochemical reaction of a methyl or ethyl thiolate molecule on a copper foil consists of several elementary steps. First, the carbon-sulfur bond breaks, releasing a gas-phase alkyl group and leaving sulfur adsorbed on the surface. Next, the sulfur is transported to the sub-surface region, leaving a clean copper surface. It was found that the friction coefficient can be treated as the sum of the contributions from each component and the friction coefficient of each component

(methyl thiolate, sulfur, and copper) was multiplied by its relative abundance in the interface and fitted to the curve of the friction coefficient evolution with pass, showing good agreement.

This concept is applied to continuous dosing experiments to find the effect of the sub-surface sulfur on the friction coefficient. The amount of sub-surface sulfur after a given number of passes can be predicted from the rate of the surface-to-bulk transport and the friction coefficient of the sub-surface sulfur was found to be  $0.12 \pm 0.02$ , about double the friction coefficient of surface sulfur, 0.07.

Density functional theory was used to find the effect of normal load on the decomposition of methyl thiolate on a Cu (100) surface. The result was compared to the extended-Bell model and found to be a good fit. To find the effect of shear, the methyl thiolate was moved step-wise across the surface in the high-symmetry directions. It was found that the sulfur-copper bonds break before the sulfur-carbon bond with shear force, and it is likely that the sulfur-carbon bonds become stronger with copper-sulfur bond breaking due to a decrease in  $\pi^*$  back bonding.

The decomposition of methyl thiolate on a copper foil was tested for load and velocity dependence. No dependence on load and velocity for the rate of decay was found, furthermore, no dependence on contact time for the amount of sliding-induced, gas-phase, methane production was observed. A hypothesis was presented to explain the exponential decay of methane signal as a function of pass, rather than time. Changes in the surface structure caused by plastic deformation account for the evolution of the gas-phase products, though follow-up experiments were not within the scope of this work.

# CURRICULUM VITAE

## Education

Doctorate | 09/2009-2017

Major: Physical Chemistry

Minor: Organic Chemistry

Dissertation Title: INVESTIGATION OF TRIBOCHEMICAL REACTIONS USING THE MODEL SYSTEM OF METHYLTHIOLATE ON COPPER FOIL IN ULTRAHIGH VACUUM AND AB-INITIO CALCULATIONS

Bachelors of Science

09/1997-05/2003

University of Wisconsin-Oshkosh

Major: Chemistry

Undergraduate Project: Synthesis of the natural product, Radermachol, from a benzofuran starting material

## Publications

Adams, Heather et al. 2016. "In Situ Measurements of Boundary Film Formation Pathways and Kinetics: Dimethyl and Diethyl Disulfide on Copper." *TRIBOLOGY LETTERS* 62(1).

Adams, Heather L et al. 2015. "Shear-Induced Mechanochemistry: Pushing Molecules Around." *The Journal of Physical Chemistry C* 119: 7115–23.  
<http://pubs.acs.org/doi/abs/10.1021/jp5121146>.

Thuening, Theodore et al. 2016. "Kinetics of Low-Temperature CO Oxidation on Au(111)." *SURFACE SCIENCE* 648(S1): 236–41.

Furlong, Octavio et al. 2014. "Shear and Thermal Effects in Boundary Film Formation during Sliding." *RSC Advances* 4(46): 24059. <http://xlink.rsc.org/?DOI=c4ra03519d> (October 13, 2014).

Adams, H.L., et al. (2017). Modeling Mechanochemical Reaction Mechanisms. *ACS applied materials & interfaces*, 9 31, 26531-26538.

## **Awards**

Louise Arndt Fellowship 04/2013

International Tribology Forum travel scholarship 01/2014

## **Presentations**

### **62<sup>nd</sup> Annual International American Vacuum Science Symposium**

**10/2015** Oral presentation: Title: Monitoring the Gas-Phase Products of a Shear-Induced Reactions in Ultra-high Vacuum

### **Prairie Chapter American Vacuum Science Meeting**

**09/2015** Poster presentation: Investigating the Tribo-Decomposition of Methyl thiolate on Copper in Ultra-High Vacuum

### **University of Wisconsin-Milwaukee Chemistry and Biochemistry Awards Day**

**05/2015** Poster Presentation: Tribological properties of a gas-phase lubricated Copper system

### **International Tribology Forum**

**01/2014** Poster Presentation: Kinetics of tribochemical decomposition of methyl thiolate on copper foil

## **Teaching Experience**

- Physical Chemistry Laboratory
- General Chemistry, second semester
- General Chemistry, first semester
- Nursing Chemistry, second semester

- Developed course content and taught a section on plasmon resonance for a graduate course on nanoparticles